Surface nanobubbles and nanodroplets

Detlef Lohse[*]

Physics of Fluids Group, Department of Science and Technology, J. M. Burgers Center for Fluid Dynamics, and Mesa+ Institute, University of Twente, 7500 AE Enschede, The Netherlands, and Max Planck Institute for Dynamics and Self-Organization, 37077 Goettingen, Germany

Xuehua Zhang (张雪花)[†]

School of Civil, Environmental and Chemical Engineering, RMIT University, Melbourne, VIC 3001, Australia and Physics of Fluids Group, Department of Science and Technology, J. M. Burgers Center for Fluid Dynamics, and Mesa+ Institute, University of Twente, 7500 AE Enschede, The Netherlands

(published 31 August 2015)

Surface nanobubbles are nanoscopic gaseous domains on immersed substrates which can survive for days. They were first speculated to exist about 20 years ago, based on stepwise features in force curves between two hydrophobic surfaces, eventually leading to the first atomic force microscopy (AFM) image in 2000. While in the early years it was suspected that they may be an artifact caused by AFM, meanwhile their existence has been confirmed with various other methods, including through direct optical observation. Their existence seems to be paradoxical, as a simple classical estimate suggests that they should dissolve in microseconds, due to the large Laplace pressure inside these nanoscopic spherical-cap-shaped objects. Moreover, their contact angle (on the gas side) is much smaller than one would expect from macroscopic counterparts. This review will not only give an overview on surface nanobubbles, but also on surface nanodroplets, which are nanoscopic droplets (e.g., of oil) on (hydrophobic) substrates immersed in water, as they show similar properties and can easily be confused with surface nanobubbles and as they are produced in a similar way, namely, by a solvent exchange process, leading to local oversaturation of the water with gas or oil, respectively, and thus to nucleation. The review starts with how surface nanobubbles and nanodroplets can be made, how they can be observed (both individually and collectively), and what their properties are. Molecular dynamic simulations and theories to account for the long lifetime of the surface nanobubbles are then reported on. The crucial element contributing to the long lifetime of surface nanobubbles and nanodroplets is pinning of the three-phase contact line at chemical or geometric surface heterogeneities. The dynamical evolution of the surface nanobubbles then follows from the diffusion equation, Laplace's equation, and Henry's law. In particular, one obtains *stable* surface nanobubbles when the gas influx from the gas-oversaturated water and the outflux due to Laplace pressure balance. This is only possible for small enough surface bubbles. It is therefore the gas or oil oversaturation ζ that determines the contact angle of the surface nanobubble or nanodroplet and not the Young equation. The review also covers the potential technological relevance of surface nanobubbles and nanodroplets, namely, in flotation, in (photo)catalysis and electrolysis, in nanomaterial engineering, for transport in and out of nanofluidic devices, and for plasmonic bubbles, vapor nanobubbles, and energy conversion. Also given is a discussion on surface nanobubbles and nanodroplets in a nutshell, including theoretical predictions resulting from it and future directions. Studying the nucleation, growth, and dissolution dynamics of surface nanobubbles and nanodroplets will shed new light on the problems of contact line pinning and contact angle hysteresis on the submicron scale.

DOI: 10.1103/RevModPhys.87.981 PACS numbers: 47.55.np, 47.55.db, 66.10.C−

CONTENTS

[*]d.lohse@utwente.nl
[†]xuehua.zhang@rmit.edu.au

I. INTRODUCTION AND ORGANIZATION OF THE REVIEW

When a solid is fully immersed in liquid one expects that the liquid is in direct contact with the surface of the solid. However, this is often not the case. Rather, nanoscopic spherical-cap-shaped gaseous domains are present at the interface. These are called *surface nanobubbles*. Figure 1(a) shows a collection of surface nanobubbles on highly oriented pyrolytic graphite (HOPG), and Fig. 2(a) shows an individual nanobubble on a hydrophobized gold surface. With one to tens of nanometers in maximum height H (according to which they are called surface nanobubbles) and hundreds of nanometers to several microns in lateral diameter L, the volume V of a nanobubble [calculated from Eq. (3), see Fig. 2(b)] is on the order of attoliters. Assuming roughly ambient pressure (which is an underestimation due to the Laplace pressure, but gives an idea on the order of magnitude) and an ideal gas law, this corresponds to only $N \sim 10^3$ gas molecules. This number can be compared to the number of gas molecules which in principle could adsorb within the footprint area $\pi L^2/4$: These are about 500, assuming the adsorption cross section of 16 nm^2 for nitrogen resulting from the Brunauer-Emmett-Teller theory (Brunauer, Emmet, and Teller, 1938), i.e., the sublimation of only 1–2 layers of condensated gas molecules could fill the nanobubbles.

Surface nanobubbles were first speculated to exist about 20 years ago by Parker, Claesson, and Attard (1994) and later

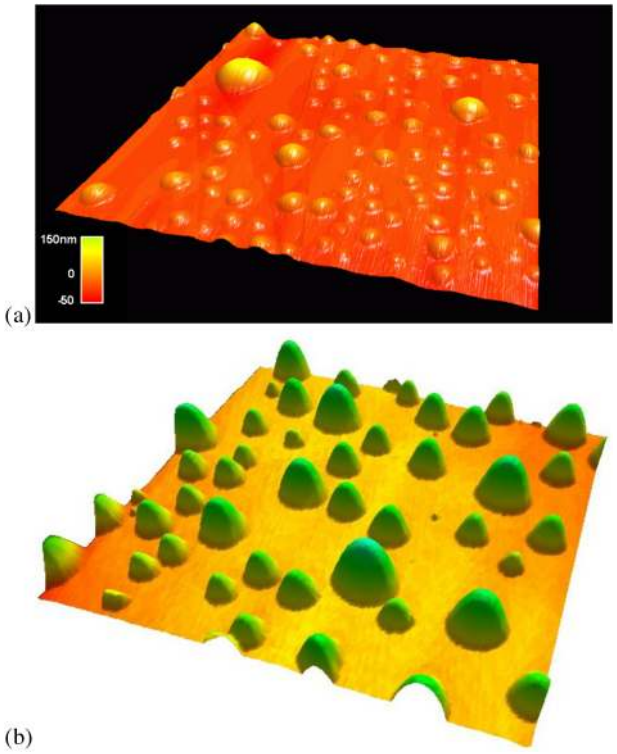

FIG. 1 (color online). (a) AFM image of nanobubbles produced by the solvent exchange method on HOPG. The imaged area is 4×4 μm^2. (b) AFM image of nanodroplets produced by the solvent exchange method on hydrophobized silicon. The imaged area is 30×30 μm^2, and the color code is from 0 to 800 nm.

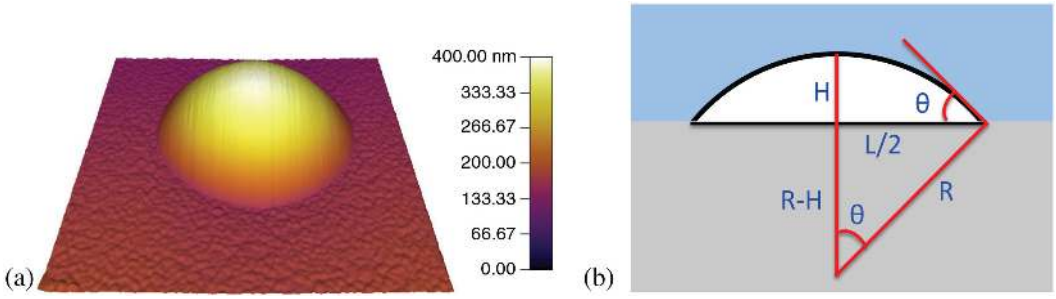

FIG. 2 (color online). (a) AFM image of a single large surface nanobubble on a hydrophobized gold surface. The mapped area is $3 \times 3\ \mu m^2$, and the color code is from 0 (dark) to 400 nm (bright). (b) Sketch of a surface nanobubble or nanodroplet and definition of the parameters describing their geometry, namely, the nanobubble's footprint lateral extension L (or its footprint radius $L/2$), its height H, its radius of curvature $R = (L^2 + 4H^2)/8H$ assuming a spherical cap shape, and its contact angle θ on the gas side. It holds $\tan\theta = (H/L)/[1/4 - (H/L)^2]$.

by Carambassis *et al.* (1998) and Yakubov, Butt, and Vinogradova (2000), based on stepwise features in atomic force curves between two hydrophobic surfaces (as shown in Fig. 3), eventually leading to the first atomic force microscopy (AFM) image by Lou *et al.* (2000) and Ishida *et al.* (2000); see Figs. 4(a) and 4(b). Another early AFM image (taken in the tapping mode) originates from Tyrrell and Attard (2001) and is shown in Fig. 4(c). While in the early years it was suspected that surface nanobubbles may be an artifact caused by AFM, meanwhile their existence was confirmed with various other methods such as attenuated total reflectance infrared spectroscopy (Zhang, Khan, and Ducker, 2007; Zhang, Quinn, and Ducker, 2008), quartz crystal microbalance (Seo, Yoo, and Jeon, 2007; Zhang, 2008), surface plasmon resonance (Martinez and Stroeve, 2007; Zhang, Khan, and Ducker, 2007; Zhang, Quinn, and Ducker, 2008), and neutron reflectometry (Steitz *et al.*, 2003). In contrast to AFM, these methods have the disadvantage of not allowing for any spatial resolution, but the advantage of being faster or detecting the chemical identity. At the scale of a single bubble, compelling evidence also comes from shock freezing (rapid cryofixation) of surfaces and subsequent scanning electron microscopy (SEM) imaging (Switkes and Ruberti, 2004), scanning

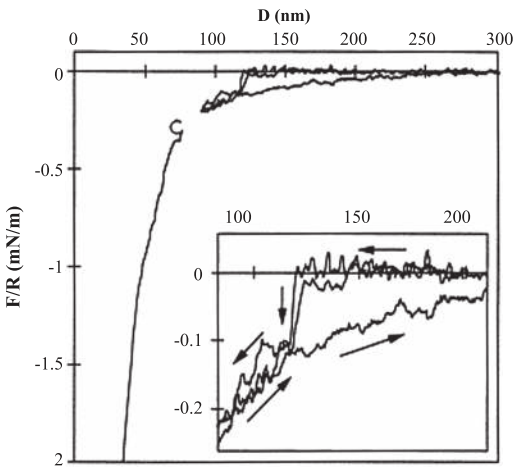

FIG. 3. Steplike features in the force vs distance curve from the measurements between two hydrophobic surfaces. The inset shows an enlargement for small distances, clearly revealing the hysteric behavior. From Parker, Claesson, and Attard, 1994.

transmission soft x-ray microscopy (L. Zhang *et al.*, 2013), and single photon counting combined with fluorescence lifetime imaging microscopy (Hain *et al.*, 2015). Surface nanobubbles were also directly optically observed with interference-enhanced reflection microscopy (Karpitschka *et al.*, 2012) and with total-internal-reflection-fluorescence microscopy (TIRF) (Chan and Ohl, 2012), although evidently these optical methods are inferior to AFM with respect to spatial resolution.

The existence of surface nanobubbles was claimed to be paradoxical (Ball, 2003), as a simple estimate based on the high Laplace pressure inside the nanoscopic object suggested that they should dissolve within the diffusive time scale $\sim R^2\rho_g/Dc_s$ (Epstein and Plesset, 1950; Ljunggren and Eriksson, 1997; Simonsen, Hansen, and Klösgen, 2004), corresponding to 100 μs, given a radius of curvature $R \approx 10^{-7}$ m, the diffusion constant $D \approx 2 \times 10^{-9}$ m^2/s of gas in water, and the ratio between the gas density ρ_g and the gas solubility c_s, which is $\rho_g/c_s \approx 0.014$ for nitrogen. Indeed, the Epstein-Plesset theory shows that small enough bubbles (for which the Laplace pressure dominates the ambient pressure and the gas overpressure) are pressed out by the diverging Laplace pressure against any oversaturation within microseconds. Yet, surface nanobubbles are known to survive for days.

Next to their long lifetime, the second main peculiarity of surface nanobubbles is their small and size-dependent contact angle θ [on the gas side, extracted from AFM images, see, e.g., Lou *et al.* (2000, 2002), Tyrrell and Attard (2001), Holmberg *et al.* (2003), Yang *et al.* (2003), Simonsen, Hansen, and Klösgen (2004), and Zhang *et al.* (2004) for early work], as compared to what one would expect from the macroscopic contact angles and from Young's equation

$$\cos\theta = \frac{\sigma_{SL} - \sigma_{SG}}{\sigma_{LG}}, \tag{1}$$

which connects the surface tensions (also called interfacial tensions, in particular, when one deals with liquid droplets in another liquid) σ_{SL}, σ_{SG}, and σ_{LG} for the solid-liquid, solid-gas, and liquid-gas interfaces.

In this review we mainly use the contact angle θ and the footprint diameter L to characterize surface nanobubbles and nanodroplets. Assuming a spherical-cap shape, the bubble height

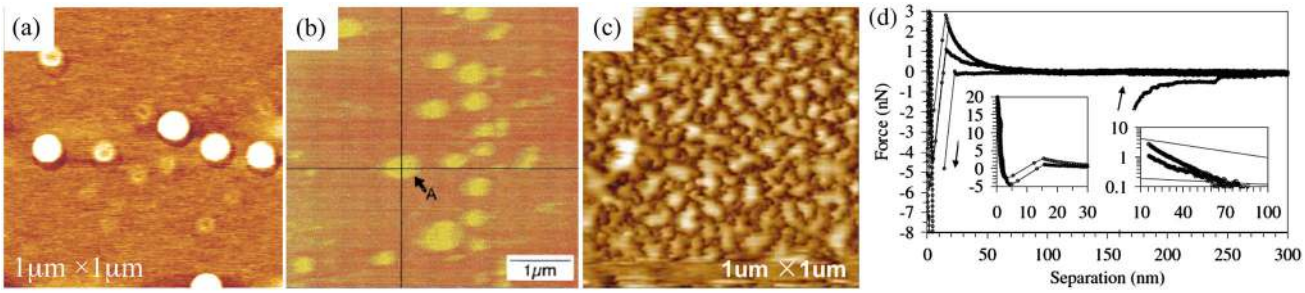

FIG. 4 (color online). Three of the first AFM images of surface nanobubbles and the force-separation curves on nanobubbles. (a) Nanobubbles created by the solvent exchange process on a water and mica interface. The image area is $1 \times 1\ \mu m^2$. From Lou *et al.*, 2000. (b) Nanobubbles created by immersion on octadecyltrimethylchlorosilane (OTS) silicon. The arrow (A) points to a nanobubble. The scale bar is 1 μm. From Ishida *et al.*, 2000. (c) Nanobubbles created by immersion on silanized silicon. From Tyrrell and Attard, 2002. (d) Force vs separation curve, for both approaching (arrows to left) and departing AFM tip (arrow to right), clearly showing the jumps for the case of the tip detaching from the bubble. The conditions are the same as in (c). The insets show zoom ins for the curves. From Tyrrell and Attard, 2001.

$$H = \frac{1-\cos\theta}{2\sin\theta} L, \tag{2}$$

its volume

$$V = \frac{\pi}{24} H(3L^2 + 4H^2), \tag{3}$$

and its radius of curvature

$$R = L/(2\sin\theta) \tag{4}$$

follow; see Fig. 2(b).

Surface nanobubbles form either spontaneously at immersion of a (hydrophobic) surface in water or by creating some gas oversaturation in direct vicinity to a (hydrophobic) surface (e.g., through some solvent exchange process or photo- or electrochemically), on which they then nucleate.

In many respects similar to gaseous surface nanobubbles are surface nanodroplets, which are shown in Fig. 1(b). They can be produced in a completely analogous way to surface nanobubbles, namely, either by immersion or by solvent exchange processes (Zhang, Ren *et al.*, 2012) which create a local oversaturation of one liquid in another. Since surface nanodroplets show features similar to those of gaseous surface nanobubbles, they can easily be confused with them (Berkelaar *et al.*, 2014). They should also dissolve in clean water (just as a nanobubble should dissolve in degassed water), but when the solubility of the liquid of the droplet in water is low as is often the case, they may survive for a long time and their existence is considered to be less spectacular. As both the creation process and the properties of surface nanobubbles and surface nanodroplets are so similar, we consider it as illuminating to also cover the latter in this review, although the focus is on the former.

Back to the gaseous surface nanobubbles: Various theories have been suggested to account for their remarkable stability: Contamination on the surface, hindering gas exchange and reducing the surface tension (Ducker, 2009), a dynamic equilibrium theory (Brenner and Lohse, 2008), postulating that the gas outflux is balanced by some gas influx, and pinning (Weijs and Lohse, 2013; Zhang, Chan *et al.*, 2013; Liu *et al.*, 2014; Liu and Zhang, 2014; Lohse and Zhang, 2015), to name only the most popular ones. These theories have meanwhile been made quantitative, leading to predicted phase diagrams.

At present, we are in a phase in which incidental information on surface nanobubbles is more and more replaced by systematic and quantitative experimental, theoretical, and numerical studies. Also the technological relevance of surface nanobubbles shows up on the horizon. While in the early years progress came mainly from colloidal science, in recent years it became clear that the fluid dynamics of and around the surface nanobubbles is crucial for their understanding. In fact, nanobubbles bring together neighboring disciplines, namely, physics of fluids, colloidal science, surface chemistry, soft matter, optical and imaging sciences, nanotechnology, and perhaps an even broader group of scientists who might be key to understanding this puzzle.

The community now is in need of standardized procedures to reproducibly produce surface nanobubbles, without any trouble from contamination. We are now also in need of new visualization and characterization methods, complementary to AFM with all its limitations with respect to time resolution and difficulties in applying this technique in water, with less ambiguity in the interpretation of the data. With such techniques controversial observations should be reproduced or falsified. We are in need of numerical models which couple nanoscale molecular dynamics (MD) simulations with fluid mechanics approaches. And finally, at present a theoretical framework based on the diffusion equation, the Laplace pressure, Henry's equation, and pinning is developing, which can account for many puzzling findings.

The review is organized as follows: It starts with a description of how nanobubbles and nanodroplets are generated (Sec. II) and what methods have been used to detect them (Sec. III). We also alert the interested reader of possible artifacts in nanobubble studies. In Sec. IV we describe the properties of surface nanobubbles, starting with the evidence for their gaseous nature, and surface nanodroplets. We cover studies both on the morphology of individual nanobubbles and nanodroplets and on their collective organization. In Sec. V we review MD simulations which analyzed the emergence, properties, and dissolution of surface nanobubbles. Section VI introduces the various theories which had been suggested to

account for the surface nanobubbles and, in particular, for their stability and their low contact angle (on the gas side). We discuss pros and cons of the various theories and focus on predictions resulting from them, and report on whether these predictions had been confirmed or not, or how to confirm or falsify them. In Sec. VII we come to the potential technological relevance of surface nanobubbles and nanodroplets and, in particular, also touch upon the relative new field of vapor nanobubbles and plasmonic bubbles. These potentially have great applications for solar energy and catalysis. We end the review with a summary of our view on surface nanobubbles and nanodroplets in a nutshell and with a list of the main open issues for future research (Sec. VIII). In particular, we suggest key future experiments and, based on our present view, make predictions on their outcome.

Prior review articles on surface nanobubbles exist (Hampton and Nguyen, 2010; Craig, 2011; Seddon and Lohse, 2011; Zhang and Lohse, 2014), giving shorter overviews. Some of them are meanwhile already a few years old and the field has developed fast. In the present review we, in particular, work out the illuminating analogy between surface nanobubbles and surface nanodroplets, viewing them as basically the same phenomenon. For a separate review on ultrasmall nanodroplets at solid-liquid or solid-gas interfaces see Mendez-Vilas, Jodar-Reyes, and Gonzalez-Martin (2009); for a review on evaporating droplets see Cazabat and Guéna (2010).

We note that next to surface nanobubbles laterally much larger, but at the same time much thinner gaseous objects may exist at the solid-water interface. Depending on their detailed features, these objects are called either *micropancakes* (Zhang *et al.*, 2007; Zhang, Maeda, and Hu, 2008; Zhang *et al.*, 2009; Seddon *et al.*, 2010) or highly ordered gas condensates (Lu, Yang, and Hwang, 2012, 2014; Yang, Lu, and Hwang, 2013; Lu *et al.*, 2014) or interfacial gas enrichments (Peng, Birkett, and Nguyen, 2013; Peng, Hampton, and Nguyen, 2013) and typically have an extension of up to microns, but are only one or two molecular layers thick. We think that these objects are chemically bound gas molecules and thus of different nature as the gaseous surface nanobubbles. They were reviewed by Seddon and Lohse (2011) and will not be covered in this review article.

II. HOW TO MAKE SURFACE NANOBUBBLES AND SURFACE NANODROPLETS

A. Importance of a reproducible protocol

The prerequisite for understanding the formation and the fundamental properties of surface nanobubbles and for exploring their potential applications is a reproducible protocol to produce them. Direct immersion of a hydrophobic substrate into water, a temperature increase or a pressure reduction at the surface of an already immersed substrate, photochemical or electrochemical reactions, or a solvent exchange can all possibly induce the formation of nanobubbles. Unfortunately, an easy-to-follow method with perfect reproducibility is still lacking, but much needed, in order to facilitate the experimental study of surface nanobubbles. Even with the ethanol-water exchange, the most often used protocol to induce nanobubbles, several parameters, such as the flow rates of the liquids during the exchange process, the boundary conditions during the mixing, and the concentration gradient of the solvents, are expected to be highly relevant, but have not yet been optimized or controlled.

It is also critical that the characterization techniques can distinguish nanobubbles from other nanoscale objects. Ideally, a simple standard procedure can be applied after the bubble formation to prove that they are indeed gaseous. Moreover, it would be even better to be able to switch back and forth between the state without nanobubbles and the one with nanobubbles.

This section discusses the various ways of formation or surface nanobubbles and nanodroplets. The various observation techniques applied to them, with their respective pros and cons, are discussed in Sec. III.

B. Spontaneous formation at immersion

The easiest way to form bubbles at a surface may be to directly bring a dry surface into contact with water, either by immersing the surface into water or by depositing a drop onto the surface. Indeed, when a drop is falling on a surface, the air pressure between surface and droplet builds up, leading to a dimple formation in the droplet and thus a macroscopic bubble is entrained at contact; see, e.g., Bouwhuis *et al.* (2012). Also surface roughness may contribute to trap gas in between the surface and the liquid. So surface nanobubbles may either directly form when the liquid comes into contact with the surface or result from some local gas supersaturation originating from the immersion process.

How does one determine whether surface nanobubbles have formed upon immersion? With the arrival of tapping mode atomic force microscopy around 2000, direct visualization of a hydrophobic surface in water became possible; see Fig. 4. Two of the three pioneering papers show the AFM images of surface nanobubbles on a hydrophobic substrate after immersion, namely, those by Ishida *et al.* (2000) and Tyrrell and Attard (2001); the third pioneering paper, namely, by Lou *et al.* (2000), shows the nanobubbles after solvent exchange. The two former papers will now be discussed and the third one in Sec. II.C.

Ishida *et al.* (2000) observed some features with a spherical dome shape on a smooth silanized silicon substrate. As seen from Fig. 4(a), the nanobubbles are sparsely distributed over the imaged area. The contact angle of the nanobubble is smaller than the macroscopic contact angle, which was attributed to the deformation by AFM imaging and the heterogeneity of the surface. The force curves collected by the AFM tip on top of the spherical domes show the stepwise features already mentioned, a unique feature indicating submicron bubbles already reviewed in the earlier work on force measurements by Christenson and Claesson (2001).

Tyrrell and Attard (2001, 2002) observed nanobubbles after immersion of the hydrophobized glass in direct contact with water; see Fig. 4(c). AFM imaging revealed the irregular networks with a mean height of 20–30 nm on the substrate. The evidence that the networks were nanobubbles came from the mechanical and morphological tests. The force measurements between a silica sphere and the surface showed the long-range attraction in the approach curve and strong adhesion in the withdraw curve, see Fig. 4(d), which is similar to the original hysteric force curve by Parker, Claesson, and Attard (1994) (Fig. 3). Furthermore, the

nanobubbles were not observed in contact mode imaging, possibly caused by the disruption enforced by the AFM tip. Reimaging the substrate by tapping mode after the contact mode test showed that nanobubbles reemerged. Moreover, nanobubbles were obtained by first flushing the substrate with ethanol and then with water (Attard, Moody, and Tyrrell, 2002; Tyrrell and Attard, 2002). The nanobubbles disappeared in a solvaphilic fluid (ethanol) and then reappeared in water (Tyrrell and Attard, 2002), a process essentially the same as the solvent exchange process which is discussed in detail in Sec. II.C.

Later, some doubt was cast on the work by Tyrrell and Attard (2001, 2002). Evans, Craig, and Senden (2004) argued that all the physical and morphological features provided in the work could be equally well ascribed to a liquid phase (i.e., droplets) rather than to gas bubbles and that the images of the "nanobubbles" in fact originated from the partially polymerized silane coating. From previous studies, e.g., Biggs and Grieser (1994), Mcgovern, Kallury, and Thompson (1994), Wang and Lieberman (2003), Wang *et al.* (2005), and Howarter and Youngblood (2006), it is known that, when prepared carefully, the silane self-assembles into a homogenous monolayer on silicon. However, often polymerization and aggregation of silane occur during the reactions in the presence of excessive moisture and give rise to soft features on the substrate (Wang *et al.*, 2005). It is indeed essential to distinguish imperfect coating from nanobubbles, and we come back to this point in Sec. II.F.

In any case, several pioneering concepts conceived in the early work by Tyrrell and Attard (2001, 2002) turned out to be highly relevant for the later understanding of the nanobubble properties, namely, the ideas that nanoubbles may not be hemispherical but irregularly shaped due to the strong pinning on the boundary, that their lifetime might be related to their peculiar morphology, and that gas supersaturation of the water may play an important role in their stability.

We now discuss papers in which the nanobubbles were produced on various substrates by immersion. Yang *et al.* (2003) examined four substrates with different hydrophobicity and roughness by tapping mode AFM in 0.01M CO_2 aqueous solution. The formation of CO_2 nanobubbles was related to roughness and hydrophobicity of these substrates. They formed on methylated silicon, but not on dehydroxylated silicon or clean hydrophilic silicon. Moreover, nanobubbles on rough, methylated surfaces were larger and less densely distributed than those on a smooth surface with similar hydrophobicity (Yang *et al.*, 2003). These results demonstrated that both the substrate hydrophobicity and its roughness are important for nanobubble formation at immersion.

Agrawal *et al.* (2005) confirmed the importance of the substrate hydrophobicity for the nanobubble formation, showing that nanobubbles formed on flat hydrophobic polystyrene, but not on flat hydrophilic polymethylmethacrylate (PMMA). They also revealed the importance of the spatial extension of the hydrophobic areas for the nanobubble formation. By using substrates with well-defined polymer patterns, they found that nanobubbles never formed on hydrophilic PMMA domains regardless of the domain size, but do form on hydrophobic polystyrene nanopatterns as long as the polystyrene domains were large enough (over several hundreds of nanometers). No nanobubbles were observed when the widths of the hydrophobic patterns were as small as 40 nm.

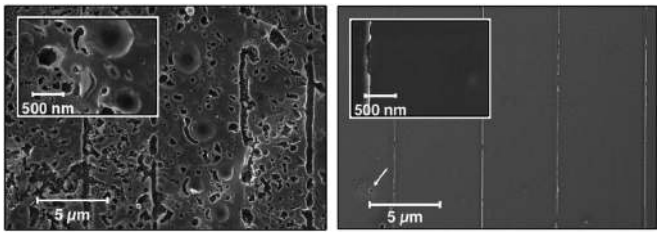

FIG. 5. SEM images of the replicas of an interface of a hydrophobic substrate air-saturated water (left) and in (right) degassed water, obtained by cryofixation. The insets show enlargements. For the case of air-saturated water (left), the voids, which originated from the nanobubbles at the interface, are clearly visible. For the degassed case (right), the interface is smooth as no nanobubbles have formed. From Switkes and Ruberti, 2004.

The absence of nanobubbles on hydrophilic surfaces was also found by Switkes and Ruberti (2004). The SEM images of rapid cryofixation and freeze fracture revealed that the surface of a *hydrophilic* substrate was smooth in gas-saturated water, i.e., no nanobubbles had formed. In contrast, the interface between gas-saturated water and *hydrophobized* Si was covered with a network of 100 nm scale features, as shown in Fig. 5. Those voids were absent for the degassed water, confirming that those features were gaseous nanobubbles, nucleating spontaneously from the dissolved gas at the hydrophobic surface.

How hydrophobic does a surface have to be to trigger surface nanobubble nucleation at immersion? Song, Walczyk, and Schönherr (2011) claimed to have observed nanobubbles on thiol-coated gold with different hydrophobicity, ranging from a contact angle of 107° (hydrophilic) down to 15° (hydrophobic). This variation of contact angle was achieved by changing the ratio of different types of thiols assembled on the surface, following a method by Bain and Whitesides (1988). Holmberg *et al.* (2003) found them on unmodified gold surfaces (known to be much less hydrophobic) immersed in water, namely, identifying them through a jump in during the approach of an AFM tip to the surface. However, care must be taken: Although a perfectly clean bare gold surface is hydrophilic, localized airborne adsorbed impurities can immediately render the surface much more hydrophobic.

Further immersion experiments were conducted with various other substrates (Simonsen, Hansen, and Klösgen, 2004; Borkent *et al.*, 2007; S. Yang *et al.*, 2007; Seddon *et al.*, 2011; Seddon, Zandvliet, and Lohse, 2011; van Limbeek and Seddon, 2011; Berkelaar *et al.*, 2012). Some of the substrates were not well characterized, but the overall picture that emerged is that the formation of surface nanobubbles is related to the concentration of the dissolved gas, temperature, hydrophobicity, and the physical and chemical structures of the substrates, i.e., to their heterogeneities.

However, we also mention that some researchers doubt that surface nanobubbles can indeed spontaneously form upon immersion of a hydrophobic substrate in water. Many precise measurements, for example, by ellipsometry (Mao *et al.*, 2004; Takata *et al.*, 2006), did not detect nanobubbles on hydrophobic surfaces in direct contact with water. AFM images of the substrate sometimes show nanobubbles and other times they do not. This discrepancy may be due to different coverages with

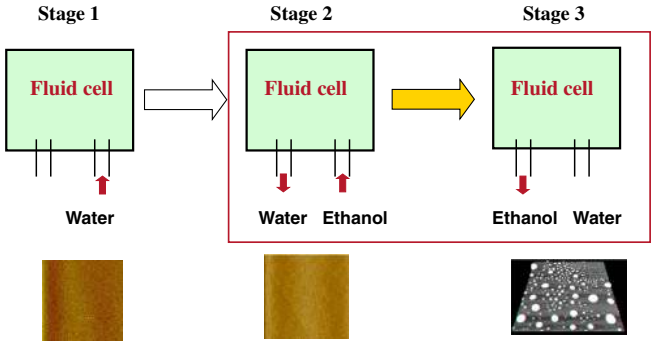

FIG. 6 (color online). Schematic drawing of the solvent exchange process. The substrate (often HOPG or silanized Si) is first exposed to water (stage 1) and characterized by AFM. In the second step, water is replaced by ethanol (stage 2) and the substrate is imaged again. In both cases no surface nanobubbles are seen. In the actual solvent exchange process, the ethanol is replaced by water (stage 3), leading to surface nanobubble nucleation on the substrate.

surfactants or due to the fact that the sparse distribution of nanobubbles on the surface precludes their detection. It is difficult to achieve high coverage with surface nanobubbles, given that the understanding of the formation mechanism is still not fully quantitatively understood. It seems plausible that the nanobubbles originate from the air entrainment when the hydrophobic substrate is brought into contact with water. However, it is crucial to establish reproducibility of this process and correlate the contact dynamics with the bubble formation. Along with the morphological features, the chemical identity should be provided by complementary measurements (e.g., spectroscopically) to prove that the found objects are indeed trapped gaseous nanobubbles.

Again, it is important to point out that in many cases (some) nanoscale objects found on a substrate in contact with water in fact are not nanobubbles, but either nanodroplets of a contaminating liquid, solid nanoscale contaminations, or surface defects. Such artifacts are discussed in detail in Sec. II.F.

C. Solvent exchange process

In the meanwhile the most-used protocol to induce surface nanobubbles is the solvent exchange process. It was first applied to produce nanobubbles on a mica surface by Lou *et al.* (2000). At that time, the then new development of tapping mode AFM made high-resolution imaging in a liquid environment possible. Mica is the most common supporting substrate for AFM imaging, as a clean and smooth surface can be conveniently obtained by cleavage. In an attempt to clean mica already assembled in an AFM fluid cell, Lou *et al.* (2000) happened to inject ethanol and then water into the cell, a sequence that many people would follow for crude surface cleaning. When the mica surface was imaged in tapping mode AFM again, instead of a cleaner surface Lou *et al.* (2000) saw some spherical objects on the surface and suspected that they were gas nanobubbles. Later it was shown that those features are closely related to the level of dissolved gas in ethanol and water (Zhang *et al.*, 2004).

The standard protocol of the solvent exchange process is shown in Fig. 6, where the substrate is first in contact with water which is then replaced by ethanol. No surface nanobubbles are observed by AFM in either case. In the actual solvent exchange process the ethanol is then slowly replaced by water. During this process long-living surface nanobubbles form. In the solvent exchange, both ethanol and water are saturated or even oversaturated with air or a specific gas. Qualitatively, the mechanism for the surface nanobubble formation is that because gases have a higher solubility in ethanol than in water, a transient gas oversaturation is locally created when the good solvent (ethanol) is replaced by a poor solvent (water). Thus there is excess gas close to the surface, leading to the nucleation of surface nanobubbles. A quantitative approach to theoretically describe the solvent exchange process is given in Sec. VI.G. The level of dissolved gases is crucial as evidenced by experiments with partially degassed liquids: When both ethanol and water are partially degassed, the number density of the surface nanobubbles is lower (Zhang *et al.*, 2004). A sketch of an experimental realization of a flow cell to perform the solvent exchange process is shown in Fig. 7.

Apart from ethanol, other organic solvents, such as methanol, propanols, tert-butanol, acetone, or acetic acid, can also be used in the solvent exchange (Zhang, Wu *et al.*, 2005; Hampton, Donose, and Nguyen, 2008). Those solvents all have a higher solubility for air than water and at the same time are miscible with water so that they can be completely rinsed off from the system by water.

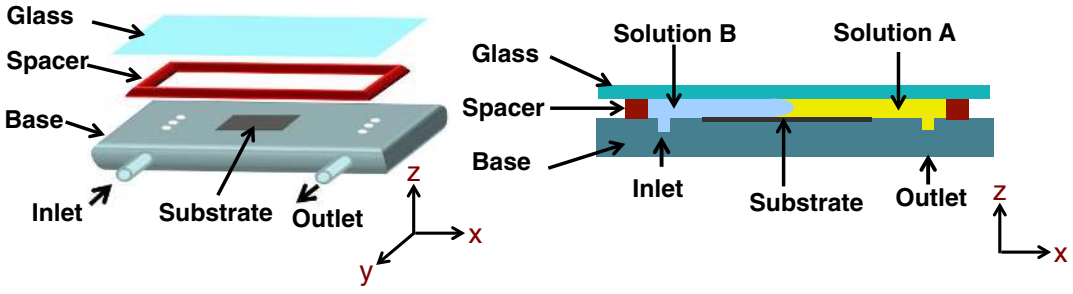

FIG. 7 (color online). Schematic drawings of a fluid cell for the solvent exchange process. It consists of a glass top window, spacer, and a base. The hydrophobic substrate is placed inside the cell, facing the transparent glass window. The distance between the substrate and the glass bottom side can be adjusted by the height of the spacer. During the solvent exchange process, solution A (typical ethanol, with high gas solubility) is pushed away by solution B (typical water, with low gas solubility) and is injected into the flow cell with a controlled flow rate. The flow direction is along the x axis. Note that both solutions are subject to the no-slip flow boundary conditions on the flow walls and thus also on the substrate. From Zhang, Lu *et al.*, 2015.

The solvent exchange process has meanwhile successfully been applied in many research groups to produce surface nanobubbles; see, e.g., Martinez and Stroeve (2007), S. Yang *et al.* (2007, 2008), Hampton, Donose, and Nguyen (2008), Palmer, Cookson, and Lamb (2011), Chan and Ohl (2012), Ishida, Kusaka, and Ushijima (2012), Karpitschka *et al.* (2012), and Belova *et al.* (2013). We discuss many of these papers later in this section and in Sec. IV on the properties of surface nanobubbles.

The protocol of the solvent exchange process also provides a procedure to obtain *liquid surface nanodroplets* at an interface between a solid and an immiscible liquid. Here the solvent exchange is akin to the solvent shifting technique, which had been applied to the preparation of homogeneous polymer nanoparticles, also known as *nanoprecipation*, or solvent diffusion, or the diafiltration method (Aubry *et al.*, 2009; Schubert, Delaney, Jr., and Schubert, 2011; Aschenbrenner *et al.*, 2013; Roger, Botet, and Cabane, 2013; Geissler *et al.*, 2014). Indeed, the formation of small droplets or particles by shifting the solvent quality is well known to a general audience as the so-called "Ouzo effect": When Greek "Ouzo" or French "Pastis" or Turkish "Raki" are diluted with water before consumption, the drink immediately becomes cloudy. The process is the spontaneous emulsification in a ternary system: ethanol, oil, and water. Oils that are much more soluble in alcohol than in water (e.g., anise) form small droplets upon the addition of water (Vitale and Katz, 2003). Figure 8 shows the stable Ouzo domain in a three-component system of hexadecane (oil), acetone (good solvent), and water (poor solvent) (Yan *et al.*, 2014). The system stays for a long time in the region between the spinodal curve (stability boundary) and binodal curve (thermodynamic equilibrium), provided that there is a large kinetic barrier (Vitale and Katz, 2003; Aubry *et al.*, 2009; Roger, Botet, and Cabane, 2013).

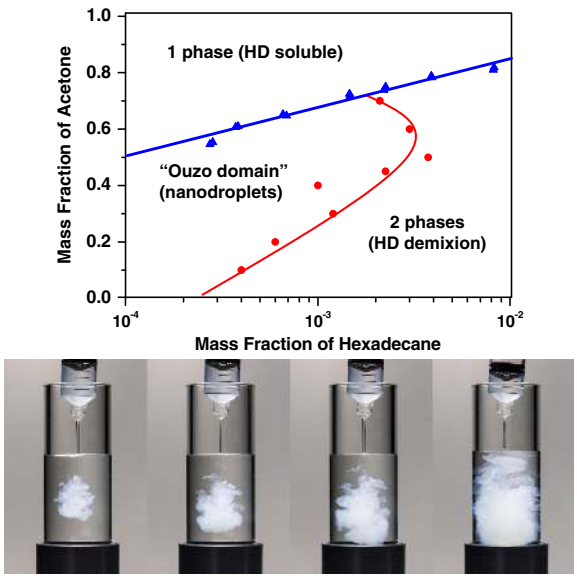

FIG. 8 (color online). (Upper) Phase diagram of a tertiary system of hexadecane (HD) in an acetone and water mixture, showing the binary curve and the Ouzo limit. Hexadecane is immiscible in water but miscible in acetone, while acetone and water are miscible. The Ouzo effect occurs when the system is brought rapidly from the one-phase region into the metastable region between the binodal and spinodal curves. From Yan *et al.*, 2014. (Lower) Solvent exchange: Four snapshots of clear water injected into Ouzo, showing the nucleation of oil droplets. From Sander Huisman and Roeland van der Veen (Twente).

In the actual solvent exchange for producing surface nanodroplets at a solid-liquid interface, there are three basic requirements (Zhang and Ducker, 2007): (i) A pair of miscible solvents that act as the first and the second solution (i.e., ethanol and water in the Ouzo case). (ii) The liquid of the droplet phase (i.e., oil in the Ouzo case) that has a lower solubility in the second solution than in the first solution. (iii) A substrate with appropriate wettability for the droplet phase on the substrate in contact with the second solution, i.e., in general a hydrophobic substrate.

The difference between the solvent shifting technique and the solvent exchange technique is that in the latter the droplets nucleate on the surface after the liquid phase is replaced by water and are thus in addition affected by the surface properties, while in the solvent shifting technique particles form in a mixture of solvent and nonsolvent. It is thus a pure bulk effect.

Both the solvent shifting technique and the solvent exchange technique are sensitive to temperature and mixing rate. Thus the exact way how the solvents and the water are added to each other matter. To control the mixing processes, Schubert, Delaney, and Schubert (2011) used an automated pipetting robot to optimize the conditions for nanoparticle fabrication by nanoprecipitation. Clearly, further specification of the fluid dynamical parameters of the solvent exchange process would be desirable to achieve better controllability and reproducibility in the formation of surface nanodroplets.

In the following we discuss a few examples of the formation of surface nanodroplets. The first example is nanodroplets of decane on silanized Si or highly oriented pyrolytic graphite (Zhang and Ducker, 2007). The first solution is a 30%–50% ethanol aqueous solution that is saturated with decane. The second solution is water or decane-saturated water. Decane droplets form after the exchange of the ethanol aqueous solution by water. The size of the decane droplets increases with increasing ethanol concentration, because then the solubility of oil increases in the first solution and thus higher oversaturation is achieved through the solvent exchange process.

In another example, Zhang, Wei, and Ducker (2010) produced toluene nanodroplets on a polystyrene substrate by the solvent exchange of toluene-saturated 40% ethanol solution and toluene-saturated water. In the last example Zhang, Ren *et al.* (2012) produced surface nanodroplets of *polymerizable* liquids by solvent exchange. In this case the nanodroplets can later be photopolymerized and converted to permanent polymeric nanolenses by following the procedure as shown in Fig. 9. These solid nanolenses can then easily be characterized by AFM imaging in air. The size and shape of the nanolenses follow their precursor liquid nanodroplets and can simply be adjusted through the wettability of the nanodroplets. For example, the addition of surfactants in the solutions can adjust the aspect ratio of the lenses (Yang *et al.*, 2014). Recently, the conversion process was applied to capture the time evolution of the contact angle of nanodroplets after different periods of dissolution (Zhang, Wang *et al.*, 2015), as an alternative to the approach of "freezing" the polymer microdroplets at a temperature lower than their transition point (Seemann *et al.*, 2005).

Compared to surface nanodroplets, the control of nanobubble formation (to which we now return) is even more

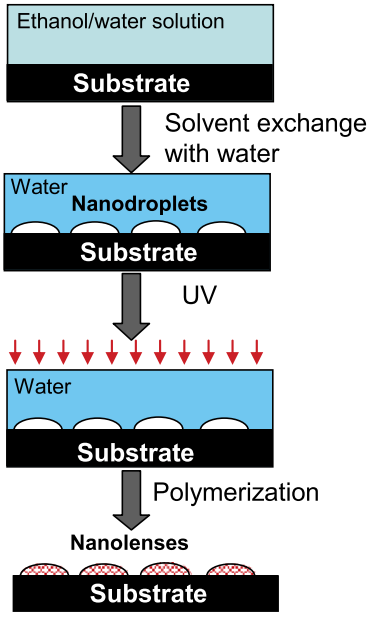

FIG. 9 (color online). Protocol to make and polymerize surface nanodroplets. From Zhang, Ren *et al.*, 2012.

complicated, because the saturation level of gas cannot be controlled as easily as that of oil. As discussed, even the solvent exchange process can hitherto not achieve perfect reproducibility in the formation of nanobubbles, as there are apparently relevant experimental parameters which have not yet been controlled, quantified, and optimized: These may be the flow rate, the shear at the substrate, the gas concentration gradient of the solvents, and other flow boundary conditions. Not surprisingly, it remains a daunting task to control the size and number density of nanobubbles. Attempts in this direction are a few qualitative studies on the effects of the temperature, the substrate properties, and the mixing patterns, which we now summarize.

1. Temperature control

Xu *et al.* (2014) showed that the substrate temperature is important for the reproducibility of nanobubble formation. The substrate of HOPG was kept at different temperatures while the liquid temperature before the solvent exchange was around 37 °C. The reproducibility of the bubble formation is significantly improved when the substrate temperature is 50 °C or above. The maximal bubble size also increased with increasing substrate temperature. The interpretation is that at enhanced temperatures the relative gas solubility decreases and that therefore more and larger surface nanobubbles form, but also the enhanced kinetics (i.e., faster gas diffusion) at elevated temperatures may help. Earlier, Zhang *et al.* (2004) showed that the number density of nanobubbles on a mica surface increased with the increase of the liquid temperature from 9 to 30 °C. In that study, the substrate temperature was not controlled, but expected to be similar to the temperature of ethanol.

2. Physical and chemical properties of the substrate

By the solvent exchange process, nanobubbles were produced on various substrates including HOPG, talc, molybdenum disulphide (MoS_2), octadecyltrimethylchlorosilane (OTS) or 1H,1H,2H,2H-perfluorodecyltrichlorosilane (PDFTES) coated Si, and decanethiol-coated gold. The wettability of this substrate is summarized in Table I. The physical and chemical properties and the structures of the solid surfaces even down to atomic scale affect the formation and morphology of the nanobubbles. The reproducibility of the bubble formation so far appears to be the best on cleaved atomically flat hydrophobic surfaces (talc or HOPG). Zhang and Maeda (2011) demonstrated the important role of the surface physical structure by comparing HOPG and amorphous carbon. Although chemically both materials consist of carbon atoms, nanobubbles can be produced only on the former.

In addition to surface nanobubbles, micron-sized bubbles can concurrently form in the solvent exchange process, provided the substrate is highly hydrophobic (Zhang, Maeda, and Craig, 2006). Those microbubbles form on geometric nucleation sites on the surface, such as microfabricated regular arrays of hydrophobic micropits (Zhang, Lhuissier *et al.*, 2013).

Just as with the immersion technique, with the solvent exchange process no nanobubbles could be produced on hydrophilic surfaces, such as glass or bare Si. The only exception is mica. This is really puzzling, given the low contact angle of water on mica (Lou *et al.*, 2000; Zhang *et al.*, 2004). It might be due to the crystalline structure of mica, dissociation of ions from the surface, or unavoidable airborne adsorbents on mica.

3. Mixing flow

The exact way of mixing during the exchange of ethanol by water is also important for the formation of nanboubbles. The

TABLE I. Advancing and receding contact angles (for consistency on the air site in contrast to the usual notation) of a macroscopic water droplet on various substrates and the nanobubble contact angle for nanobubbles formed by solvent exchange (*) or direct immersion. No obvious correlation between the microscopic and nanoscopic angles is seen. OTS stands for octadecyltrichlorosilane, TMCS for trimethylchlorosilane, and PFDS for perfluorodecyldimethylchlorosilane.

Substrate	Advancing contact angle (deg)	Receding contact angle (deg)	Nanobubble	θ_{NB}	Reference
Mica*	175	180	Yes	30–60	Lou *et al.* (2000), Zhang *et al.* (2010), and Wang *et al.* (2015)
HOPG*	85	115	Yes	5–20	Lou *et al.* (2000, 2002), Zhang, Maeda, and Craig (2006), and Wang *et al.* (2015)
OTS coated Si*	70	80	Yes	10–30	Zhang, Maeda, and Craig (2006)
TMCS coated Si	92	113	Yes	26	Yang *et al.* (2003)
PFDS coated Si	105		Yes	50	S. Yang *et al.* (2007)

flow rate influences the concentration gradient of ethanol and hence the transit saturation level of the gas, as the solubility of atmospheric gases decreases (nonlinearly) with the decrease of ethanol concentration in water (Pollack, 1991). In case that the exchange was performed stepwise, that is, ethanol was replaced subsequently by an ethanol aqueous solution of 80%, 60%, 40% etc., no nanobubbles formed on the surface (Ishida, Kusaka, and Ushijima, 2012). The mixing pattern is also related to the shear on the surface. However, no systematic study has hitherto been performed to quantify how the shear and the resulting Reynolds number influences the efficiency of nanobubble formation.

D. Temperature difference method

An extension of the solvent exchange is the temperature difference method (Zhang *et al.*, 2007; Guan *et al.*, 2012). By this method, nanobubbles are produced by the exchange of cold water (4 °C) by warm water (25–40 °C). The reason that this method works is that the gas solubility is higher in cold water than in warm water, and thus gas oversaturation is created during the cold-warm water exchange. For example, for N_2 in water it decreases from $c_s \approx 0.018$ kg/m^3 at 25 °C to $c_s \approx 0.010$ kg/m^3 at 60 °C; for a parametrization of the full functional dependences $c_s(T)$ for various gases see Lide (1995). The advantage of the temperature difference method is that no organic solvents are used in this procedure, which avoids some potential risk of contaminations from the organic solvent.

Another interesting extension of this method may be the use of a salt solution (Guo *et al.*, 2012; Liu *et al.*, 2013). Nanobubbles were observed on HOPG after the exchange of water by a salt solution. The mechanism may again be the gas oversaturation resulting from the exchange process, because water has a higher gas solubility than the salt solution. However, this does not explain the formation of surface nanobubble also observed for an exchange process in the other direction, i.e., after the exchange of salt solution by water (Guo *et al.*, 2012), as then the solubility of gas goes the other way around.

E. Photochemical and electrochemical nanobubble production

In electrochemical reactions, a large amount of gas molecules are produced at an electrode through electrolysis, leading to a high gas concentration in the system and thus to bubble nucleation in the bulk or on the electrode surface. We discuss technological applications in Sec. VII.D. Often the emerging surface bubbles are in fact unwanted, e.g., in electrochemical deposition, as the bubbles on the electrodes cause defects in electrodepositions (Tsai *et al.*, 2002). It is reasonable to assume that in electrolysis surface nanobubble generation precedes the emergence of the visible surface microbubbles.

The earliest direct experimental observation of surface nanobubbles produced by electrochemical reactions was achieved by L. Zhang *et al.* (2006) who combined an electrochemical reaction cell with *in situ* tapping mode AFM to produce and image electrochemically generated nanobubbles. In their experiments, HOPG served as both the substrate for imaging and the working electrode. Both auxiliary and quasireference electrodes were platinum wires. The electrolyte solution was a *degassed* 0.01*M* sulfuric acid solution. The study showed that formation and growth of surface nanobubbles on HOPG could be controlled by tuning either the applied voltage (−1.4 to −2 V) or the electrochemical reaction time under the same potential. More and larger bubbles formed after a longer reaction time for a given applied potential, or a higher potential for a given reaction time. Micron-sized bubbles detached from the surface and left a circular nanobubble-free zone.

In contrast, Yang *et al.* (2009) found that for low enough potential ($\sim 1-2$ V) electrolytically formed nanobubbles grew only for a limited time, even though the potential was continuously applied. The current stabilized on a finite value, which was considerably smaller than the original current, due to the partial blockage of the electrodes by the formed nanobubbles. They proposed that electrolytically generated nanobubbles must be in a dynamic equilibrium between the electrolytic gas influx and a diffusive gas outflux. At higher potentials of $\sim 4.5-5.0$ V, microbubbles developed and were visible by optical microscopy.

Why are the observations from these two groups different with respect to the nanobubble growth? There is clearly a difference in their experimental details. First, Yang *et al.* (2009) did not have a quasireference electrode in the production of hydrogen or oxygen nanobubbles. Missing a reference electrode could lead to an uncertainty of the applied potential on the working electrode. Therefore care should be taken in comparison of the minimum potential required for the nanobubble generation. Second, L. Zhang *et al.* (2006) removed the dissolved air before the electrochemical reaction, so any potential effect from dissolved air was eliminated, whereas Yang *et al.* (2009) did not predegas the liquid. Third, L. Zhang *et al.* (2006) performed electrochemical reactions intermittently between capturing the AFM images, whereas Yang *et al.* (2009) AFM imaged the nanobubbles simultaneously with the ongoing electrochemical reaction. In the latter case, the dynamical evolution of the nanobubbles may be affected by the AFM tip.

A disadvantage shared in the work from both groups is the much larger surface area of the working electrode (HOPG) as compared to the auxiliary electrode. Such arrangement can cause a highly nonuniform distribution of the electric field over the HOPG surface, adversely affecting the control of the gas saturation and thus the nanobubble nucleation. Moreover, multiple nanobubbles can form simultaneously on the surface, which further complicates the nanobubble growth dynamics due to cross talk among neighboring bubbles.

The above difficulties were overcome by Chen, Luo, and White (2015) and Luo and White (2013), who used a platinum nanoelectrode with a radius smaller than 50 nm. In the experiments by Luo and White (2013), a nanodisk electrode was fabricated by sharpening the top of a Pt wire sealed inside a glass capillary. The nanoscale dimension of the electrode provided a nucleation site for a single nanobubble and in addition the sensitivity in the voltametric response measured through the Pt wire. As the hydrogen nanobubble was generated by the reduction of protons, it partially occupied the surface area on the nanoelectrode and thus partially blocked further proton transport. Thus a sudden drop, faster than a few hundred milliseconds, in the current can be detected. The time scale of this sudden drop gives an estimate of the required time to nucleate a surface nanobubble. Such a voltametric response at different

concentrations of electrolyte can also be used to determine the critical hydrogen concentration in the solution for the initial nanobuble formation: The results of Luo and White (2013) showed that the formation of nanobubbles required an *oversaturated* gas concentration, but was independent of the electrolyte concentration or the rate of the applied potential. After generation, the nanobubble stayed in a dynamically stable state and lived indefinitely, as long as the threshold potential was applied to feed the system with electrons. In this dynamical equilibrium state the bubble dissolution is balanced by the hydrogen generation from the partly nanobubble covered nanoelectrode.

In continuation of this work, Chen *et al.* (2014) measured the voltametric response at different concentrations of acid solutions to show that the critical concentration of dissolved hydrogen required for the nanobubble nucleation is 310-fold larger than the hydrogen solubility at the pressure of 1 bar and room temperature. This is different than observed by Seddon *et al.* (2011) and Guan *et al.* (2012) who found that nanobubbles can form at undersaturated conditions. The effects of surfactants on the nanobubble nucleation on the nanoelectrode were consistent with the classical theory: The increase of surfactant concentration in the electrolyte solution resulted in a lower nucleation energy barrier and consequently a lower supersaturation concentration required for the nanobubble nucleation (Chen *et al.*, 2014).

Clearly, the controlled nanobubble formation on a single nanoelectrode or, more sophisticated, on an array of nanoelectrodes, is promising in understanding the nucleation and growth of a single nanobubble or several interacting nanobubbles under well-defined conditions. What presently is missing in these studies is the nanobubble size, which is critical for quantifying the dynamics. It is highly desirable to obtain it through AFM or other *in situ* techniques.

Huang *et al.* (2009) captured the evolving hydrogen nanobubbles by deposing gold on the bubble surface in a so-called electroless reaction, which is an autocatalytic reaction to deposit metal without requiring an external current. The bubbles acted as templates and reducing agent in the electroless deposition of gold on the inner wall of narrow channels. The hollow gold nanoparticles replicated the morphology of the hydrogen nanobubbles.

A striking twist to electrochemically generated nanobubbles is given by Svetovoy *et al.* (2011, 2014) and Svetovoy, Sanders, and Elwenspoek (2013). Rather than dc, they used ac with frequencies between 20 and 100 kHz and thus electrochemically generated nanobubbles with stoichometric mixtures of hydrogen and oxygen ("knallgas"). These nanobubbles densely covered the electrodes and when merging they could ignite. They also showed that the resulting violent implosions of the knallgas nanobubbles and microbubbles damaged the platinum electrodes.

Nanobubbles may also nucleate from produced gases in photochemical or catalytic reactions. For example, Shen *et al.* (2008) observed nanobubbles on surface-coated titanium dioxide through a photocatalytic reaction in a methanol and water solution. Another example is oxygen nanobubbles which are formed on a Pt surface by the catalytic decomposition of H_2O_2 to H_2 and O_2 (Paxton *et al.*, 2004).

F. Potential artifacts in nanobubble studies

Studies on surface nanobubbles have encountered various artifacts, partly due to the limitation of the main tool, AFM, that is unable to distinguish nanobubbles from other objects, and partly due to uncontrolled contamination. Many soft nanoscale features on a surface in AFM images can actually be due to some entities other than nanobubbles. Some typical ones are heterogeneity of the substrate, features on the substrate induced by water, and adsorbents from the liquid phase. We discuss these in this section.

Geometric heterogeneities on the substrate can emerge during the production process and when it comes into contact with water. For example, silicon can be hydrophobized with a self-assembled monolayer of silane. However, without enough caution, the silane molecules easily form aggregates and the silane oligomerization leads to nonuniformity on the surfaces in the form of islandlike patches and physically adsorbed aggregates (Biggs and Grieser, 1994; Mcgovern, Kallury, and Thompson, 1994; Wang and Lieberman, 2003; Yang *et al.*, 2003; Mao *et al.*, 2004; Wang *et al.*, 2005; Howarter and Youngblood, 2006). Similar problems occur for surfaces coated with fluoroalkylsilane that can also oligomerize in the presence of water. It is therefore crucial to avoid the aggregates or thoroughly remove them before use and to characterize the surface to ensure that they are free of unknown structures before the generation of nanobubbles.

Another pitfall is that even if the substrate is indeed flat in a dry condition, the morphology of the substrate can change upon contact with water. This is a particularly relevant case for polystyrene coated Si, a popular substrate for several groups (Steitz *et al.*, 2003; Simonsen, Hansen, and Klösgen, 2004; Bhushan, Wang, and Maali, 2008; Wang, Bhushan, and Zhao, 2009a, 2009b; Wang and Bhushan, 2010; Mazumder and Bhushan, 2011; Li *et al.*, 2014). It is important to note that a polymer thin film on a hydrophilic substrate is often subjected to instabilities in contact with water (Joanny and de Gennes, 1984; de Gennes, 1985). The polymer thin film may dewet from the surface and form polymeric nanoparticles. Another danger is that water can penetrate through the thin film by osmosis and form blisters between the polymer membrane and the substrate (Berkelaar *et al.*, 2015). Both nanoparticles and blisters can easily be mistaken as bubbles solely based on AFM measurements.

Contamination may also originate from adsorbents from liquids. A typical example is the use of disposable syringes for handling liquid. Berkelaar *et al.* (2014) found that nanobubbles prepared by using plastic syringes stayed on the surface even exposed to degassed water for more than 90 hours. Their control experiments showed that these nanobubbles were in fact due to the dissolved materials (e.g., lubricants) sitting on the needles of (medical) plastic syringes. They thus were nanodroplets. Apart from exposing surface nanobubbles respective surface nanodroplets to degassed water in order to distinguish between them, there are other ways to do so: Chan *et al.* (2015) studied the collision dynamics between these features with a three-phase contact line (TPCL). They showed that while a surface nanobubble rapidly shrinks when colliding with the TPCL, a polymeric droplet pins it.

Perhaps most importantly are the chemical heterogeneities on the surface which arise from the attachment of air-bound (often organic) contaminations and which are nearly unavoidable for all the measurements in ambient conditions. These patches of chemical heterogeneities can lead to contact line pinning which, as we argue in Sec. VI, are considered to be crucial for the properties and, in particular, the stability of surface nanobubbles. In this sense these chemical surface heterogeneities are not a bug of the system—they are a feature.

Luederitz and von Klitzing (2012, 2013) directly demonstrated the effect of hydrophobic patches on pinning and surface nanobubble formation. They exposed originally hydrophilic silicon wafers to an aqueous solutions of hexadecyl trimethyl ammonium bromide (CTAB) at concentrations between 0.05 up to 1 mM critical micelle concentration (CMC). From AFM studies they deduced the formation of surface nanobubbles on hydrophobic patches on the surface, whereas for increasing CTAB concentration the hydrophobic properties of the patches vanished.

III. HOW TO OBSERVE SURFACE NANOBUBBLES AND SURFACE NANODROPLETS

A wide range of techniques are available for investigating surface nanobubbles and nanodroplets. Some of them provide a high spatial resolution, such as AFM (the most popular technique for surface nanobubbles in the last ten years, although it is a slow technique, providing only long time averages) and SEM; others are sensitive to the chemical properties of the spatially averaged interfaces, such as attenuated total reflection infrared spectroscopy, neutron reflectivity, x-ray scattering, and surface plasmon resonance spectroscopy. The great challenge is how to achieve high spatial resolution and at the same time good temporal resolution and chemical identification. Up to now there are no techniques available for such a comprehensive characterization of nanobubbles and nanodroplets. Often two or three complementary techniques are required to obtain a more complete picture. In this section we discuss the strengths and limitations of each technique. We will not go into the technical details extensively, but focus on the aspects that are critical for the data interpretation.

A. Observations with atomic force microscopy

AFM is a member of the family of scanning probe microscopy (SPM), which is capable of characterization and manipulation of features on an atomic scale (Binnig, Quate, and Gerber, 1986). High-resolution images and force measurements can be obtained by AFM in air and in liquids. Several earlier review articles have explained in detail the principles and applications of AFM imaging (Garcia and Perez, 2002), force measurements (Cappella and Dietler, 1999; Butt, Cappella, and Kappl, 2005), AFM in vacuum (Giessibl, 2003), and theories of SPM (Hofer, Foster, and Shluger, 2003). Here we focus on the applications of AFM in a liquid environment at an atmospherical pressure and room temperature for investigating surface nanobubbles and nanodroplets.

The advantage of AFM is the incomparable 3D resolutions of surface nanobubbles and nanodroplets. In particular, the contact angle of nanobubbles [as depicted in Fig. 2(b)] can be extracted from the cross-sectional profile of a nanobubble in the AFM image. However, one of several disadvantages of AFM is the inevitable perturbation of the examined sample by the probe. Thus one concern of the early days of nanobubble research was that the nanobubbles were not present on the surface until the surface was actually perturbed by the AFM probe. Only after several other complementary measurements (as described later) also showed the presence of surface nanobubbles was it generally accepted that surface nanobubbles are not the consequence from the tip perturbation. This will be discussed further in Sec. III.B when we come to non-AFM techniques.

Several AFM modes are available for probing nanobubbles and nanodroplets, including contact mode, tapping mode, frequency modulation mode, force mapping, and peak force quantitative nanomechanics (QNM). Among different imaging modes, the contact mode is the least used mode as it is too destructive: A considerable lateral force in the contact mode is exerted to the bubbles and the tip can thus sweep the bubbles away during the imaging (Holmberg *et al.*, 2003). We first discuss the tapping mode, then force mapping, and finally the more recent peak force QNM.

1. Tapping mode imaging

The tapping mode AFM in liquid is the most frequently used mode to obtain the morphology of nanobubbles and nanodroplets. In this mode, a soft cantilever is oscillating at a drive frequency close to the resonance frequency of the cantilever (e.g., 6–12 kHz). The amplitude of the oscillation is maintained at a constant value, i.e., 95%–98% of the free amplitude at the interaction with the sample. The motion of the oscillating cantilever reduces the lateral forces exerted to the sample, which is crucial for success in imaging soft materials. But it is highly nontrivial to obtain a one-to-one correspondence between the imaging parameters and the mechanical force applied to the nanobubble or nanodroplet from an oscillating tip.

The set point, which is the ratio of the oscillation amplitude to the free amplitude of the cantilever, is one of the most important parameters to optimize the imaging quality. What is the effect of the set point on the nanobubble deformation? Zhang, Maeda, and Craig (2006) observed that the size of nanobubbles in water did not change much for set points from 0.93 to 0.74. Yang *et al.* (2008) varied the set point from 0.89 to 0.78 and also observed that the nanobubbles appeared to be only slightly smaller with the decrease of the set point. But for smaller set points below 0.67 the deformation was larger and at 0.44 the nanobubbles became flat.

2. Force mapping

In force mapping, an array of force curves shows the cantilever deflection at different distances from the substrate. The initial contact between the tip and the bubble or droplet surface usually leads to a sudden change in the approach curve. Such a jump in is shown in Fig. 4(d). The distance between the jump in and the hard substrate reflects the height

of the nanobubble or nanodroplet at the specific point where the force curve was collected, from which the morphology can be reconstructed. Different from the contact mode, the force measurement does not apply a substantial lateral shear along the surface, as the tip is far off the surface between each touch on the surface. For the same reason, obtaining a force map with good spatial resolution is however time consuming.

In early work, the force mapping was applied to investigate the profile of a single oil nanodroplet on a polystyrene surface in air (Connell *et al.*, 2002). Zhang, Maeda, and Craig (2006) adapted this technique to obtain cross-sectional profiles of nanobubbles on OTS Si in water. The contact angles, deduced from the profile, were consistent with tapping mode measurements.

A convenient function available on some recent models of AFM is the possibility to obtain the force curve measurement on a location determined on the topographic image. In this way, one can compare the height measured from the image and the jump-in distance in the force curve. The heights of the nanobubbles measured from such topographic images turned out to be similar to those obtained by the measurements of the jump-in distances in the force curves (Zhang *et al.*, 2010).

3. Peak force QNM

The main concern of tapping mode AFM is that it is difficult to quantify how much force is applied from the oscillating tip to the bubble surface, or how much the bubble is deformed during the imaging. This concern is partly addressed through measurements with peak force QNM, an increasing popular imaging and mechanical mapping mode.

Peak force QNM allows for the simultaneous collection of high-resolution morphological images and quantitative mechanical mapping. In this mode, a periodically modulated probe interacts with the surface at a modulation frequency of ~2 kHz. This frequency is significantly lower than the resonance frequency of the cantilever, an important difference from the drive frequency in tapping mode. Also different from the amplitude in tapping mode, in peak force QNM the feedback loop keeps the maximum force loaded on the tip. The system acquires and analyzes the individual force curves from each beat occurring during the imaging process, so that quantitative mechanical properties can be obtained simultaneously with high spatial resolution over the surface area. Thus peak force QNM has both the advantages from the tapping mode, namely, efficient scanning and low lateral shear, and from force mapping, namely, a well-defined magnitude of the applied force. In addition, peak force QNM enables the feature that automatically adjusts the scanning parameters in real time to optimize the image and protect the probe and sample, although this option has not been helpful for extremely soft samples such as bubbles or droplets.

By peak force QNM, Walczyk, Schön, and Schönherr (2013) imaged nanobubbles under an imaging force ranging from 0.24 to 27 nN. The profile of a surface nanobubble from a low force peak force QNM measurement is comparable to that obtained by tapping mode AFM. Stronger imaging forces led to less high nanobubble (or nanodroplet) profiles. Zhao *et al.* (2013) obtained the stiffness of nanobubbles quantitatively by peak force QNM measurements. With the known tip radius and cantilever stiffness from the calibrations, the mechanical measurements show that nanobubbles behave like a simple spring: the height decreased linearly with the force. Their findings are discussed further in Sec. IV.

4. Bubble and droplet deformation by AFM tip

We now discuss a dilemma which holds for all AFM techniques: Can an AFM tip be ever gentle enough to reveal the true profiles of surface nanobubbles and nanodroplets? As the morphology of surface nanobubbles and nanodroplets is sensitive to the interactions with the AFM tip, many parameters including cantilever stiffness, tip radius and cleanness, and the imaging parameters (e.g., scan rate and set point) all affect the fidelity of their morphologic images. The general experience from imaging soft matters, such as biological macromolecules, is also relevant for imaging nanobubbles and nanodroplets. Note that the scan rate must be optimized: a slow scan (less than 5 μm/s) does not necessarily produce more stable images than a fast scan, possibly due to shorter duration for the tip-bubble interactions. Borkent *et al.* (2010) investigated how the profiles of nanobubbles depend on the tip types and tip cleanness. A hydrophilic tip gives more stable and sharper images.

For those nanobubbles or nanodroplets with highly curved profiles, a quantitive reconstruction of the real profiles also requires the consideration of the broadening effect from the tip-sample convolution (Garcia and Perez, 2002). This effect has implications on the contact angle obtained from AFM images. Borkent *et al.* (2010) obtained the tip shape correction by using the HOPG step as a reference. Song, Walczyk, and Schönherr (2011) explored this approach to obtain contact angles of nanobubbles by three-dimensional fitting of AFM data, shown in Fig. 10. However, the tip-sample interaction will also affect how to deconvolute the AFM images; see, e.g., Walczyk, Hain, and Schönherr (2014) and Walczyk and Schönherr (2014). We discuss this tip-sample interaction and the contact angle of nanobubbles in detail in the next section.

The nanobubble imaging becomes even more challenging when the bubbles become softer or very small. For example, as interfacial tension of gas-liquid interface is reduced by the addition of surfactants or organic solvents in the liquid phase or for oil nanodroplets, the nanobubbles or nanodroplets may even become invisible to AFM due to strong deformation (Zhang, Uddin *et al.*, 2012).

We finally again stress the various limitations in the application of AFM to nanobubble studies: (i) AFM cannot provide the chemical identity of the structures and therefore cannot distinguish nanobubbles from other types of objects. This limitation has led to erroneous interpretations of various AFM images; see the discussion in Sec. II.F. It is clear that in order to draw reliable conclusions on the presence of nanobubbles at an interface from AFM images, the substrate has to be carefully characterized both in air and in the aqueous environment. But this by far is not enough: Attention must also be paid to potential alternation of the surface morphology in the immersed conditions, e.g., by surface nanodroplets or contamination. An independent verification of the gaseous

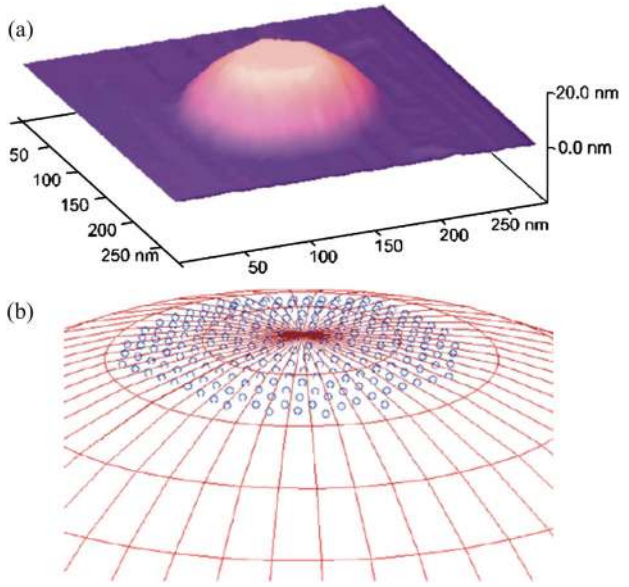

FIG. 10 (color online). (a) AFM height image of a nanobubble (footprint diameter 210 nm) and (b) 3D spherical-cap fit (mesh) of the AFM data points indicated by the open circles. The nanobubble is only a small part of a sphere, namely, down to the second ring (diameter 210 nm corresponding to the footprint diameter). From Song, Walczyk, and Schönherr, 2011.

nature of the nanobubbles, e.g., by degassing experiments or in combination with other complementary techniques, is highly desirable. (ii) Full-size imaging by AFM is usually time consuming. This precludes AFM from studies of the fast dynamics of nanobubbles, such as their formation or their moving contact line. (iii) Along this line, AFM imaging requires a mechanically and chemically stable environment. So it cannot follow the response of nanobubbles to some external field, for example, ultrasound.

To put it in a nutshell, AFM has wonderful spatial resolution, but at the same time AFM is slow, chemically blind, and intrusive. Therefore, we need alternative observation techniques beyond AFM which we discuss in the next sections.

B. Optical microscopy

Several optical techniques have been applied to study nanobubbles and nanodroplets. Compared to AFMs, they are direct, nonintrusive, and fast. In particular, fast optical movies can potentially capture the nucleation of nanobubbles and nanodroplets. But they are limited by the spatial resolution and can mainly offer lateral resolution of the nanobubbles or nanodroplets. Therefore it is nearly impossible to get the volume of nanobubbles or nanodroplets from optical microscopy.

Normal optical microscopy can resolve the bubbles with a large lateral diameter wider than about 1.5 μm, as shown in Fig. 11(a), and in combination with a fast camera, can record the nanobubble dynamics (Zhang *et al.*, 2014). Much smaller nanobubbles can be resolved only by much more sophisticated optical techniques, which are discussed later.

1. Interference-enhanced reflection microscopy

In this technique, a planar surface with suitable auxiliary layers is used to increase the reflected intensity contrast between bare surface areas and regions covered by thin transparent objects (Köhler, Lazar, and Riegler, 2006). A depth resolution of a few angstroms can be achieved with a time resolution better than 1 s (Köhler, Lazar, and Riegler, 2006). Karpitschka *et al.* (2012) applied this technique to visualize nanobubbles. An artificially grown oxide (silica) layer of 300 nm on silicon wafers was used as a substrate. The setup is shown in Fig. 11(b). Surface nanobubbles were visualized by this technique and correlated to the corresponding AFM images collected in the same surface area. The work clearly showed that nanobubbles exist without any intrusive perturbation (such as AFM causes), and that they form within a few seconds after the solvent exchange. The optical movies could further reveal that nanobubbles did not always form at the same spots, suggesting that their growth was not dominated by preferred or active surface sites. The nucleation took place within 37 s after the start of the liquid exchange, consistent with the previous (not spatially resolving) QCM measurements (Zhang, 2008).

2. Attenuated total internal reflection

An alternative optical technique is attenuated total internal reflection (ATR), which has been used in combination with fluorescence spectroscopy (TIRF), infrared spectroscopy [ATR Fourier transform infrared (FTIR)], Raman spectroscopy (ATR-Raman spectroscopy), and other spectroscopic methods. The detected region in the ATR configuration is

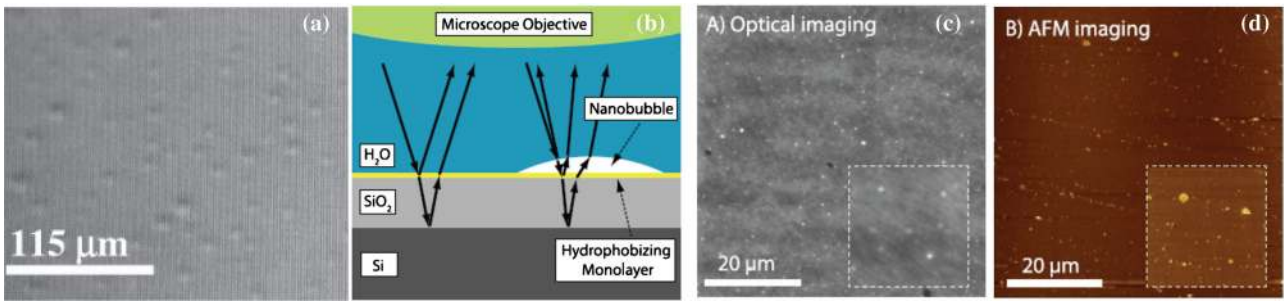

FIG. 11 (color online). (a) Reflection mode optical images of bubbles formed by the solvent exchange on a flat OTS-Si substrate. From Zhang, Maeda, and Craig, 2006. (b) Setup of interference-enhanced reflection microscopy, (c) the resulting optical images of surface nanobubbles, and (d) the corresponding AFM images of the surface nanobubbles produced under the same conditions on the same substrate. From Karpitschka *et al.*, 2012.

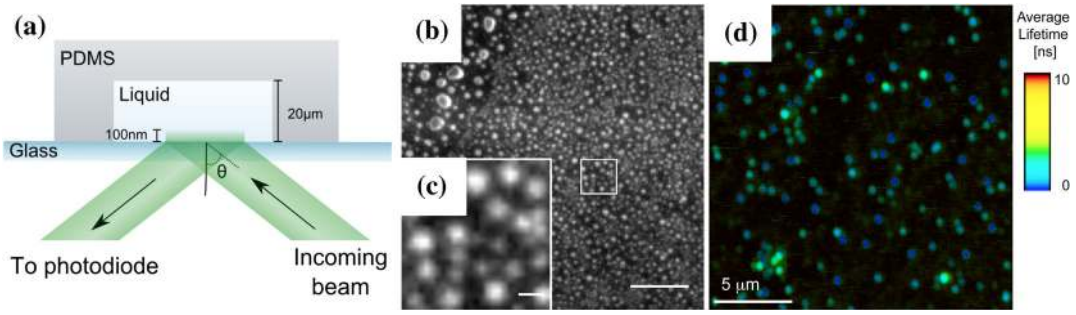

FIG. 12 (color online). (a) Schematic of TIRF setup; (b), (c) surface nanobubbles observed under TIRF microscopy. The scale bars are 5 μm. The square area in (c) is a zoomed-in area of (b); the scale bar now is 500 nm. From Chan and Ohl, 2012. (d) FLIM image of surface nanobubbles on glass imaged in aqueous solution containing 100 nM ATTO-465 dye after a partial ethanol-water exchange. The glass was cleaned prior to the ethanol-water exchange with piranha solution. The ATTO-465 dye partitions to the gas-liquid interface, where it can be identified via its characteristic excited state lifetime of $\tau_{\text{gas-liquid}} = 2.6$ ns compared to the molecularly dissolved dye ($\tau_{\text{water}} = 5.3$ ns). The image has been false colored to highlight the locations, where the characteristic lifetime $\tau_{\text{gas-liquid}}$ was detected. From Hain *et al.*, 2015.

determined by the penetration depth of the light (evanescent field), which is related to the refractive index of the substrate and the liquid medium, incident angle of the light, and its wavelength. The details of the relevant optics and fundamental instrumentation on ATR can be found in Hansen (1973) or Banwell (1983). The high sensitivity to objects adjacent to the substrate makes the configuration of ATR especially effective in studying surface nanobubbles and nanodroplets. So far two out of this family of techniques based on the total internal reflection have been applied to nanobubbles or nanodroplets, namely, TIRF and ATR FTIR.

Chan and Ohl (2012) applied TIRF microscopy to visualize the formation of nanobubbles during the solvent exchange process. A fluorescent dye (rhodamine) was doped into water to provide the contrast. A penetration depth in the setup was approximately 70 nm from a hydrophilic glass sealed inside a polydimethylsiloxane (PDMS) microchannel. The technique allowed one to detect nanobubbles with diameters of 230 nm and above, with a rate of 18 frames/s. Images of surface nanobubbles observed under TIRF microscopy are shown in Fig. 12. The results of Chan and Ohl (2012) suggested that when ethanol was replaced by water, many nanobubbles nucleated within about 10 s. The flow rate of the solvent exchange process affected the nucleation rate: at higher flow rates, nucleation was completed almost instantly, while at a slower rate, it took several minutes. Stable nanobubbles appeared only after the later stage exchange and continuously formed even after completion of the solvent exchange. Later concerns were cast onto the nature of those nanobubbles, as PDMS could be a source of contamination (An, Liu, and Craig, 2015).

Clearly, the TIRF technique should be further exploited in the research of surface nanobubbles, best under extremely well-defined surface and solvent conditions. From our point of view TIRF can potentially provide the highly desired information on the dynamics of nanobubbles and nanodroplets: their nucleation and growth, and their response to external fields. Although there may be effects from the dye used for visualization, such effects can be addressed by varying the dye concentration or comparing different dyes.

3. High-resolution fluorescence microscopy

Confocal microscopy can provide a high spatial resolution bottom view of dyed surface nanodroplets. Zhang, Wang *et al.* (2015) tracked the lateral size of dissolving methylmethacrylate nanodroplets as a function of time. They found partial pinning of the contact line through which the droplet center shifted to one side of the droplet as shown in Fig. 13. Complementary contact angle measurements by disruptive polymerization of the nanodroplets supported the fact that the surface nanodroplets dissolved in a mixed stick-slide mode: Alternately, both the lateral size and the contact angle decrease during the dissolution. We discuss various droplet dissolution modes in detail in Sec. VI.F.

In recent work Hain *et al.* (2015) combined time correlated single photon counting (TCSPC) with fluorescence lifetime imaging microscopy (FLIM), applied to very small areas, being only a few times larger than the nanobubbles themselves. From the lifetimes τ_i of the fluorescence signal $I(t) = \Sigma_i I_i \exp(-t/\tau_i)$ the nature of the interfaces (i) to which the (fluorescent) rhodamine dye adsorbed at—namely, either solid-water, gas-water, or PDMS-water—could be deduced,

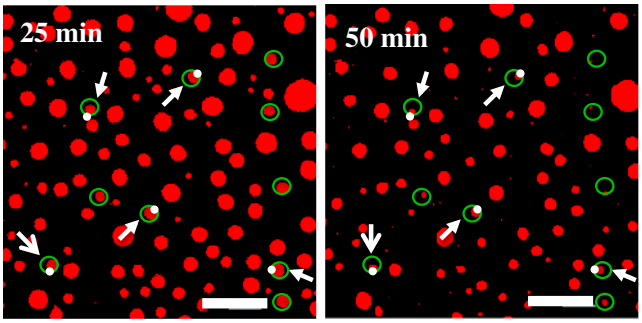

FIG. 13 (color online). Confocal images of surface nanodroplets of methylmethacrylate (MMA) after 25 and 50 min in stationary, originally pure water. The droplets were dyed by rhodamine 6G. As seen from the two images, the droplet center shifted as the lateral size of the droplet shrank, clearly demonstrating the pinning effect on the three-phase boundary. The scale bars correspond to 40 μm. From Zhang, Wang *et al.*, 2015.

demonstrating the gaseous character of the nanobubbles in their case. This was also supported by the dissolution of the surface nanobubbles in degassed water. They moreover combined this technique with AFM and were able to correlate spots of fluorescence light emission with individual nanobubbles in the AFM image of the same area.

Another important observation in this context is that in the nanobubble nucleation experiments by Hain *et al.* (2015), nanobubbles emerge only after piranha cleaning of the glass surfaces, which causes presumably surface roughness and little crevices on which the nanobubbles can nucleate and pin. In contrast, Hain *et al.* (2015) did not observe nanobubbles on plasma-cleaned or UV and ozone-cleaned glass surfaces by combined AFM-FLIM measurements.

C. Other techniques with high spatial resolution

1. Scattering and transmission x ray

Length scales much smaller than the optically accessible ones can be reached with x rays. L. Zhang *et al.* (2013) explored synchrotron-based scanning transmission soft x-ray microscopy (STXM) to investigate surface nanobubbles with a nanometer resolution. The setup is shown in Fig. 14. The solution was sandwiched between two silicon nitride windows with a solution of volume of about $2-3\ \mu\ell$. Neon and SF_6 bubbles with a lateral size less than 1 μm could be visualized in a gas-containing α-cyclodextrin solution and in an urea solution (see Fig. 14), but not in degassed solutions. This shows the existence of surface nanobubbles of these gases in these solutions for the given substrates.

The strength of x-ray spectroscopy is that the gas types can be determined from the measurements that also have a good spatial resolution. Moreover, x-ray spectroscopy is less intrusive than AFM, although also somewhat intrusive as x rays can nucleate bubbles. At the moment, the technique is still slow, particularly in the acquisition of highly resolved images.

We again stress that the nanobubbles detected by STXM are sandwiched between the walls of tiny fluid cells with typical volume of a microliter. The morphology and stability of these nanboubbles can be different from those sitting on an isolated substrate immersed in a large pool of liquid where AFM images and other optical microscopy took place. Under such confinement, the system can establish an equilibrium quickly.

2. *In situ* transmission electronic microscopy

The measurements by *in situ* transmission electronic microscopy (TEM) now discussed are only for nanobubbles confined to a very small volume of liquid. *In situ* transmission electronic microscopy has recently been used for the characterization of the nanobubble nucleation process, possessing superb spatial and temporal resolution. The setup is shown in Fig. 15. So far the nanobubbles observed with this technique formed either from electrolytic reaction or from *in situ* radiolysis of water under the irradiation of a high-dose electron beam in Fig. 16.

Liu and Dillon (2014) followed the evolution of electrolytically generated hydrogen on Au electrodes in $0.1M$ H_2SO_4 solution by *in situ* TEM. At the beginning the produced gas molecules dissolved into the solution and then formed a bubble that is isolated from the gold electrode by a 6–8 nm liquid layer. Eventually the bubble adsorbed onto the electrodes as shown in Fig. 17. This observation is different from the general thought that the nanobubble nucleation originates from the electrode surface, but shows that the nucleation may be favorable in the electrical double layer or region with steep composition gradients rather than from the electrode surface.

Also by *in situ* electronic transmission microscopy, Huang *et al.* (2013) demonstrated that hydrogen nanobubbles can be generated and stabilized in a protein solution via radiolysis. An electron beam served as a radiation source and at the same time as an imaging probe, while the protein acted as a

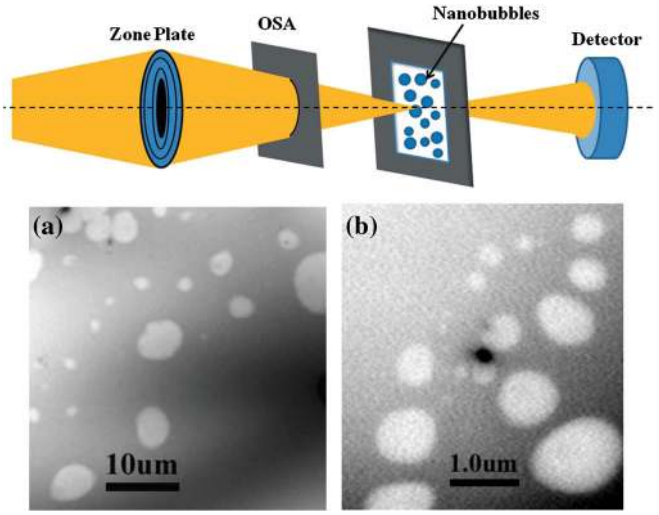

FIG. 14 (color online). Detection of nanobubbles by synchrotron-based scanning transmission soft x-ray microscopy (STXM) with nanometric resolution. Schematics of the setup (upper) and the images (lower): (a) STXM transmission image of neon nanobubbles sitting on a Si_3N_4 window. (b) STXM transmission image of SF_6 nanobubbles on the same substrate. From L. Zhang *et al.*, 2013.

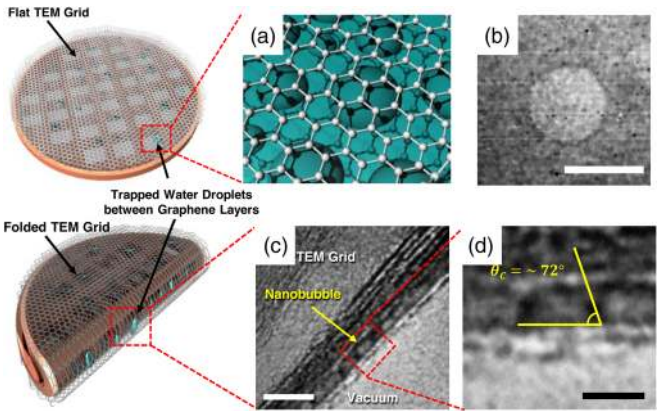

FIG. 15 (color online). Visualization of nanobubbles by *in situ* TEM. (a) Water was trapped between graphene membranes for nanobubble visualization in low dose electron irradiation. (b) The top view of a nanobubble. (c) The graphene membrane is flexible and can be folded up, allowing the side view of nanobubbles encapsulated inside the membrane. (c), (d) The contact angle of the nanobubbles was measured to be 72°. From Shin *et al.*, 2015.

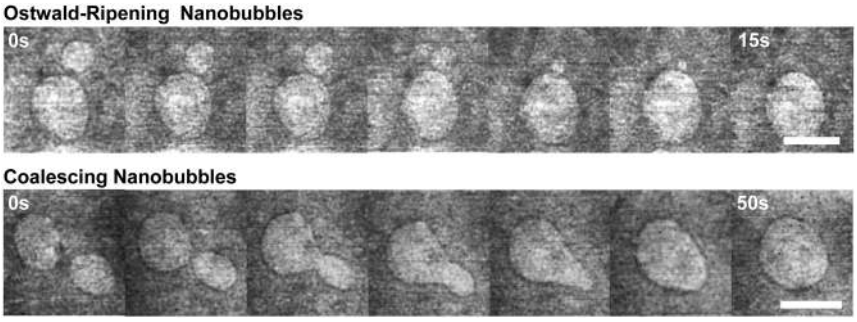

FIG. 16. Snapshots of TEM images showing the merging of two adjacent nanobubbles observed for 15 and 50 s, respectively. When the nanobubble sizes are significantly different, an Ostwald ripeninglike process is observed, with the smaller nanobubble shrinking and the larger one growing (upper line). In contrast, similar-sized nanobubbles simply coalesce (lower line). The scale bars are only 10 nm. From Shin *et al.*, 2015.

scavenger of hydroxyle radicals so that hydrogen molecules could be generated. An image reconstruction method was applied to extract the morphology and the contact angle of the nanobubbles from the TEM images. The pressure inside those nanobubbles was estimated to be 15–75 atm, so Huang *et al.* (2013) concluded that the hydrogen nanobubbles were in a "dense gas" phase. The nanobubbles dissolved or grew, depending on the competition between the dissolution rate and the generation rate of the hydrogen. Big nanobubbles were found to influence the growth rate of neighboring nanobubbles and gas transfer from small bubbles to big bubbles, but also vice versa was found.

Later Shin *et al.* (2015) used TEM to directly visualize surface nanobubbles in encapsulated water confined in a graphene membrane. The thin liquid film between two merging nanobubbles was clearly visualized and followed in time during the merging process, as shown in Fig. 16. Impressively, Shin *et al.* (2015) could even obtain the side view of nanobubbles with a diameter from 5 to 15 nm, when the graphene fluid cell was folded. For top and side views of these small surface nanobubbles see Figs. 16 and 15, respectively.

By using a higher dose rate of electron beam, Grogan *et al.* (2014) induced nanobubble formation from radiolysis of water and then followed the nanobubble growth dynamics. They observed that after bubble nucleation, growth, and detachment, the next bubble repeated the process at the very same spot. This suggests that chemical heterogeneities on the surface played a role for the bubble nucleation. In fact, the bubbles reproducibly grew at a nearly constant rate of 70 nm/s, nucleated at a frequency of 0.3 kHz, and detached at the radius of 190 nm in 3.1 s, as shown in Fig. 18(b). A simplified reaction-diffusion model could explain the nanobubble growth and detachment. Essentially, the continuous irradiation leads to a steady-state H_2 concentration, which is in between the saturation concentration and the concentration required for homogenous nucleation. The periodic nanoscale bubble formation showed that the system was in a dynamic equilibrium, balancing bubble nucleation and growth with bubble detachment.

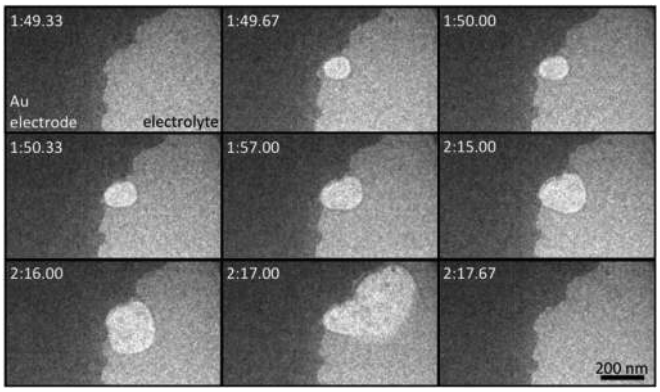

FIG. 17. Time-lapse TEM images showing nucleation and growth of electrolytically generated gas nanobubbles at a gold electrode at −2 V. From Liu and Dillon, 2014.

D. Techniques with low spatial resolution

The advantage of AFM is to have excellent spatial resolution, but as put in a nutshell above: It has no chemical sensitivity and is slow and intrusive. So we need techniques that provide *complementary* information to AFM, i.e., techniques that can provide information on the chemical nature of the objects at the surface and that are faster. Such techniques are presented in this section, but the price one has to pay is that these techniques do not have adequate spatial resolution: The signal from the measurements is always averaged over the detection area which is much larger than the size of the nanobubbles.

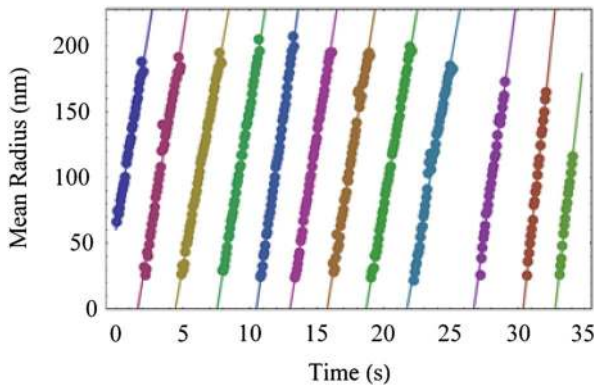

FIG. 18 (color online). The mean bubble radius as a function of time. Nanobubbles were induced by a high-dose electron beam and visualized by environmental transmission electron microscopy. Colored circles represent experimental data and lines are linear fits. From Grogan *et al.*, 2014.

1. Molecular spectroscopy by attenuated total reflection Fourier transform infrared

Detection of surface nanobubbles by ATR-FTIR requires that the gas inside nanobubbles is infrared (IR) active. Many gases, such as CO_2, CO, CH_4, C_2H_8, or water vapor, strongly absorb infrared (Banwell, 1983). Particularly suited for IR studies is CO_2 as the IR spectrum of gaseous CO_2 consists of two branches with fine lines (at $\approx 2300 - 2380$ cm^{-1}), while the IR spectrum of aqueous CO_2 is a single band (at ≈ 2340 cm^{-1}). The IR spectra can thus reveal whether the CO_2 molecules are in the gaseous state or the aqueous state.

An early attempt to characterize adsorbed CO_2 molecules at the solid-liquid interface by ATR-FTIR was undertaken by Gong *et al.* (1999). They exposed a ZnSe crystal to an aqueous dispersion and measured the IR spectrum of CO_2, which not only displayed the aqueous CO_2 adsorption in a hydrophilic silica dispersion, but also showed the characteristics of gaseous CO_2. Gong *et al.* (1999) speculated that CO_2 gas might be present on the surface of the hydrophobic silica in the form of small, submicron-sized bubbles, giving rise to the gaseous spectra.

Zhang, Khan, and Ducker (2007) for the first time obtained ATR-FTIR spectra of surface nanobubbles. In their experiments, CO_2 nanobubbles were produced on a hydrophobic Si prism by the exchange of CO_2-saturated ethanol and CO_2-saturated water. A full spectrum was first collected when the substrate was directly immersed in CO_2-saturated water in the state without surface nanobubbles, as confirmed by AFM imaging. This full spectrum served as a background for a difference spectrum that was then collected after the solvent exchange process, as shown in Fig. 19. The difference spectrum shows two groups of distinctive fine peaks that were attributed to CO_2 gas molecules, demonstrating the formation of gaseous CO_2 bubbles by the solvent exchange. The height of the fine peaks is determined by the amount of gas molecules inside nanobubbles.

The difference spectrum from the same measurement also showed weaker intensity of infrared peaks attributed to any chemicals in the liquid phase (such as D_2O or aqueous CO_2) after the formation of nanobubbles, due to the depletion of the liquid phase from the volume which was occupied by the gaseous bubbles. From the infrared intensity from chemicals in the liquid phase, the volume loss of the liquid (i.e., the volume of the nanobubbles) can be determined. Together with the amount of gas molecules determined from the CO_2 gaseous peaks, the average density of gas inside the nanobubbles can be obtained. Assuming the ideal gas law, the calculated pressure inside the bubbles was around 1.1 ± 0.4 atm. This is consistent with the pressure inside a typically sized surface nanobubble in the corresponding AFM image (Laplace pressure and atmospheric pressure).

Furthermore, Zhang, Quinn, and Ducker (2008) showed from the spectra that the adsorption of gaseous CO_2 slowly decreases with time, indicating that CO_2 leaks out from the nanobubbles and that therefore the partial pressure of CO_2 inside the bubbles decreases. This may be the first measurements on the dynamics of surface nanobubbles, which as we see in Sec. VI is crucial for their theoretical understanding and indeed CO_2 bubbles have a particularly fast dynamics due to the good solubility of CO_2 in water.

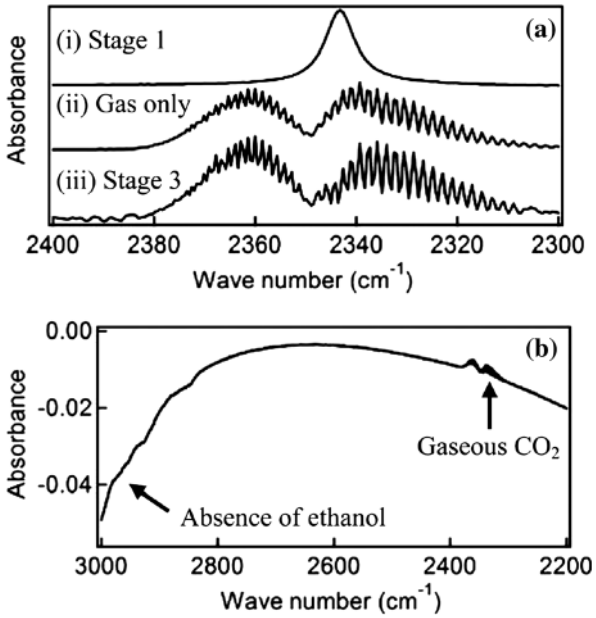

FIG. 19. ATR-FTIR spectra of the surface of a hydrophobized silicon. (a) Detail of the CO_2 absorption band. (i) Stage 1: CO_2-saturated water. The background spectrum is air-equilibrated water. The spectrum shows the presence of aqueous CO_2. (ii) Standard CO_2 gas spectrum. (iii) Stage 3 of the solvent exchange: This is the difference spectrum with the spectrum at stage 1 as the background. The spectrum shows the presence of CO_2 gas molecules as in (ii), and a weaker aqueous CO_2 band at $2337 - 2348$ cm^{-1} due to depletion of liquid by nanobubbles in the detected interfacial region. There was less liquid, compared to the background spectrum. (b) Same as (iii) in (a), but now a wider scan is shown, demonstrating the absence of ethanol at 2980 cm^{-1}. So the ethanol was completely removed by water from the system. From Zhang, Khan, and Ducker, 2007.

The above ATR-FTIR spectra of surface nanobubbles have laid a cornerstone for the nanobubble research, because the gaseous spectra serve as unambiguous evidence for the existence of surface nanobubbles. Since then the field has moved away from the debate whether nanobubbles exist toward the investigation on their stability mechanism.

2. Surface plasmon resonance spectroscopy

Surface plasmon resonance (SPR) spectroscopy is a technique that is widely used to detect changes in the refractive index of an adsorbed layer on or near an SPR-active surface (Shumaker-Parry and Campbell, 2004). It does not have the chemical specificity of infrared spectroscopy, but can be used to detect surface nanobubbles as they give rise to a lower refractive index of the layer adjacent to the surface.

Zhang, Khan, and Ducker (2007) applied SPR to detect nanobubbles on a decanethiol-coated gold surface. After the solvent exchange process (stage 3, cf. Fig. 6), the resonant angle in the SPR spectrum shifted to a lower value relative to the reference in water (stage 1). Such a shift demonstrates that the material introduced by the solvent exchange has a lower refractive index than water. This is entirely consistent with the formation of gaseous bubbles.

Martinez and Stroeve (2007) also observed the shift of the SPR reflectivity after the exchange of an ethanol solution by a salt solution, which is consistent with a layer of gas formed at the interface. They followed the composition of the layer by SPR and found that the nanobubble layers are short lived. The interface of hydrophobic surface in water gradually changed with time and turned into a layer of organic characteristics after 30 h.

In principle, the coverage of the adsorbed gaseous layer can quantitatively be estimated from the SPR data. However, this is difficult for nanobubbles because the adsorbed gas molecules are not in the form of a continuous film, but occur as individual nanobubbles with some lateral size and number density distribution.

3. Quartz crystal microbalance

In quartz crystal microbalance (QCM) measurements, a thin quartz crystal sensor is excited to oscillate at its resonance frequency, which depends on the total mass of the sensor and the adhering layers on the surface. If the adsorbed layer is thin and rigid, the shift of the resonance frequency can be well described by the Sauerbrey equation (Rodahl *et al.*, 1995). With QCM one can thus continuously and on a fast time scale quantitatively monitor absorption phenomena on the crystal surface. The method has been frequently used in electrochemistry, surface science, and biology. In the context of surface nanobubbles, the presence of nanobubbles on the quartz sensor surface affects the response of QCM drastically due to the depletion of water from the sensor surface. Thanks to the extremely high sensitivity and fast response of the QCM, the method can probe the early stages of surface nanobubble nucleation at the water-solid interfaces, which is not feasible with AFM measurements.

In early work, Carr *et al.* (1989) demonstrated the feasibility of electrochemical QCM for detection of bubble nucleation. Here the gold-coated electrode also served as the working electrode in electrochemical reaction. The formation of bubbles led to an increase in the resonance frequency. J. Yang *et al.* (2007) flushed the fluid cell with CO_2-saturated water to form nanobubbles. Compared to the frequency in milli-Q water, a frequency increase was observed on TMCS-modified gold, but not on mildly contaminated clean gold. This is consistent with the formation of surface nanobubbles only on hydrophobic surfaces (Yang *et al.*, 2003).

Zhang (2008) simultaneously measured both frequency and dissipation shift by QCM-D (where "D" stands for "dissipation") after the solvent exchange. Her measurements showed that the frequency of QCM increased (because of the depletion of coupled water) and the dissipation decreased (because of less energy dissipation on the oscillating crystal), consistent with the formation of nanobubbles on a hydrophobized gold-coated sensor. Furthermore, the QCM-D measurements could also reveal the short time scale for the nucleation of surface nanobubbles: As soon as the frequency and the dissipation can be measured ($\sim$1 min), the frequency shift and the dissipation reduction caused by the presence of nanobubbles had already occurred and remained the same afterward. This demonstrates that the nanobubble nucleation has in fact finished within 1 min and the bubbles are stable.

The frequency shift in QCM measurements is also conveniently applied to investigate the effects of nanobubbles on several interesting interfacial phenomena, such as the slip boundary conditions (Finger and Johannsmann, 2011) and the adsorption of biomolecules (Liu, Wu, and Craig, 2008; Liu and Craig, 2009).

E. Further techniques for the study of surface nanobubbles

Apart from the techniques discussed previously, several other techniques have also been used to examine the surface nanobubbles, namely, neutron reflectivity measurements (Schwendel *et al.*, 2003; Steitz *et al.*, 2003) and small angle x-ray scattering (Palmer, Cookson, and Lamb, 2011).

Also a range of techniques that are available in biological imaging, catalytic chemistry, and surface science may be useful for nanobubble studies too, although they have not been used so far, namely, vibrational sum-frequency spectroscopy (Du *et al.*, 1993; Tyrode, Rutland, and Bain, 2008), tender energy x-ray adsorption spectroscopy in a liquid environment (Velasco-Velez *et al.*, 2014), and a high sensitive weighing device, nanomechanic resonators (Burg *et al.*, 2007). These techniques have impressive resolution or are ultrasensitive to certain molecular structures. The implementation of these techniques to surface nanobubble study may provide complementary information on nanobubble properties and their interactions with the environment. Presently, in the context of catalysis such techniques as, e.g., an integrated AFM-Raman instrument or time-resolved tip-enhanced Raman spectroscopy, both of which can monitor photocatalytic reactions at the nanoscale, are being developed (Harvey *et al.*, 2012; Woods and Bain, 2012; van Schrojenstein Lantman *et al.*, 2012) and should also be applied to surface nanobubbles.

In summary, a wide range of techniques have been applied to characterize the morphology of nanobubbles and nanodroplets with high spatial and temporal resolution. In parallel, several kinds of molecular spectroscopy have also been employed to provide their chemical identities. Up to now different techniques have been combined in measurements under the same conditions. However, we have to assume that under these same conditions nanobubbles of at least similar size or number density were produced both for the space-averaging techniques and for the techniques with a high spatial resolution. This however is often not the case, as unfortunately hitherto no protocol has been established which precisely controls the size distribution and surface coverage of nanobubbles. Even in the same experiment, the size of nanobubbles varies with the locations on the surface. Therefore the field is in need of really simultaneous techniques, such as AFM combined with fluorescent spectroscopy, TCSPC combined with FLIM (Hain *et al.*, 2015), x-ray spectroscopy with high spatial resolution, or electron energy-loss spectrometry in TEM, to obtain the spectroscopy of a single surface nanobubble under well-defined conditions.

IV. PROPERTIES OF SURFACE NANOBUBBLES AND NANODROPLETS

In the two previous sections we discussed in detail how to make and how to observe surface nanobubbles and surface

nanodroplets. In this section we review the properties of surface nanobubbles and, in particular, their morphology (i.e., their shape), their long-term stability and their stability against rather violent changes of the external conditions, and finally their collective effects. A general feature is that in nanobubble and nanodroplet populations, not every individual possesses identical properties. They show individuality in all aspects, which can be rationalized by the local heterogeneities on the surface and cooperative effects among neighboring nanobubbles, i.e., different local gas concentrations.

Given the various potential artifacts in nanobubble studies described in Sec. II.F, here we are confronted with the difficulty of judging whether the generated features on a surface reported are indeed nanobubbles or rather nanodroplets or artifacts. We address this question for those studies for which we think it is relevant and for which from our point of view there is a particular danger of surface nanodroplet or artifact formation.

A. Morphological characteristics

The morphology of nanobubbles is related to chemical and physical properties of the substrate. Large, sparse defects on the substrate can lead to irregularities of the three-phase contact line of the nanobubbles, reminiscent of a pinned triple line as described by de Gennes, Brochard-Wyart, and Quere (2004). But also for substrates that are considered to be very smooth, pinning at nanoscopic heterogeneities can be deceiving, as we will see later.

The typical shape of nanobubbles is spherical caplike with a circular three-phase boundary (see Fig. 2). The height of these spherical-cap nanobubbles is on a nanometer scale, and the lateral extension can be up to several microns, implying a very small contact angle on the gas side, drastically different from the macroscopic counterpart. This contact angle of nanobubbles is extracted from spherical-cap fits to the AFM topographic images (Borkent *et al.*, 2010; Walczyk, Schön, and Schönherr, 2013) [see, e.g., Fig. 10(b)] or often for simplicity (but with the price of lack of accuracy) from the central cross-sectional profiles of nanobubbles.

The finding that the nanobubble contact angles are much smaller than their macroscopic counterparts has been confirmed in various AFM measurements in several complementary modes (Lou *et al.*, 2000, 2002; Tyrrell and Attard, 2001; Holmberg *et al.*, 2003; J. Yang *et al.*, 2003; Simonsen, Hansen, and Klösgen, 2004; Zhang *et al.*, 2004; S. Yang *et al.*, 2007; Borkent *et al.*, 2010; Song, Walczyk, and Schönherr, 2011; Zhang, Ren *et al.*, 2012; Walczyk, Schön, and Schönherr, 2013; Zhao *et al.*, 2013; H. Yang *et al.*, 2014). For a collection of measured contact angles see Table I. So far the highest contact angles of nanobubbles in unconfined space reported are only 50° (S. Yang *et al.*, 2007) to 60° (Zhang *et al.*, 2010).

It was proposed that the large difference between microscopic and macroscopic contact angles was due to the effect of line tension (Ishida *et al.*, 2000; Yang *et al.*, 2003), representing the energy per unit length of the three-phase line, which becomes relevant for very small droplets and bubbles. This leads to a modification of Young's equation (1), namely, to (Gibbs, 1957; Boruvka and Neumann, 1977; de Gennes, 1985; de Gennes, Brochard-Wyart, and Quere, 2004)

$$\cos\theta = \frac{\sigma_{SL} - \sigma_{SG}}{\sigma_{LG}} - \frac{\tau}{\sigma_{LG} L} = \cos\theta_\infty - \frac{\tau}{\sigma_{LG} L}, \qquad (5)$$

where θ_∞ is the contact angle of an infinitely large bubble and τ is the line tension. Equation (5) thus implies a bubble size dependence of the contact angle. From the typical value $\tau \sim -(10^{-11} - 10^{-12})$ N obtained from theory (Getta and Dietrich, 1998) or MD simulations (Weijs *et al.*, 2011) one can extract the length scale below which line-tension effects should be relevant, namely, $\tau/\sigma_{LG} \sim 0.05 - 0.5$ nm.

However, all the experimental data require much larger line tension to account for the measured contact angle of nanobubbles. For example, Yang *et al.* (2003) fitted the observed size dependence of the contact angle of nanobubbles with the modified Young equation (5), obtaining an effective line tension of $\tau \sim 10^{-10}$ N, which is about 1 to 2 orders of magnitude larger than the theoretically expected value for molecular line tension (Getta and Dietrich, 1998; Weijs *et al.*, 2011). Kameda and Nakabayashi (2008) characterized surface nanobubbles on bare gold in water and in ethanol aqueous solutions. Figure 20(a) shows a plot of the cosine of the contact angle versus the inverse of the base radius (Kameda and Nakabayashi, 2008; Kameda, Sogoshi, and Nakabayashi, 2008). They found a positive line tension for the larger nanobubbles immersed in ethanol aqueous solution, but a negative line tension for the smaller nanobubbles immersed in water. The extracted line tensions were -2×10^{-10} and 5×10^{-11} N, respectively. Also those values are much larger than the theoretically expected value (Getta and Dietrich, 1998; Weijs *et al.*, 2011). In particular, the sign is not even consistent. In any case, it is clear that the effect of molecular line tension is too small to account for the observed size dependence of the contact angle. Equation (5) can at most be used as an effective description of the experimental findings.

What casts further doubt on the relevance of molecular line tension effects is that the linear dependence of $\cos\theta$ on the inverse nanobubble lateral extension L^{-1} as suggested by Eq. (5) is not always obeyed. Zhang, Maeda, and Craig (2006)

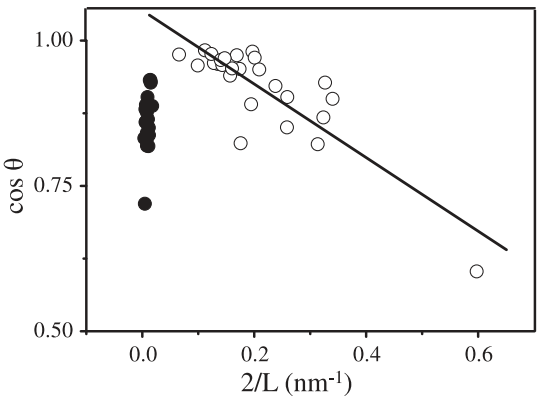

FIG. 20. Cosine of the contact angle of surface nanobubbles as a function of their inverse footprint radius $2/L$. Nanobubbles are in water (open circles) and much larger ones are in an ethanol aqueous solution (filled circles). The straight line results from a fit to the modified Young's equation (5), corresponding to a line tension of $\tau = -2 \times 10^{-10}$ N. From Kameda and Nakabayashi, 2008.

found the contact angle of nanobubbles to be almost constant when the radius of curvature of the nanobubbles on HOPG became larger than 650–700 nm. Zhang *et al.* (2010) obtained similar results for nanobubbles on both mica and HOPG.

One can expect that with the increase of the bubble size, the contact angle of nanobubbles should eventually approach the macroscopic value. But it is *a priori* not clear what conditions are required and we see in Sec. VI.D that this expectation is wrong. Indeed, Xu *et al.* (2014) observed that even for surface microbubbles that were as large as 8 μm in lateral extension, the contact angle was still much smaller than the macroscopic value. Clearly, the size dependence of the contact angle of nanobubbles is far more complicated than predicted by the linear relationship (5) suggested by line tension or even some sort of (much larger) effective line tension.

We now come to the contact angle of (immersed) surface nanodroplets. Munz and Mills (2014) measured the contact angles of the nanodroplets that were deposited from surfactant-stabilized emulsion and observed different contact angles for different droplet sizes. Also such size dependence was attributed to line tension, here from the fit estimated to be 10^{-10} N, which again is much larger than the theoretically expected value. Moreover, the relation between $\cos\theta$ and $1/L$ of nanodroplets need not be linear; see, e.g., Heim and Bonaccurso (2013).

Zhang, Ren *et al.* (2012) produced nanodroplets of polymerizable liquid on a solid surface immersed in an immersible liquid and converted them to polymeric nanolenses by photopoymerization. The morphology of the precursor nanodroplets was characterized by the protocol discussed in Fig. 9. It was again found that the difference between the contact angle of the nanodroplets and macroscopic value was too large to be explained by the effect of molecular line tension (Zhang, Ren *et al.*, 2012; Yang *et al.*, 2014), and that just as for nanobubbles the concept of line tension can at most be used as an effective description of some other underlying process.

The alternative and more correct interpretation for the morphology of nanobubbles is that the morphology of nanobubbles is determined by the pinning effects from very small scale imperfections on the surface. This can account for not only the contact angle of nanobubbles but also the evolution of the contact angle with the bubble lifetime (Lohse and Zhang, 2015). This mechanism is equally applicable to the morphology of surface nanobubbles. We discuss this interpretation in detail in Sec. VI.D.

B. Long lifetime

Already the early AFM observation of nanobubbles immediately indicated that nanobubbles could last at least for the time of the measurements, i.e., typically 10–15 min, which, as explained in the Introduction, was considered to be surprisingly long, given the small sizes of the bubbles. Many more examples of long lifetimes were found over the last one and one-half decade, but initially no quantitative and controlled experiments were done. Zhang, Quinn, and Ducker (2008) followed some air nanobubbles for two days in initially

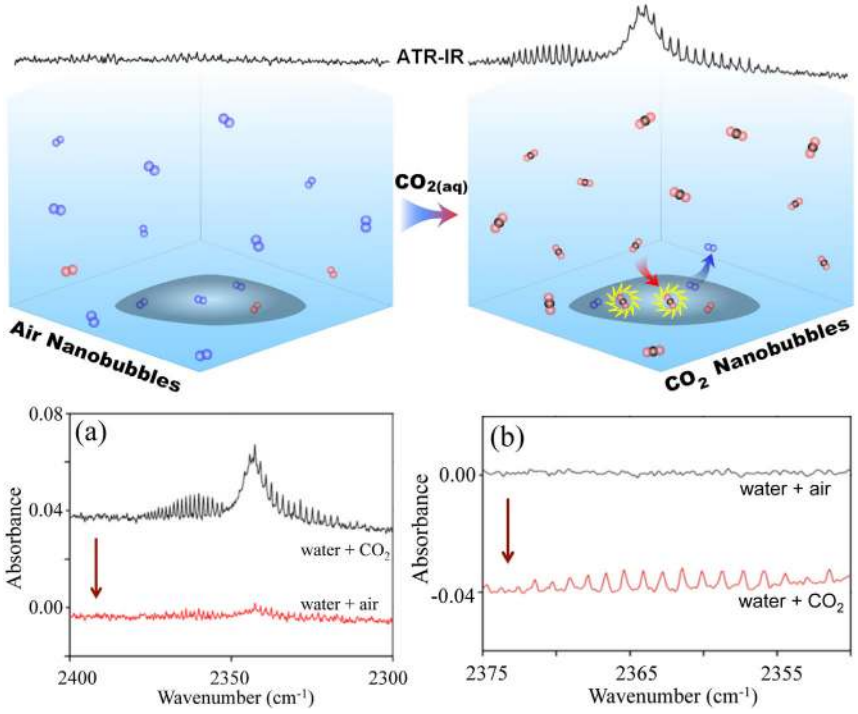

FIG. 21 (color online). Permeable gas-liquid interface of nanobubbles. The top sketch depicts the gas exchange between air nanobubbles and the surrounding CO_2-saturated water. The bottom panels show the ATR-FTIR spectra of nanobubbles in different liquid media. (a) Spectra before and after CO_2 bubbles were exposed to the air-equilibrated water. The gaseous CO_2 adsorption disappeared due to the replacement of CO_2 by air inside nanobubbles. (b) Spectra before and after air bubbles were exposed to the CO_2-saturated water. The gaseous CO_2 adsorption appeared due to the replacement of air by CO_2 inside nanobubbles. From German *et al.*, 2014.

air-saturated water in a closed fluid cell, to avoid the evaporation of the liquid.

On the other hand, in (partially) degassed water, the air nanobubbles shrink, which supports their gaseous nature. For example, after nanobubble formation in air-equilibrated water, Zhang, Chan *et al.* (2013) exposed these nanobubbles to partially degassed water with an (initial) saturation level of approximately 80%: Some nanobubbles disappeared immediately after the solvent exchange process; those remaining either disappeared later or shrank within the 14 h of observation time.

The dissolution of the surface nanobubbles is not only influenced by the gas concentration, but also by the type of dissolved gas. According to AFM images, in CO_2-saturated water nanobubbles dissolved faster than in air-saturated water. Small nanobubbles already shrank in size within 20 min, and then disappeared in 40 mins, which is in contrast to the stability for 3 days in air-equilibrated water (Zhang, Quinn, and Ducker, 2008; German *et al.*, 2014). The dissolution of CO_2 nanobubbles was also reflected in ATR-FTIR measurements. The gaseous CO_2 infrared adsorption from surface nanobubbles decreased gradually with time and disappeared after 60–70 min (Zhang, Quinn, and Ducker, 2008; German *et al.*, 2014). Why CO_2 nanobubbles shrink faster than air nanobubbles will be explained in Sec. VI. German *et al.* (2014) also demonstrated the diffusive exchange between nanobubbles and competing dissolved gases, demonstrating the permeability of the gas-water interface as shown in Fig. 21.

Next to gas concentration and gas type the surface properties also affect the surface nanobubble lifetime because of the pinning effect. Figure 22 shows the representative profiles of three dissolving bubbles obtained from AFM images. All three bubbles had become smaller after 14 h (Zhang, Chan *et al.*, 2013). A pronounced morphologic feature is that their volume decreased mainly by the decrease in height, while their lateral extension remained more or less constant. This morphological feature demonstrates the pinning on the three-phase contact line of the nanobubbles. In cases in which the lateral extension also shrank, the contact angle of the bubble became smaller or was unchanged (Zhang, Chan *et al.*, 2013; German *et al.*, 2014). In that case the strength of the "pinning" did not seem to be sufficiently strong to maintain the lateral extension constant until the end of the nanobubble lifetime. Consequently, there were jumps between the pinned phases during the bubble dissolution. This dissolution mode is similar to the mixed mode of stick slide that was observed for an evaporating droplet (Stauber *et al.*, 2014) and will be discussed in more detail in Sec. VI.F.

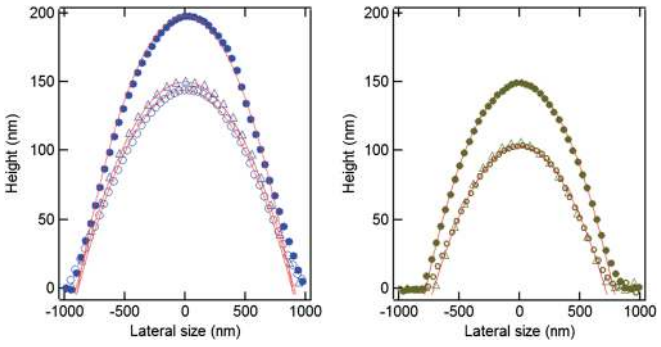

FIG. 22 (color online). Morphology of two surface nanobubbles during incubation in partially degassed water. Note that the level of dissolved gas during the incubation was not calibrated. The profiles of nanobubbles were measured at times of 0.25 h (solid bullets), 14 h (open triangles), and 20 h (open circles) in partially degassed water. The height of nanobubbles clearly decreased from 0.25 to 14 h, and no further change was observed from 14 to 20 h. From Zhang, Chan *et al.*, 2013.

We point out that the feature of the pinned three-phase contact line was also observed for growing nanobubbles, which will be discussed in Sec. IV.D. The volume increase of growing nanobubbles is achieved mainly by the increase of the height, while the lateral extension remains constant. The implications from the pinned boundary on the nanobubble stability are discussed in detail in Sec. VI.

The main problem with one-to-one comparison between theoretical and experimental lifetime for surface nanobubbles is that in most cases the experimental conditions for the nanobubble stability were not well controlled. One of the reasons is that the solubility of air in water is very sensitive to the temperature of the environment and to the details of how the water is handled. It is also often unclear to what degree the system is open or closed so that the gas concentration boundary conditions are not fully known. The random surface heterogeneities and the size distributions of nanobubbles make it complicated to quantify the effects from the pinning or from neighboring nanobubbles. The nanobubble study calls for well-controlled experiments of the lifetime and dissolution rate of nanobubbles and for quantitative data on the dissolution rate related to temperature, gas saturation level, gas types, and the surface heterogeneity. For microbubbles, Enriquez *et al.* (2013) built an elaborate device based on the idea to first saturate water with gas at some elevated pressure (up to 1 MPa) and then to apply a small pressure drop from saturation conditions, to create a controlled gas oversaturation. Using this device, Enriquez *et al.* (2014) could follow the diffusive dynamics of individual microbubbles generated in hydrophobic pits.

The problem of controlling the saturation level is less intricate for surface nanodroplets, as in general an oil saturation level is easier to control than a gas saturation level, namely, for nonvolatile oils. Otherwise, in principle dissolving surface nanodroplets share the same features as dissolving surface nanobubbles. Zhang, Wang *et al.* (2015) produced nanodroplets of oils that have different solubilities in water and measured the dissolution rate of those oil nanodroplets in pure water over time. The lifetime of surface nanodroplets is determined by the solubility and the saturation level of the droplet phase in water. Indeed, Zhang, Wang *et al.* (2015) found them to be stable in oil-saturated water (i.e., infinite lifetime), but they dissolved in pure water. The overall dissolution rate of oil nanodroplets was faster for oils with higher solubility in water. The dissolution rate was found to also be influenced by the initial size of the nanodroplets: Smaller droplets dissolved more slowly. Moreover, the dissolution rate was found to be different even for the droplets with the same initial size. Such individuality in the nanodroplet dissolution was ascribed to variations in the local surface heterogeneities and in local concentration gradients of

the dissolved oil that are influenced by neighboring oil droplets (Zhang, Wang *et al.*, 2015).

C. Nanobubble stability in aqueous solutions

What happens to nanobubbles in aqueous solutions, i.e., with salt or other solvents in water? Zhang, Maeda, and Craig (2006) showed that preformed nanobubbles do not disappear in salt solutions. Neither was there any difference in the nanobubble stability in different pH solutions, suggesting that the surface charges do not play any important role.

However, some care is required in connection with possible contaminations: From their observations Berkelaar, Zandvliet, and Lohse (2013) had claimed the stability of nanobubbles in aqueous NaCl droplets, up to the very end of the droplet evaporation process and the formation of salt crystals. However, later they gave evidence that the nanobubbles of their prior salty droplet drying experiments might in fact be PDMS nanodroplets (Berkelaar *et al.*, 2014).

How do surface nanobubbles behave in organic aqueous solutions? They turn out to be stable in many aqueous solutions such as protein solutions or nanoparticle solutions. For example, Wu *et al.* (2008) showed that nanobubbles remained stable during the evaporation of protein solution and created cavities on the deposited protein film after drying. In the evaporation of nanoparticle suspension droplets, the surface nanobubbles templated the emerging pattern of the nanoparticles (Darwich *et al.*, 2011), leading to nanorings of gold nanoparticles around the footprint of the original nanobubble. Nanobubbles also remained stable in electrochemical reactions during the deposition of a conductive polymer film and led to nanoholes on the polymer film (Hui *et al.*, 2009). All these processes are similar to what was seen for the evaporating salty droplet (Berkelaar, Zandvliet, and Lohse, 2013) and we take them as indication for the strong pinning that the nanobubbles or nanodroplets experience under those conditions.

But surface nanobubbles are not stable in alcohol (Zhang, Wu *et al.*, 2005; Hampton, Donose, and Nguyen, 2008), though short-chain alcohols are often used as the first solvent in the formation of nanobubbles by the solvent exchange. The reason lies in the good wetting property of the alcohol, which displaces bubbles from the surface.

Finally, we comment on surface nanobubbles in other nonaqueous liquids: So far nanobubbles have not been reported in such liquids, but only because the research has mainly focused on water. We expect that water is not special with respect to the existence of surface nanobubbles and we do not see any reason why other liquids should not host them. In particular, we expect surface nanobubbles in liquids with low solubility for gases which can easily be oversaturated with gas.

D. Nanobubble response to external fields

1. Response to mechanical load

The mechanical properties of the gas-liquid (liquid-liquid) interface of surface nanobubbles (nanodroplets) can best be examined by an AFM tip, operated in the peak force mode; see Sec. III. Employing this method Zhao *et al.* (2013) measured the stiffness of various nanobubbles of different sizes. They found that surface nanobubbles in water behave like a Hook spring. The stiffness of the nanobubbles was between 60 and 120 pN/nm (see Fig. 23), close to the interfacial tension of a clean gas-water interface ($\sigma \approx 72$ pN/nm). Bigger nanobubbles were slightly softer than the smaller ones [see Fig. 23(b)], possibly due to the effect of the smaller Laplace pressure inside them.

Walczyk, Schön, and Schönherr (2013) confirmed that the apparent height of the nanobubbles decreases linearly with the applied force for a given tip; see Fig. 24. An extrapolation method to zero force allowed Walczyk, Schön, and Schönherr (2013) to obtain the undisturbed nanobubble (or nanodroplet) profiles. Later, Walczyk, Hain, and Schönherr (2014) confirmed also that the stiffness of nanobubbles was comparable to the surface tension of water. We note that the deposition in their work was done with a plastic syringe which may lead to contamination effects (Berkelaar *et al.*, 2014), so it is unknown whether these objects were nanobubbles or nanodroplets.

In combining the tapping mode, the lift mode, and the force volume mode, Walczyk, Hain, and Schönherr (2014) found that the strength and the magnitude for the bubble deformation are not the same across the surface of nanobubbles, but depend on the position of the tip on the bubble surface. The extent of the deformation on the bubble rim and on the bubble center is different, leading to a nonuniform underestimation of the bubble height, width, and contact angle (Walczyk and Schönherr, 2014). This seems to imply a peculiar property of nanobubbles: the effective surface tension of a nanobubble might not be uniform but decreases from the center to the rim.

Walczyk and Schönherr (2014) also reported that nanobubbles deform more severely with hydrophobic AFM tips as compared to hydrophilic tips and that the bubble deformation depends on whether the tip approaches the bubble from the top or from the side. The degree of the underestimation of the bubble size increased with increasing bubble height and radius of curvature (Walczyk, Schön, and Schönherr, 2013; Walczyk, Hain, and Schönherr, 2014). The contact angle for the nanobubbles is only slightly underestimated when the force was extrapolated to zero interaction force and remain significantly different from the macroscopic contact angle.

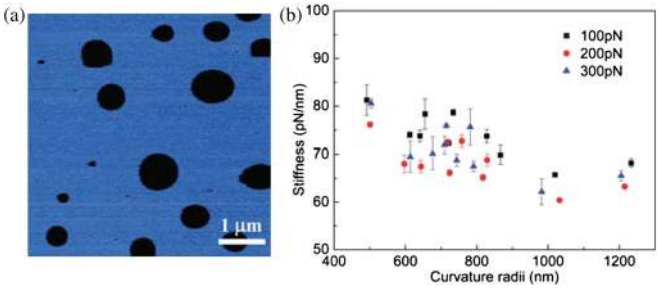

FIG. 23 (color online). Stiffness of nanobubbles measured by AFM in the mode of peak force QNM. (a) Stiffness image. The shaded area is the hard HOPG substrate, and the black circular regions are soft nanobubbles. (b) The nanobubble stiffness vs their curvature radii. The nanobubbles behave like a Hook spring. Bigger nanobubbles are always "softer" than smaller ones. From Zhao *et al.*, 2013.

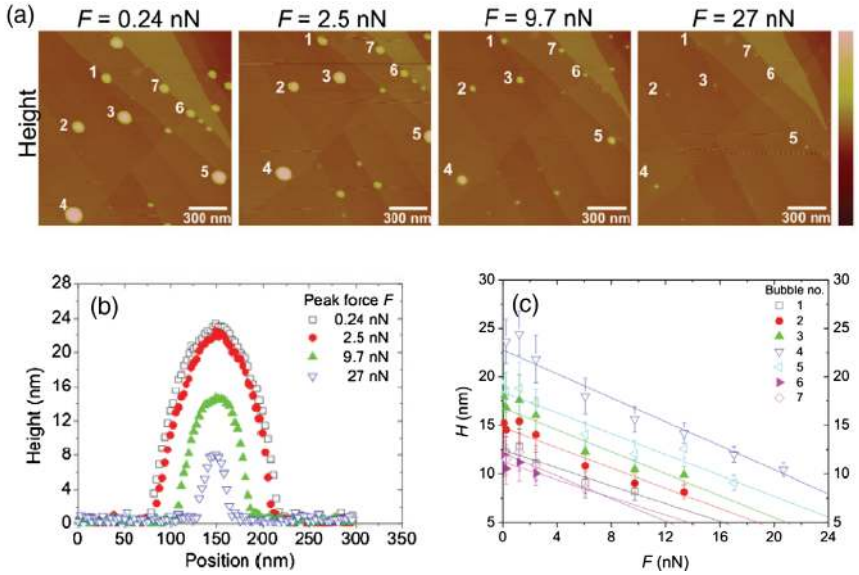

FIG. 24 (color online). (a) Peak force tapping mode AFM image of seven surface nanobubbles or nanobubblelike objects created by water droplet deposition on HOPG, taken with four different forces. (b) The nanobubble and nanodroplet profiles depend on the chosen peak force. (c) For all seven nanobubbles and nanodroplets the measured height linearly decreases with the applied peak force. An extrapolation to zero applied force gives the undisturbed nanobubble or nanodroplet profiles. From Walczyk, Schön, and Schönherr, 2013.

2. Response to ultrasound and pressure reduction

It has been known for a long time that small gas pockets in crevices on the surface can act as cavitation nuclei (Harvey *et al.*, 1944; Atchley and Prosperetti, 1989; Jones, Evans, and Galvin, 1999; Borkent, Gekle *et al.*, 2009). To investigate whether also surface nanobubbles can act as such nucleation sites for cavitating bubbles, Borkent *et al.* (2007) applied a pressure wave of −6 MPa (i.e., tension) to what they thought were surface nanobubbles on a flat hydrophobic substrate and examined the number density of the cavitation bubbles, which was compared to the number of cavitation bubbles on the surface free of nanobubbles under the same refraction wave. No correlation between the appearance of macroscopic bubbles and surface nanobubbles was found, i.e., the surface nanobubbles did not act as nucleation sites and were stable even under this extreme reduction of the liquid pressure. If this superstability of nanobubbles (as it was called) really existed [meaning that the investigated objects are not simply, as speculated by Berkelaar *et al.* (2014), nanodroplets of some contamination, which do no cavitate] this property would be extremely puzzling, as for such large pressure reduction air pockets down to a few nanometers can nucleate bubbles. Indeed, Borkent, Gekle *et al.* (2009) showed that air-filled cylindrical nanopits with a radius even down to 50 nm (smaller than the lateral extension of most nanobubbles) can nucleate bubbles, in good agreement with the theoretical prediction.

Brotchie and Zhang (2011) exposed nanobubbles on HOPG to ultrasound with a much smaller pressure amplitude, but for a longer period of time, in order to study rectified diffusion (Eller and Flynn, 1965; Leighton, 1994; Brennen, 1995; Brenner, Hilgenfeldt, and Lohse, 2002): Oscillating bubbles grow in mass once the ambient pressure is low, as then the pressure inside the bubble is low. Vice versa, for larger ambient pressure they lose gas, as then the gas inside the bubble is compressed. However, for large enough acoustic driving (even for partially degassed water) the growth process dominates as then the bubble surface is larger and the gas concentration boundary layer around the bubble is smaller. Brotchie and Zhang (2011) compared AFM nanobubble images before and after ultrasound exposure and revealed that the nanobubbles indeed become slightly larger through the exposure to ultrasound. Such response to ultrasound provides direct evidence that the domains seen in the AFM images are indeed a gaseous state, as such behavior is exclusive for bubbles, not for liquid nanodroplets or solid particles.

For comparison, Brotchie and Zhang (2011) also exposed nanodroplets on HOPG to ultrasound. Indeed, they did not grow, but some of the nanodroplets were mobile upon exposure to the acoustic wave, while others remained pinned on the substrate. This was attributed to the surface heterogeneity and the resulting difference in the pinning strength.

The effect of nanobubbles on heterogenous nucleation of macroscopic bubbles under ultrasound was demonstrated in the work of Belova *et al.* (2010, 2011). They patterned a soft substrate with hydrophobic and hydrophilic regions and immersed it in water with a controlled amount of dissolved gas. Then strong ultrasound was applied to the substrate. Strongly collapsing bubbles close to the surface develop a jet directed toward the surface and the jet impact can create micropits on the soft substrate (Leighton, 1994; Brennen, 1995). The number density of pits were then counted from high-resolution images of the substrate, giving a measure of the cavitation activity. The effect of the interfacial gases on the cavitation process became evident when surface nanobubbles were preformed by the solvent exchange process on the substrate. This was possible on both hydrophilic and

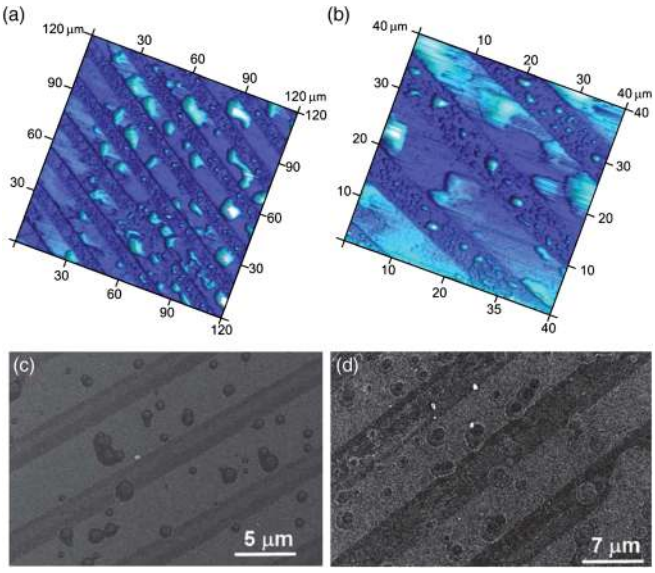

FIG. 25 (color online). (a) AFM images of the patterned substrate after the ethanol and water solvent exchange procedure. (b) An enlargement of (a). SEM images of the pits after (c) 3 min and (d) 10 min of sonication, which was performed after the formation of surface nanobubbles or micropancakes by the ethanol-water solvent exchange process. From Belova *et al.*, 2013.

hydrophobic areas as shown in Fig. 25. However, the gas volume was larger in the hydrophobic areas and after sonication more pits formed. The suggested explanation is that the cavitation processes were facilitated due to the large amount of gas in the form of nanobubbles accumulated on the interface by the solvent exchange (Belova *et al.*, 2013).

How would surface nanobubbles react to a longer-lasting change of the ambient pressure? One can expect that as the outer pressure decreases, the nanobubbles immediately expand to balance the changed ambient pressure and the Laplace pressure. On a longer time scale, the reduction of the ambient pressure leads to a decrease in the gas solubility in the liquid according to Henry's law and correspondingly to an increase in the relative gas concentration and thus a diffusive bubble growth. In fact, as stated previously, Enriquez *et al.* (2014) employed an ambient pressure reduction to quantitatively study the growth of surface microbubbles generated in hydrophobic pits, confirming the applicability of Epstein-Plesset theory and Henry's law; see Sec. VI.

Unfortunately, for surface nanobubbles direct imaging by AFM could not yet be conducted under different ambient pressures. So far only one experiment indirectly examined the response of nanboubbles to the reduction of the ambient pressure. X. H. Zhang *et al.* (2006) exposed nanobubbles to moderately reduced ambient pressure for some time and AFM imaged them before and immediately after that procedure, but again under ambient pressure of 1 atm: After 0.5 to 3 h under reduced pressure, some nanobubbles had coalesced and detached from the substrate, some others had grown, and yet others remained unchanged. Several intermediate stages of nanobubble removal were proposed: The reduced pressure results in the growth of some nanobubbles. When the size of the nanobubbles increases, they may merge with surrounding nanobubbles, which accelerates the bubble expansion. Once large enough, the bubble may detach from the substrate because of buoyancy and leave some region free of bubbles. If the recovery of the ambient pressure to atmospherical pressure of 1 atm occurs before the detachment, the expanded bubbles will shrink again and leave behind a circular adjacent rim free of nanobubbles. The results of X. H. Zhang *et al.* (2006) are additional evidence that the nanoscopic objects seen in AFM, or at least some of them, are indeed of a gaseous nature.

The study by X. H. Zhang *et al.* (2006) also revealed an important feature of surface nanobubbles: *individuality*, similar to the feature of surface nanodroplets. Not all nanobubbles (even of the same size) respond to the pressure reduction in the same way. Some dissolve while others remain. As they dissolve, the dissolution rate differs from bubble to bubble. The answer we have to this puzzling observation is that the surface must be chemically and/or geometrically heterogeneous, presumably due to absorption of species on the hydrophobic surface, either airborne prior to immersion in water or waterborne after immersion. Note that even small concentrations of hydrophobic organic contaminations of the water (say, only thousands of molecules in a drop of water) are enough to form hydrophobic patches on the surface. Another origin of the individuality can be differences in the local gas saturation, due to neighboring bubbles.

3. Response to temperature rise

The stability of surface nanobubbles at different temperatures was investigated both experimentally and theoretically; see, e.g., Zhang, Li *et al.* (2005), Thormann *et al.* (2008), Berkelaar *et al.* (2012), Guan *et al.* (2012), and Petsev, Shell, and Leal (2013). S. Yang *et al.* (2007) increased the water temperature in intervals of 5 °C from 20 to 40 °C and found a dramatic increase of the nanobubble density from 30 to 35 °C. The nanobubbles did not disappear when the water cooled down to ambient conditions, at least not on the time scale of the experiment. Some of the above experimental studies have shown that also the typical nanobubble size is temperature dependent, with the maximal typical bubble size occurring around 35–40 °C. Berkelaar *et al.* (2012) related this finding to the minimal air solubility in water around this temperature, leading to the largest saturation level at those temperatures. Also they found individuality of the surface nanobubbles: At a certain temperature change, some nanobubbles grew while others with the same size shrink. Again, we interpret this as a consequence of (chemical) surface inhomogeneities. Finally, Berkelaar *et al.* (2012) found that also the total nanobubble volume per unit area had a maximum around 33 °C, which is similar to what had been found in earlier studies by Zhang, Li *et al.* (2005).

Zhang *et al.* (2014) investigated large surface (nano) bubbles (generated by solvent exchange) on a highly hydrophobic surface that are more than 2.5 μm in lateral extension and several hundred nanometers in height. Thus optical microscopy imaging could be used to follow those bubbles at an elevated temperature. They found that these nanobubbles survive a temperature rise even up to the boiling point of

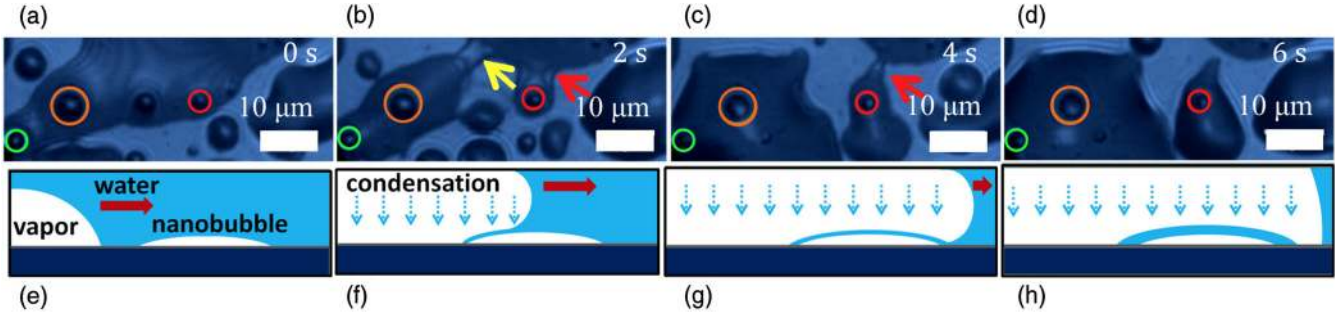

FIG. 26 (color online). Top view snapshots of nanobubbles in water at 95 °C. Individual nanobubbles are identified by different colors, and the arrows point to the liquid bridges which eventually break. The corresponding times are (a) 0 s, (b) 2 s, (c) 4 s, and (d) 6 s. (e)–(h) Schematic drawings of microdroplet nucleation triggered by a nanobubble and the subsequent growth of the microdroplet by condensation. From Zhang *et al.*, 2014.

water. Even during the boiling process, nanobubbles are remarkably stable, although a simple nucleation theory suggests that then they already should be unstable (Zhang *et al.*, 2014). We think that this enhanced stability can be provided only by the strong pinning to the substrate.

The events during boiling are depicted in Fig. 26. As normal vapor microbubbles already form and expand at temperatures close to boiling, the TPCL of such expanding vapor bubbles moves across the surface and can hit the surface (nano)bubbles. Remarkably, the nanobubbles then pin the TPCL of the moving microbubble. The TPCL of the microbubble then moves on and once it snaps off from the nanobubble, a microdroplet inside the microbubble nucleates on the nanobubbles. The microdroplet then grows by nucleation and keeps the nanobubbles stable on the surface even after the bulk liquid has retreated. Once all water has evaporated in the system and the condensation has ceased, the nanobubbles finally burst, again showing their gaseous nature.

E. Collective effects and nanobubble interactions

The spatial distribution of surface nanobubbles is related to their formation methods. By directly immersing a substrate into water, two distinctive distributions of nanobubbles were observed: The densely packed irregular nanobubble networks in Fig. 4(c) as observed by Tyrrell and Attard (2001, 2002), and the sparsely distributed nanobubbles in Fig. 4(a), as observed by Ishida *et al.* (2000) and Yang *et al.* (2003). Borkent, Schönherr *et al.* (2009) analyzed the statistical distributions of discrete surface nanobubbles that were created either by droplet deposition or by the solvent exchange method. In the first case the bubble size distribution had a single peak with a preferred radius of 20 nm and the preferred bubble spacing was about 5 times larger. The radial distribution function was quite different from that of randomly packed hard disks, suggesting a structuring effect in the nanobubble formation process. In the second case the bubble size distribution was double peaked. Note that later Berkelaar *et al.* (2014) argued that the analyzed object in Borkent, Schönherr *et al.* (2009) may in fact at least partly be (PDMS) nanodroplets rather than nanobubbles, in particular, for the droplet depositions case. In any case, we think that chemical surface inhomogeneities play a major role in the spatial distribution of both nanobubbles and nanodroplets.

Lhuissier, Lohse, and Zhang (2014) analyzed the spatial distribution of nanobubbles produced by solvent exchange, employing a Voronoi analysis of AFM images of surface nanobubble populations [see Fig. 27(a)]. That analysis showed that the distribution of the nanobubbles is not random as in a random Poisson process, which cannot be explained by bubble nucleation on random heterogeneities on the surface. They concluded that the growth of the bubbles already nucleated competes with the formation of new bubbles. The Voronoi analysis also showed a correlation between the individual bubble size and the depleted area around the bubbles [the area of the so-called modified Voronoi cell, see Fig. 27(b)]. Larger bubbles had larger depleted areas than smaller ones. The actual functional dependence between the modified Voronoi area and the bubble footprint size could theoretically be understood from a model assuming that nanobubbles grow by diffusion of

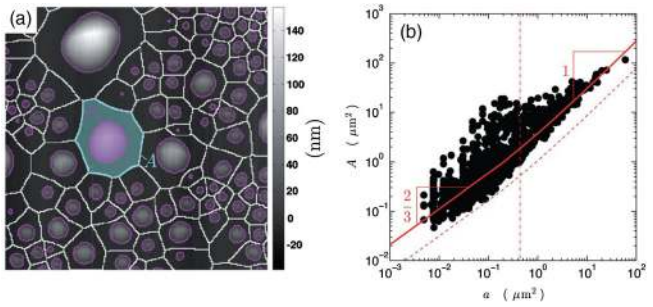

FIG. 27 (color online). Spatial arrangement of surface nanobubbles. (a) Modified Voronoi tessellation of surface nanobubbles with one representative modified Voronoi cell. The three-phase boundary of nanobubbles is marked by lines. A is the area of the modified Voronoi cell, i.e., the set of all points with minimal distance to the edge of the surface nanobubble in the center of the modified Voronoi cell. (b) The cell area A of the modified Voronoi cells vs the area a of the nanobubble footprints. The vertical dash-dotted line shows the transition between small and large bubbles, where for the former ones the internal pressure is dominated by the Laplace pressure and for the latter ones by the ambient pressure; cf. Eq. (12) and Sec. VI. The shown slopes $2/3$ and 1 for the dependence $A(a)$ result from these two limiting cases whereas the dashed line shows the full theoretical dependence $A(a)$ derived by Lhuissier, Lohse, and Zhang (2014) and the solid line the same dependence, but shifted by a prefactor adopted to the experimental data. From Lhuissier, Lohse, and Zhang, 2014.

the gas from the bulk rather than by diffusion of the gas adsorbed on the surface or from an instability of a potential gas condensate (micropancake) at the surface.

But also after their nucleation there must be cross talk between the surface nanobubbles through diffusion. For bubbles (and droplets) in the bulk such cross talk leads to shrinkage of neighboring smaller bubbles and growth of larger ones (the so-called Ostwald ripening), due to the concentration gradient caused by the different Laplace pressures [cf. Eq. (12) and Henry's law Eq. (9)]. In principle, such Ostwald ripening should also occur for surface nanobubbles. The gas transport again must go from the bubble with smaller radius of curvature to the one with larger radius of curvature, but given that for surface nanobubbles there can be contact line pinning (stabilizing the bubbles), this does not necessarily mean that it goes from smaller to larger bubbles. Instead, the diffusive flux will go from bubbles with larger curvature to those with smaller curvature, which volumewise need not be larger than the shrinking bubbles.

Reports of experimental observations of Ostwald ripening of surface nanobubbles are unfortunately rare. This, in particular, holds for surface nanobubbles consisting of air, for which due to the low air solubility in water the dynamics is particularly slow, as we see in Sec. VI.A. For CO_2 bubbles the dynamics is about 50 times faster (see Table II) than for air bubbles and indeed Yang *et al.* (2003) observed the slow dissolution of small CO_2 surface nanobubbles next to larger ones. A similar observation, also for CO_2 surface nanobubbles, was made by German *et al.* (2014), but due to resolution issues none saw the growth of larger surface nanobubbles next to smaller ones.

One example for Ostwald ripening of nanobubbles in a highly confined space may be the one by Shin *et al.* (2015), who followed the nanobubble dynamics in water encapsulated between a graphene membrane by *in situ* ultrahigh vacuum transmission electron microscopy (UHV-TEM) (see Fig. 16). In case the bubble sizes were distinctively different, the smaller bubbles (typically below 3 nm in footprint diameter) tended to disappear near growing larger bubbles (typically 10 nm footprint radius), thus showing diffusive gas exchange (see Fig. 16). In contrast, for two similar-sized nanobubbles, a coalescing process occurred where the interface of the bubbles broke and the merged bubble finally reshaped into a spherical morphology. Note that these nanobubbles in this highly confined environment did not seem to show contact line pinning, as their contact angle was constant, $\theta \approx 71° \pm 1°$, regardless of their size (2–10 nm) and their age, as revealed from side views (see Fig. 15 for an example). We note that the Laplace pressure in these small nanobubbles in the confined and encapsulated environment must be enormous and was estimated to be 27 MPa, i.e., 270 times the ambient pressure (Shin *et al.*, 2015).

V. MOLECULAR DYNAMICS SIMULATIONS

A. Methods and limitations

MD-type simulations have developed tremendously over the last decades and are presently more and more used in fluid dynamics. For reviews see Koplik and Banavar (1995), Frenkel and Smit (1996), Lauga, Brenner, and Stone (2007), and Bocquet and Charlaix (2010). The idea is that for a given potential between individual molecules and given boundary conditions, the whole overall dynamics should result from integrating the force equations. Thanks to the increasing computational resources and improved code parallelization—these days in principle multitrillions of particles with an overall performance of hundreds of teraflops (on $\sim 10^5$ cores) can be simulated (Eckhardt *et al.*, 2013)—we presently witness the fact that the gap between MD simulations and continuum-type descriptions based on the Navier-Stokes equation, the advection-diffusion equation, and the Laplace equation is closing. For a general review see Bocquet and Charlaix (2010). More specific examples include, e.g., the calculation of the shape and contact angle of a nanodroplet in air on smooth (Weijs *et al.*, 2011) and patterned (Daub *et al.*, 2010; Ritchie *et al.*, 2012) surfaces, the calculation of a nanodrop impact on a surface by Koplik and Zhang (2013), and the calculation of the droplet emission from an abruptly molten metal surface by Afkhami and Kondic (2013). Bocquet and Charlaix (2010) give as an estimate 1 nm as a length scale above which continuum descriptions can become reasonable. To extend continuum concepts to such small scales, at interfaces the so-called disjoining pressure Π_d was introduced [see, e.g., de Gennes, Brochard-Wyart, and Quere (2004) or Bonn *et al.* (2009) and Sec. VI.D.4], representing interfacial effects on the bulk liquid. In any case, an overlap between continuum approaches and MD simulations is developing.

In this context we also mention the power of lattice-Boltzmann (LB)-type methods (Chen and Doolen, 1998) which can be considered to be kind of in between continuum dynamics simulations and MD simulations. We think that they have great potential to study dissolving surface nanobubbles and nanodroplets and, in particular, the collective effects thereof, which may presently be too challenging for MD. To our knowledge a LB method has not yet been employed to study the diffusive dynamics of nanobubbles. However, in a pioneering paper Ledesma-Aguilar, Vella, and Yeomans (2014) employed a LB method to analyze the evaporation of a surface microdroplet in air.

Given their size and the meanwhile available computational power, surface nanobubbles in principle should be accessible to MD simulations. However, there are several severe complications: (i) First, the above examples for a good comparison between MD simulations and continuum descriptions are all for nanodroplets, rather than for nanobubbles. The reason is that then a denser integrity (the droplet) is surrounded by a less dense one (air or in general gas), allowing for an overall smaller number of particles than the other way around. (ii) Second, the larger the number of particles, the smaller the number of time steps that can be simulated. Achieving microseconds is already extremely challenging, given that the typical time step for the integration is of the order of a few femtoseconds as the characteristic time of atomic motion is subpicoseconds. In contrast, as described previously, the dynamics of nanobubbles can be on a time scale order of days, implying that $\sim 10^{20}$ time steps would be required, which clearly is not feasible. (iii) Third, and even more seriously, the intermolecular potentials are incompletely known. Open source MD packages like GROMACS, which emerged out of the seminal work by Berendsen *et al.* (1984) in

Groningen, or LAMMPS, which is based in the Sandia National Laboratory, typically have hundreds of different potentials for nontrivial molecules such as water, and none of them correctly reflects all macroscopic material properties of even the pure bulk liquid such as viscosity, boiling and freezing points, surface tension, dielectric constant, etc., not to mention interfacial forces between different species.

Therefore, and as it is up to 1 order of magnitude cheaper in computational time, one often restricts oneself to Lennard-Jones (LJ) potentials, which per pair of molecules only contain two parameters, namely, the depth ϵ and the interaction length scale σ. In fact, for the interaction between argon or other inert gases among each other the LJ potentials agree rather nicely with more elaborate potentials, but not for water. That brings us to yet another complication, namely, (iv) the range of the interaction potential: Electromagnetic interactions are very long range, making the problem nonlocal in space and thus computationally expensive. Clearly, long-range cutoffs have to be introduced to keep the simulations feasible. We note that this may affect the disjoining pressure (de Gennes, Brochard-Wyart, and Quere, 2004; Bonn *et al.*, 2009) which is a continuum parametrization of the long-range effects of the individual potentials of the individual solid molecules or atoms on the gas or liquid in touch with the solid.

Given all these severe complications, in practice in most MD simulations of surface nanobubbles only LJ potentials with some long-range cutoff have been used, with only hundreds of thousands of particles (solid, liquid, gas), corresponding to a length scale of at most tens of nanometers, for at most submicroseconds integration time. Such simulations can give only an indication on what is going on.

B. Liquid depletion zones at hydrophobic interfaces

As elaborated in Sec. III.D, there are various experimental indications of a liquid depletion zone close to hydrophobic surfaces, and there is the theoretical expectation (Lum, Chandler, and Weeks, 1999) that long-range (exclusively) repulsive forces will indeed allow for the nucleation of such a depletion zone. The experimental studies and theoretical considerations have been augmented by MD simulations.

Among the first simulations of that kind were the studies by Leung, Luzar, and Bratko (2003) and Luzar and Bratko (2005), showing that for realistic molecular parameters there is indeed major accumulation of gas at hydrophobic surfaces, with 25- to 50-fold increase in the local gas concentration, but that the adsorption is restricted to the first monolayer of liquid, and that the effect of the dissolved gas on the width of the depletion zone is small, at least for gas-saturated water, in contrast to the neutron reflectivity measurements of Doshi *et al.* (2005), but in agreement with x-ray studies by Mezger *et al.* (2006). Later, Bratko and Luzar (2008) extended those MD simulations with realistic potential to strongly gas-oversaturated liquids, finding qualitatively the same result.

Nonetheless, the gas accumulation on hydrophobic surfaces has repeatedly been used to account for the experimentally observed large slip length, which shows a systematic bias toward higher values than theoretical ones; see, e.g., the review articles by Neto *et al.* (2005) and Bocquet and Charlaix (2010).

Some wall slip can be achieved through the accumulation of gas molecules at the wall, as shown in the MD study of Dammer and Lohse (2006), although the used LJ parameters of that study do not necessarily represent realistic gases and liquids. For hydrophobic surfaces Dammer and Lohse (2006) found gas accumulation that was by more than 2 orders of magnitude larger as compared to the bulk gas density, here leading to a modified structure of the water close to the wall, but only to a slightly enhanced wall slip of a few molecular diameters. This by far is not enough to account for the experimental observations of a much larger slip (Neto *et al.*, 2005; Bocquet and Charlaix, 2010). These numerical findings thus fed the speculation (de Gennes, 2002; Neto *et al.*, 2005; Bocquet and Charlaix, 2010) that the reason for the enhanced slip may be the formation of surface nanobubbles, which were absent in the MD simulations of Dammer and Lohse (2006).

More realistic LJ parameters mimicking various gases and liquids were used in the MD simulations of Sendner *et al.* (2009). Depending on the gas type, for hydrophobic surfaces slip lengths of several nanometers were obtained (strongly correlated with the width of the depletion zone at the surface), but again with only slightly larger values for liquids with dissolved gases, in spite of strong gas absorption at the surface. Sendner *et al.* (2009) also provided scaling arguments for the mutual dependences of the slip length, the width of the depletion zone, and the contact angle.

C. MD surface nanobubbles

While a number performed MD simulations on the nucleation and properties of nanobubbles in the bulk, there are only a few MD studies of surface nanobubbles. To our knowledge the first one was by Weijs, Snoeijer, and Lohse (2012), who simulated a ternary (solid, liquid, gas) system with LJ potentials in between the different species,

$$U(r) = r\epsilon_{ij}\left[\left(\frac{\sigma_{ij}}{r}\right)^{12} - \left(\frac{\sigma_{ij}}{r}\right)^{6}\right], \tag{6}$$

which was truncated after typically $5\sigma_{ij}$. The parameters of the MD simulation are the interaction strength ϵ_{ij} and range σ_{ij} between the species $\{i, j\} \in \{l, s, g\}$ for liquid, solid, and gas. The GROMACS package was used, with constant temperature, volume, and particle number, all in a Berendsen thermostat (Bussi, Donadio, and Parrinello, 2007). The solid particles were constrained to their initial position throughout time and constitute the immobile substrate where the gas and liquid particles can freely float around. Their properties as solid, liquid, or gas are defined by their respective interaction parameters and the temperature. The simulated box size was typically $40 \times 40 \times 5.5$ nm^3, with periodic boundary conditions in all directions. Typically, Weijs, Snoeijer, and Lohse (2012) used 13 000 solid particles, 62 000 liquid particles, and 1600 gas particles. The simulations were done on typically about 100 parallel CPUs and 3 h simulation time corresponded to 1 ns real time. The initial conditions were characterized by massive local gas oversaturation. For appropriate interaction parameters—low $\epsilon_{lg}/\epsilon_{ll}$ and large σ_{lg}/σ_{ll} both of which imply low gas solubility in the liquid—this

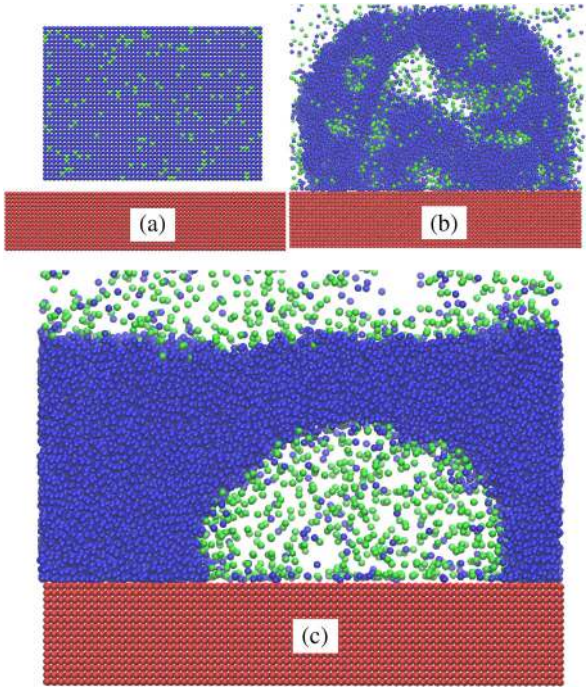

FIG. 28 (color online). Surface nanobubble formation in the Lennard-Jones MD simulations of Weijs, Snoeijer, and Lohse (2012). For the detailed parameters see that paper. Different colored molecules represent the (fixed) surface, the liquid, and the gas. Three snapshots are shown, namely, (a) the initial conditions with a gas oversaturation, (b) the initial phase of bubble nucleation at 0.1 ns, and (c) the fully formed surface nanobubble at 10 ns. As seen from Fig. 29, with ongoing time this nanobubble dissolves again.

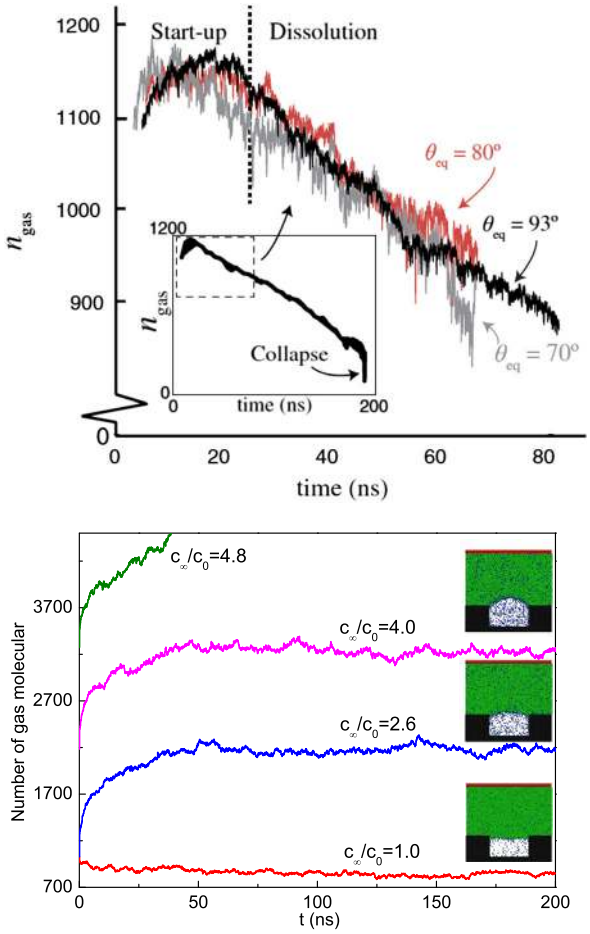

FIG. 29 (color online). (Upper) Shrinking nanobubbles in the MD simulations of Weijs, Snoeijer, and Lohse (2012) for various equilibrium contact angles. n_{gas} is the number of gas molecules inside the nanobubble. The inset shows the full dissolution of the $\theta_{eq} = 92°$ bubble after 0.2 μs. Note that the depth of the pool in which the bubble is immersed is comparable to the lateral bubble extension; see Fig. 28. (Lower) Number of gas molecules in a pinned nanobubble (shown in the figure) for three different relative gas concentrations c_∞/c_0, corresponding to saturation or oversaturation. Adapted from Liu and Zhang, 2014.

would lead to the nucleation of nanobubbles typically 20–30 nm wide, 10–20 nm high, and consisting of 1000 gas particles (the other gas particles are dissolved in the liquid), in a pool of depth 20–30 nm, as seen in Fig. 28, in which three snapshots of the dynamical evolution are shown. As there were no pinning forces for the nanobubble, it freely floated around over the surface. For strong attraction of the gas molecules toward the wall $\epsilon_{sg}/\epsilon_{ll} > 1$, a one-molecule wide gas layer would form in between the liquid and the solid on which the surface nanobubble would float. In this limit the contact angle (on the gas side) would become universal and relatively flat [typically 75°—still much larger than observed in experiment, but consistent with what one would expect from a mean field argument (Bauer and Dietrich, 1999; Snoeijer and Andreotti, 2008)].

However, the MD surface nanobubbles were not stable and for all analyzed cases of Weijs, Snoeijer, and Lohse (2012) dissolved within microseconds, as seen from Fig. 29. As there was no pinning, the contact angle remained roughly constant during the dissolution process. The shrinkage occurred via a delicate balance between the total gas influx into the bubble and the total gas outflux, which was slightly larger. Note that both influx and outflux showed an angular dependence, with the latter being maximal close to the three-phase contact line, in contrast to the speculation of Brenner and Lohse (2008).

As compared to experiment, the MD simulations of Weijs, Snoeijer, and Lohse (2012) missed crucial ingredients leading to their long lifetime. This could be (i) the lack of conditions that are sufficiently far from equilibrium, i.e., some possible external driving, (ii) a sufficiently large pool depth ℓ which was only tens of nanometers in contrast to typically millimeters as in experiment, (iii) contact line pinning by chemical or geometrical surface inhomogeneities, (iv) more intricate and long-range intermolecular potentials, and (v) contamination, among others. We conclude that one or more of these missing conditions must be the origin of the found nanobubble stability in experiment and we discuss them in Sec. VI.

We stress that stable MD nanobubbles can be found in closed, gas-oversatured finite-sized systems. Weijs, Seddon, and Lohse (2012) simulated such a system with periodic boundary conditions in all directions and found that for sufficient gas oversaturation nanobubbles nucleate in the bulk. This is not surprising as, from some gas concentration on, it is

energetically more expensive to squeeze further gas molecules in between the liquid molecules, rather than forming nanobubbles. Occurrence, growth rate, equilibrium size, and critical size corresponded exactly to what one would expect from the macroscopic description such as Henry's law, Laplace's law, and the diffusion equation. This would also hold in systems with one or more solid walls, provided that they are closed. If these walls were hydrophobic, then bubble nucleation would occur at these walls, implying stable surface nanobubbles in these fully closed systems. Note, however, that in experiment the systems are open or at least partially open.

Recently, Liu and Zhang (2014) extended the MD simulation of Weijs, Snoeijer, and Lohse (2012), but explicitly included controlled surface heterogeneities into their substrate. They unambiguously showed that these can lead to contact line pinning of the surface nanobubbles, which together with the gas oversaturation turned out to be crucial for surface nanobubble stabilization. Examples for pinned stable nanobubbles in an oversaturared solution, obtained by MD, are shown in Fig. 29, lower panel.

D. Density functional theory approaches

Next to MD simulations, constrained and kinetic lattice density functional theory (LDFT) have been tried to account for surface nanobubble formation and stability (Liu and Zhang, 2013b). In that numerical work thermodynamically metastable surface nanobubbles were found, provided that there was some gas oversaturation of the liquid and sufficient surface heterogeneity (either geometrically or chemically). This heterogeneity is a crucial ingredient to provide contact line pinning which stabilizes the bubbles in the metastable state (see Fig. 30), which resulted from kinetic LDFT calculations and shows the time evolution of the nanobubble volume and the contact angle for an unpinned and a pinned (by roughness) situation: While in the former case the bubble dissolved with roughly constant contact angle, in the latter case both the volume and the contact angle remained constant. The reason is that, once there is pinning of the contact line, the shrinkage of the bubble leads to a larger radius of curvature and thus to a reduction of the Laplace pressure and thus stabilization, in contrast to the situation for a free bubble or an unpinned bubble, for which shrinkage implies a Laplace pressure enhancement and thus destabilization; see Sec. VI. Liu and Zhang (2013b) also demonstrated that for geometric inhomogeneity the microscopic contact angle (on the gas side) is always much smaller than the macroscopic one and only weakly depends on the substrate chemistry, as also found in experiments; see, e.g., Zhang, Maeda, and Craig (2006), where they provided a prediction based on a thermodynamical argument that stable surface nanobubbles can exist only in a certain size range.

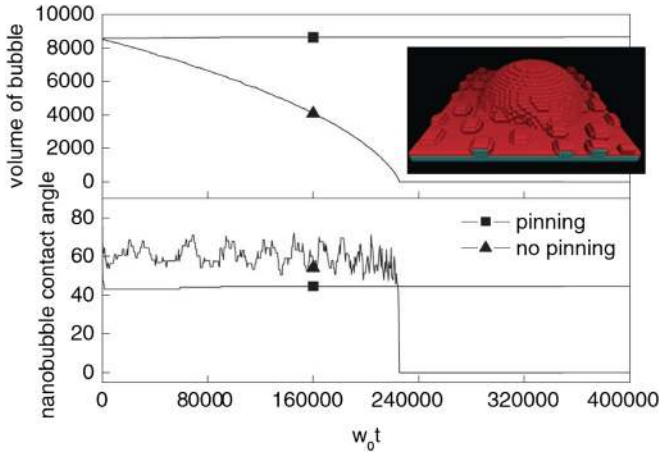

FIG. 30 (color online). Results from the kinetic LDFT calculations: Volume of a nanobubble and its contact angle as a function of time: Pinning caused by surface roughness provides the nanobubble stability. Length and time scales are given in the computational units of Liu and Zhang (2013b). The inset shows a pinned nanobubble on some geometrically inhomogeneous surface structure, obtained by constrained LDFT calculations. From Liu and Zhang, 2013b.

VI. THEORIES FOR SURFACE NANOBUBBLES AND NANODROPLETS

In this section we show that the stability and small contact angle of surface nanobubbles can be understood from the diffusion equation, the Laplace equation, and Henry's law (Sec. VI.D). The central ingredient will be the *pinning* assumption which is motivated in Sec. VI.E. In Sec. VI.F we elaborate on other dissolution (or growth) modes of surface nanobubbles and nanodroplets. But before doing so, we revisit the classic Epstein-Plesset theory (Sec. VI.A) for dissolving or growing spherical bulk bubbles (or droplets) and explain why a contamination theory (Sec. VI.B) and a dynamic equilibrium theory (Sec. VI.C) are insufficient to account for stable surface nanobubbles.

A. Epstein-Plesset theory for bulk bubbles

In a classical paper, Epstein and Plesset (1950) calculated the lifetime of a spherical isolated bubble of initial radius R_0 and at rest in an infinitely extended liquid-gas solution in which the gas concentration far away from the bubble is c_∞, whereas the gas solubility is c_s. Although Epstein and Plesset (1950) had the growth (shrinkage) of macroscopic bubbles in oversaturated (undersatured) gas solutions in mind, their calculation is also applicable for microscopic and nanoscopic bubbles, as the effect of surface tension is explicitly taken into consideration and as the employed hydrodynamical equations hold down to the nanoscale (Bocquet and Charlaix, 2010). Ljunggren and Eriksson (1997) adopted the Epstein-Plesset calculation in the context of surface nanobubbles, although they still assumed a spherical isolated bubble far from any walls. So strictly speaking their calculation is not applicable to surface nanobubbles, but their paper (Ljunggren and Eriksson, 1997)—with the spherical bubble radius being replaced by the radius of curvature—had always been used as an illustration that the measured lifetime of surface nanobubbles is much longer than the theory would predict, at least order of magnitude wise.

1. Diffusion equation, Laplace equation, and Henry's law

In general, the diffusion equation for the mass concentration $c(\mathbf{r}, t)$ (mass and volume) reads

$$\partial_t c + \mathbf{u}\cdot\nabla c = D\nabla^2 c, \tag{7}$$

where D is the gas diffusion coefficient in the liquid and $\mathbf{u}$ is the velocity field. Under the above formulated assumptions by Epstein and Plesset (1950) for a spherical bubble of radius $R(t)$, the diffusion equation for the mass concentration $c(r,t)$ around the spherical bubble becomes

$$\partial_t c + \dot{R}\frac{R^2}{r^2}\partial_r c = D\frac{1}{r^2}\partial_r(r^2\partial_r c), \tag{8}$$

where $R(t)$ is the time-dependent bubble radius. The inner boundary conditions for the spherical concentration field at the bubble's interface are given by Henry's law

$$c(R,t) = \frac{c_s}{P_o}p_g(t), \tag{9}$$

as the gas in the bubble is assumed to remain in equilibrium with that in the liquid at the boundary of the bubble wall. Here $p_g(t)$ is the pressure inside the bubble and the ratio $k = c_s/P_0$ between the gas solubility c_s and the ambient pressure P_0 in the outside world is called Henry's constant.[1] Finally, the gas concentration far from the bubble is given by the ambient concentration c_∞,

$$c(\infty,t) = c_\infty. \tag{10}$$

The gas concentration can also be expressed in terms of the gas oversaturation

$$\zeta \equiv \frac{c_\infty}{c_s} - 1. \tag{11}$$

The pressure $p_g(t)$ inside the gas bubble is given as a sum of the ambient pressure P_0 and the Laplace pressure (neglecting the vapor pressure)

$$p_g(t) = P_0 + \frac{2\sigma}{R(t)}. \tag{12}$$

On the other hand, it also obeys the ideal gas law

$$\frac{4\pi}{3}R^3(t)p_g(t) = n(t)\mathcal{R}T, \tag{13}$$

where $n(t)$ is the number of moles, $\mathcal{R}\approx 8.3145$ J/mol K is the ideal gas constant, and T is the (constant) temperature. Depending on whether the first or second term in Eq. (12) dominates, we speak of large or small bubbles, respectively. For large bubbles $R \gg 2\sigma/P_0$ ($\approx$1.4 μm for air in water at ambient pressure) the gas pressure p_g inside the bubble is dominated by the ambient pressure, whereas for small bubbles $R \ll 2\sigma/P_0$ it is dominated by the Laplace pressure.

The mass loss or gain of the bubble is proportional to the gas concentration gradient at the bubble wall,

$$\dot{m} = 4\pi R^2 D\partial_r c|_{R(t)}. \tag{14}$$

[1]Some call k^{-1} Henry's constant.

For purely diffusive (quasistatic) growth or shrinkage, Epstein and Plesset (1950) succeeded to analytically calculate the full spatial and temporal dependence $c(r,t)$ of the gas concentration field and, in particular, from Eq. (14) the radial growth and shrinkage rate

$$\dot{R} = \alpha\left(\frac{1}{R} + \frac{1}{\sqrt{\pi D t}}\right) \tag{15}$$

with

$$\alpha \equiv \frac{D}{\rho_g}\frac{c_\infty - c_s(1+2\sigma/RP_0)}{1+4\sigma/3RP_0}, \tag{16}$$

where ρ_g is the density of the gas.

We now discuss this expression in the two limiting cases of large and small bubbles. For large bubbles $R(t) \gg 2\sigma/P_0$ it can be approximated as

$$\alpha \approx \frac{D(c_\infty - c_s)}{\rho_g} = \frac{Dc_s}{\rho_g}\zeta. \tag{17}$$

For oversaturation $c_\infty > c_s$ or $\zeta > 0$ the bubble grows and for undersaturation $c_\infty < c_s$ or $\zeta < 0$ it shrinks.

For small bubbles $R(t) \ll 2\sigma/P_0$ and at the same time $R(t) \ll 2\sigma/(P_0 c_\infty/c_s)$ (for oversaturation $c_\infty/c_s > 1$, the latter is the more restrictive condition) in the last phase of dissolution we have

$$\alpha \approx -3Dc_s/(2\rho_g), \tag{18}$$

independent of the undersaturation $\zeta < 0$, as then the process is purely driven by Laplace pressure, which accelerates dissolution. It is remarkable that although the Laplace pressure drives the process, the value of the surface tension itself cancels out in this limiting case. However, in the transition regime the value of the surface tension shows up explicitly; see Eq. (16).

By integrating Eq. (15) the shrinkage or growth dynamics of the bubble can be directly calculated.

2. Shrinking bubbles

We start with the shrinking case ($c_\infty < c_s$, resulting in $\alpha < 0$ and $\zeta < 0$). Neglecting transient effects during which the second term on the right-hand side of Eq. (15) still plays a role, that equation can be integrated to obtain

$$R(t) \approx \sqrt{R_0^2 - 2|\alpha|t}, \tag{19}$$

i.e., an approximate bubble lifetime of

$$\tau_{\text{life}} \approx \frac{R_0^2}{2|\alpha|} \approx \begin{cases} \frac{R_0^2\rho_g}{2Dc_s|\zeta|} & \text{for large } R_0, \\ \frac{R_0^2\rho_g}{3Dc_s} & \text{for small } R_0, \end{cases} \tag{20}$$

for a spherical bubble of initial radius R_0. Epstein and Plesset (1950) also gave the exact lifetimes and showed that they are not very different from the approximate ones.

Note that the time scale of the diffusive process is not given by the diffusive time R^2/D, but by Eq. (20), which has an extra factor ρ_g/c_s. Thus the time scale $\tau_{\rm life}$ gets large for gases with small solubility c_s such as nitrogen or oxygen, whereas for CO_2 the diffusive dynamics is about 50 times faster; see Table II. The large-R expression diverges to an infinite lifetime for $\zeta \to 0$ in the employed approximation that neglects surface tension effects, but the full expression (16) leads to a finite bubble lifetime also for the saturated case $c_s = c_\infty$ (i.e., $\zeta = 0$), due to the effect of nonzero surface tension.

It is useful to give some numerical values for the above calculated dissolution times. Diffusion constants D, solubilities c_s, gas densities ρ_g, and the resulting (approximate) lifetimes for a $R = 1$ μm (i.e., small) bubble and a $R = 10$ μm (i.e., large) bubble consisting of various gases are given in Table II. As one can see, for the gases with high solubilities such as CO_2 and SO_2, the lifetime dramatically decreases. More values for the dissolution times for various bubble sizes and undersaturations $\zeta < 0$ are given in Epstein and Plesset (1950) and Ljunggren and Eriksson (1997).

What directly follows from Eq. (20) is that small bubbles [with $R_0 \ll \sigma/P_0$ and at the same time $R_0 \ll 2\sigma/(P_0 c_\infty/c_s)$] cannot stably exist in the bulk, even not for oversaturation $c_\infty > c_s$: The surface tension squeezes them out and they dissolve in time $\tau_{\rm life} \approx R_0^2 \rho_g/3Dc_s$. Therefore, according to Epstein and Plesset (1950) there are no stable bulk nanobubbles.

We stress that the Epstein-Plesset theory also quantitatively describes the shrinkage (or growth) of droplets in liquids as, e.g., shown by Duncan and Needham (2006) and Su and Needham (2013)—then the boundary condition for the concentration field at the droplet interface is simply the saturation concentration c_s [neglecting the effect of the surface tension on the solubility of the droplet liquid in the surrounding liquid which is justified for not too large saturation levels (Duncan and Needham, 2006)]. Again, the solubility is crucially determining the time scale and thus the lifetime of the droplet. Just as for gas bubbles, the dynamics is much faster for high solubilities. Typical examples for the solubilities and diffusion constants of some liquids immiscible with water and the resulting lifetimes of the droplets are included in Table II.

TABLE II. Material properties of various gases (upper part) and liquids (lower part; then ρ_g means the density of the liquid drop) in water at 25 °C under ambient pressure conditions (Battino, Seybold, and Campanell, 2011) and the resulting lifetimes for spherical bubble (droplet) dissolution. HDODA stands for 1,6-hexanedioldiacrylate and MMA for methylmethacrylate. The lifetime $\tau_{\rm life}^{R_0=1\ \mu\rm m}$ (given in milliseconds) for a 1 μm bubble (droplet) was calculated from Eq. (20) in the small-bubble limit (i.e., smaller at 1.44 μm), in which the dissolution time is independent of the undersaturation ζ. The lifetime $\tau_{\rm life}^{R_0=10\ \mu\rm m}$ (given in seconds) for a 10 μm bubble was calculated from Eq. (20) in the large-bubble limit for an undersaturation of $\zeta = -0.1$, i.e., $c_\infty/c_s = 90\%$.

Gas	c_s (kg/m^3)	ρ_g (kg/m^3)	D (10^{-9} m^2/s)	$\tau_{\rm life}^{R_0=1\ \mu\rm m}$ (ms)	$\tau_{\rm life}^{R_0=10\ \mu\rm m}$ (s)
He	0.0015	0.163	6.3	5.7	8.6
H_2	0.0016	0.082	2.7	6.3	9.5
N_2	0.018	1.146	2	11	17
CH_4	0.022	0.656	1.9	5.2	7.8
SF_6	0.035	6.12	1	58	87
O_2	0.041	1.309	2	5.3	8.0
Ar	0.056	1.634	2	4.9	7.3
CO_2	1.49	1.811	1.8	0.24	0.36
SO_2	87.5	2.408	2	0.0046	0.0069
NH_3	177	0.704	6.9	1.9×10^{-4}	2.9×10^{-4}
Decane	5.2×10^{-5}	730	0.75	6.2×10^{6}	9.4×10^{6}
HDODA	0.343	1202	0.65	1.7×10^{3}	2.7×10^{3}
Heptanol	4.0	919	0.8	96	144
MMA	15	936	0.88	24	35

For microscopic droplets, for which the interface is strongly curved, the concentration at the droplet interface $c_s^{\rm curve}$ is a little bit larger due to the geometric effect of the curvature, thus enhancing dissolution, and it is given by the Ostwald equation [see, e.g., the discussion in Kaptay (2012)[2]]

$$c_s^{\rm curve} = c_s \exp\left(\frac{3\sigma V}{Rk_BT}\right), \tag{21}$$

where σ is the surface tension of the respective interface, k_B is the Boltzmann constant, and V is the molecular volume of a molecule. As one can see, the correction factor becomes relevant only below a length scale of $R_{\rm Ostwald} = 3\sigma V/k_BT$ which is in the range of subnanometer. Therefore, for the nanodroplets and nanobubbles discussed in this review these corrections are negligible.

3. Growing bubbles

We now come to the case of gas oversaturation $c_\infty > c_s$ or $\zeta > 0$ which can lead to growing bubbles or droplets. Such bubble growth can occur after bubble nucleation in a gas-oversaturated liquid, so here directly after the ethanol-water exchange, but only provided that the initial bubble nucleus is sufficiently large: Otherwise it will immediately be squeezed out by surface tension, as shown in Sec. VI.A.2. In other words, for oversaturation $\zeta > 0$ the equilibrium radius (for which $\dot R = 0$ holds) of a bulk bubble is unstable: The free bubble either shrinks and quickly dissolves or grows so that buoyancy finally takes over. The only way for small bulk bubbles to stabilize is to attach to some surface [cf. the crevice model by Harvey *et al.* (1944), Atchley and Prosperetti (1989), and Borkent, Gekle *et al.* (2009)], as discussed in Sec. VI.D.

Coming back to the free bulk bubble, and provided that its nucleus is so large that it is not squeezed out immediately by surface tension, also for this growing bubble case Eq. (15) can be integrated, which after transients results in (Epstein and Plesset, 1950)

$$R(t) \approx R_0\left[\left(\frac{\alpha}{2\pi D}\right)^{1/2} + \left(1+\frac{\alpha}{2\pi D}\right)^{1/2}\right]\sqrt{\frac{t}{\tau_{\rm life}}}. \tag{22}$$

[2]Further names connected to the equation are Kelvin [cf. Guggenheim (1967), Cazabat and Guéna (2010), and Eggers and Pismen (2010)], Gibbs, and Freundlich, although Freundlich and Kelvin erroneously had the factor 2 rather than 3, which in the context of our discussion here does not make any substantial difference.

Enriquez *et al.* (2014) quantitatively demonstrated the validity of the Epstein-Plesset theory (with wall corrections) for growing microbubbles in CO_2 oversaturated water. Further examples were provided by Brennen (1995) and Leighton (1994).

Up to now we assumed a fixed gas concentration c_∞ far away from the bubble. Such a fixed gas concentration can be achieved only in closed systems. In systems open to the atmosphere in the long term c_∞ adjusts to the saturation concentration c_s of nitrogen and oxygen due to Henry's law. In a closed container filled with gas-oversaturated liquid bubbles can exist, even in the bulk, provided that they are large enough. The reason is that for the dissolved gas molecules it can be energetically more favorable to form a bubble (and energetically "pay" for some emerging surface) rather than to stay squeezed in between the liquid molecules in an energetically expensive state of strong oversaturation. This holds more for bubble nucleation on hydrophobic surfaces, but even in the bulk—away from any surface or even with periodic boundary conditions, it can still be energetically more favorable for the system to form bubbles. From a total energy minimization argument, Weijs, Seddon, and Lohse (2012) analytically calculated the equilibrium radius for bulk bubbles in such oversaturated liquid in a closed system, only using Laplace's law and Henry's law, finding excellent and quantitative agreement with corresponding MD simulations as pointed out in Sec. V.C.

We conclude from the analysis of this section that large bulk bubbles can live rather long, namely, for gas concentration around saturation $\zeta \approx 0$. In closed containers ζ cannot change at all. In general, it is determined by diffusive exchange with the outside world, which in partly closed containers of sufficiently large size can take very long.

But small nitrogen (or air) bubbles $\ll 2\sigma/P_0 \approx 1.4\ \mu$m must all dissolve in the bulk within less than about 50 ms, independent of the saturation level [apart from cases of oversaturation when the condition sharpens to $R_0 \ll 2\sigma/(P_0 c_\infty/c_s)$]. However, we recall the assumptions in this section: a spherical single bubble in a bulk liquid, no interaction with any wall, nor with any other bubble. In the case of surface nanobubbles one is tempted to simply replace the radius of the Epstein-Plesset analysis by the radius of curvature R of the bubble, as the Laplace pressure is then given by $2\sigma/R$. However, this assumes that there is free slip of the three-phase gas-liquid-solid contact line on the surface, so that the bubble can shrink without any effect of the surface forces and without any effect of the surface on the gas concentration field. Both assumptions are clearly not correct and we discuss the required modifications of the Epstein-Plesset theory in the context of surface nanobubbles in Sec. VI.D.

Nonetheless, over the last 15 years, Epstein-Plesset–type estimates for the bubble lifetime with the assumption of a spherical bubble were often taken as a gospel of truth also in the context of surface nanobubbles, thus stating that the experimentally observed long bubble lifetime would be paradoxical, and various theories were developed to account for this observed long bubble lifetime.

In Secs. VI.B and VI.C we outline two of these theories; in Sec. VI.D we revisit the Epstein-Plesset theory, but with the necessary adoptions from the case of spherical isolated bulk bubbles toward the case of surface nanobubbles.

B. Contamination theory

The first suspects for the stabilization of bubbles in a liquid were contaminations of the gas-water interface. It has been colloidal science textbook knowledge for decades that water-air interfaces are particularly vulnerable to surfactant accumulation (Israelachvili, 1991) which even affects the bubble rise velocity due to the modified boundary conditions at the interface (Harper, 1973). The surfactants also affect (normally lower) the surface tension and hinder the gas exchange between the bubble and the liquid (Barnes, 1986), thus stabilizing the bubble in two ways. In fact, in diagnostic ultrasonic imaging bubbles coated with lipids or polymers (and thus stabilized) are used as ultrasound contrast enhancers (Schlief, 1991; Nanda and Schlief, 1993; Burns, 1996; Lindner, 2004). Microbubble stabilization is also achieved by the addition of amphiphilic molecules which block the outgas flux from the bubble (Dressaire *et al.*, 2008).

Ducker (2009) transferred this knowledge to surface nanobubbles, hypothesizing that both their stability and their small contact angle would originate from contaminations acting as surfactants, decreasing the surface tension and hindering diffusion out of the bubble, eventually leading to bubble stabilization. He suggests that, apart from being omnipresent anyhow, the (organic) contaminations could originate from the ethanol-water exchange process and that, due to a small total interfacial area (small size and typically low surface coverage $\ll 10\%$), small amounts of contamination would be sufficient, the more as they further accumulate during the shrinkage process of the bubble.

Ducker (2009)'s theory has been criticized, based on (i) a quantitative analysis of the idea and based on (ii) further experimental observations:

(i) Das, Snoeijer, and Lohse (2010) theoretically and quantitatively worked out Ducker's contamination theory by estimating the dependence of the surface tension, the contact angle, and the Laplace pressure on the fraction of impurity coverage at the liquid-gas interface, based on a thermodynamic approach employing the Butler equation which describes the chemical equilibrium of some impurity on an interface (Butler, 1932). They found that the equilibrium adsorption of soluble surfactants to the air-water interface can reduce the surface tension to values around $\sigma = \sigma_{LG} \approx 0.025 - 0.03$ N/m (rather than 0.072 N/m for the pure air-water interface), leading, on the one hand, according to Eq. (1) to a contact angle smaller than expected for clean bubbles, but, on the other hand, not large enough to sufficiently reduce the Laplace pressure to account for the bubble stability. The blockage effect of the contaminations on the gas exchange was not considered by Das, Snoeijer, and Lohse (2010). Later Das (2011) showed that even small surface concentrations of the surfactants have relatively large effect

on the effective surface tension and the contact angle.

(ii) Further evidence against the conjecture that the contamination theory of Ducker (2009) was provided by Zhang, Uddin *et al.* (2012) who washed away potential impermeable materials with various surfactants. Assuming there were impermeable contaminates on the nanobubble surfaces, these contaminates would be washed off or replaced by surfactants when a solution of surfactant with positive, negative, or nonionic groups were introduced into the system. The concentration of the surfactants must be above CMC to obtain effective detergency. To test the hypothesis of Ducker (2009), Zhang, Uddin *et al.* (2012) imaged nanobubbles in water and in various surfactant solutions. The measurements confirmed that nanobubbles remained on the surface in cationic, anionic, and nonionic surfactant solutions. This stability in the presence of micellar solutions thus does not support the hypothesis that surface nanobubbles are stabilized by water insoluble materials adsorbed at their gas-liquid interface (Zhang, Uddin *et al.*, 2012). German *et al.* (2014) also found that the gas-liquid interface of nanobubble is fully gas permeable, in contrast to the theory of Ducker (2009).

In this section we also mention the speculation that the surface nanobubble stabilization is due to hydroxide ion adsorption on the bubble surface (Karraker and Radke, 2002) and/or the effect of induced charges in the Debye layer around the bubble interface (Jin *et al.*, 2007; Duval *et al.*, 2012). The argument is that the double layer at the gas-water interface reduces the surface tension and thus the internal pressure. However, as mentioned previously, a pH change has no effect on the nanobubbles and we therefore consider it as unlikely that hydroxide ion adsorption plays any important role in the surface nanobubble stabilization.

C. Dynamic equilibrium theory

Because of the limitations and problems of the contamination theory, Brenner and Lohse (2008) postulated a dynamic equilibrium mechanism to account for the long lifetime of surface nanobubbles. The key idea is visualized in Fig. 31: The surface tension driven gas outflux from the nanobubble is compensated by a gas influx close to the contact line, as the hydrophobic surface preferentially attracts gas molecules, rather than water molecules. The bubble then would be in a dynamic equilibrium.

The idea of Brenner and Lohse (2008) dynamic equilibrium hypothesis was triggered by the finding of Yang *et al.* (2009) that *electrolytically* generated nanobubbles do not further grow beyond a certain size, in spite of an electrical current which produces gas molecules—so those electrolytically generated nanobubbles are out of equilibrium. However, what is the driving mechanism for the nanobubbles generated by droplet deposition or by the solvent exchange process? Brenner and Lohse (2008) gave various speculations, ranging from some temperature gradient to the droplet evaporation process (Seddon *et al.*, 2012), which provides energy. In any case, it is clear that once this driving mechanism is expired or stopped (for the evaporation, e.g., by placing the droplet in a water-saturated environment) and the system is adiabatic, that then the nanobubble must still dissolve.

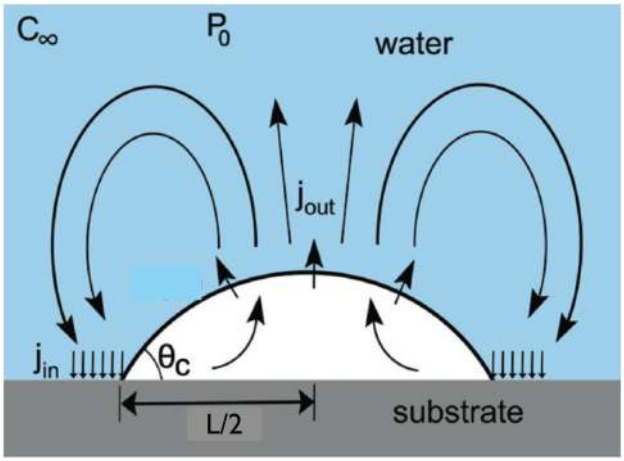

FIG. 31 (color online). The key idea of the dynamic equilibrium theory of Brenner and Lohse (2008): The surface tension driven gas outflux j_{out} from the surface nanobubble (with footprint diameter L) is compensated by a gas influx j_{in} close to the contact line. From Petsev, Shell, and Leal, 2013.

The dynamic equilibrium theory was further elaborated by Seddon, Zandvliet, and Lohse (2011) by postulating an upward liquid flow outside the bubble which would be driven by a directional gas flow inside the bubble, which would be due to the asymmetric adsorption properties of the gas inside the bubble at the solid-gas interface and the liquid-gas interface. Seddon, Zandvliet, and Lohse (2011) also provided measurements of an upward liquid flow above the surface nanobubbles, but this flow could not be confirmed in later measurements[3]; neither could a lateral liquid flow be found (Chan and Ohl, 2012; Dietrich *et al.*, 2013), which one would expect to be the direct consequence of the upward flow.

Petsev, Shell, and Leal (2013) developed an alternate formulation of the dynamic equilibrium theory. They employed a more realistic empirical model for the hydrophobic attraction of the gas molecules toward the surface, thus avoiding an artificially high effective line tension, which had to be assumed by Brenner and Lohse (2008) to guarantee a sufficiently large gas influx into the bubble. Yasui *et al.* (2015) extended the work by Brenner and Lohse (2008) by explicitly taking into account the van der Waals attractive force between gas molecules inside the nanobubble and the solid surface.

In any formulation, the Achilles heel of the dynamic equilibrium theory is that it is unclear what the driving mechanism is. In addition, the experimental bubble size distribution is rather broad, in contrast to the predictions of the dynamic equilibrium theory (again in any formulation), although this distribution may be accounted for by inhomogeneities of the flow or the substrate.

[3]R. Berkelaar, D. Lohse, and H. Zandvliet (private communication).

D. Diffusive dynamics of pinned surface nanobubbles and nanodroplets

1. Diffusion around surface bubbles and drops

We now come back to the Epstein and Plesset (1950) theory for the dissolution (or growth) of spherical bubbles in the bulk, but adopt it to the situation of surface nanobubbles and nanodroplets. They are assumed to be sitting on a plane surface and to be of spherical-cap shape as in Fig. 2(b). Their dissolution or growth is described by the same diffusion equation (7), but now the situation is axisymmetric and other boundary conditions must be imposed. In the quasisteady, diffusion-limited case, in which the diffusion is the rate-limiting mechanism (which is the relevant case for still water around the bubble or drop), the diffusion equation for the concentration field $c(r,z)$ around the droplet or bubble simplifies to $\nabla^2 c = 0$. Far away from the droplet or bubble we still have $c = c_\infty$, but as the substrate is impermeable, at the plane surface we have the no flux condition $\partial c/\partial z = 0$. In general, the diffusive flux is given by $\mathbf{J} = -D\nabla c$. Along the droplet surface for the considered diffusion-limited case [of either a dissolving (or growing) liquid droplet in another liquid (neglecting surface tension effects) or in ambient still gas] we have the saturated mass concentration $c = c_s$ as a boundary condition; for a dissolving (or growing) gas bubble in liquid we still have Henry's law (9) with the gas pressure $p_g(t)$ as given by Eq. (12) as a boundary condition, with the radius of curvature R in that equation given by $R = L/(2\sin\theta)$ [see Eq. (4) and Fig. 2(b)], i.e.,

$$p_g(t) = P_0 + \frac{4\sigma\sin\theta}{L}. \tag{23}$$

Here we neglected again the vapor pressure and also the disjoining pressure, which we discuss in Sec. VI.D.4.

Deegan *et al.* (1997) and Hu and Larson (2002) calculated the approximate droplet evaporation rate in the small contact angle limit. Popov (2005) solved the full problem for any contact angle, using an elegant analogy to the electric potential around a charged lens-shaped conductor. For a recent review on sessile droplet evaporation see Cazabat and Guéna (2010). The droplet dissolution rate in another liquid follows the same equations as the droplet evaporation rate in ambient air, provided both are diffusion controlled and liquid-liquid surface tension effects can be neglected. The result for the mass loss rate dM/dt of the droplet is (Popov, 2005; Gelderblom *et al.*, 2011)

$$\frac{dM}{dt} = -\frac{\pi}{2}LD(c_s - c_\infty)f(\theta), \tag{24}$$

with

$$f(\theta) = \frac{\sin\theta}{1+\cos\theta} + 4\int_0^\infty \frac{1+\cosh 2\theta\tau}{\sinh 2\pi\tau}\tanh[(\pi-\theta)\tau]d\tau, \tag{25}$$

which is positive definite. Lohse and Zhang (2015) generalized Eq. (24) to the bubble case, for which the concentration boundary conditions at the interface are given by Henry's law (9) and not by the saturation concentration c_s as in the case of droplets, obtaining

$$\frac{dM}{dt} = -\frac{\pi}{2}LD\left[\left(P_0 + \frac{4\sigma\sin\theta}{L}\right)\frac{c_s}{P_0} - c_\infty\right]f(\theta). \tag{26}$$

With the gas (or droplet) density ρ_g the mass M can be expressed in terms of the footprint diameter L and the contact angle θ as

$$M(\theta) = \rho_g\frac{\pi}{8}L^3\frac{\cos^3\theta - 3\cos\theta + 2}{3\sin^3\theta} =: \rho_g\frac{\pi}{8}L^3\ g(\theta). \tag{27}$$

2. Pinning

Now the crucial assumption first put forward by Zhang, Chan *et al.* (2013) and by Weijs and Lohse (2013) is pinning of the contact line, so that the lateral extension L is fixed, and so is the footprint area. The same pinning assumption has also been made for evaporating (Deegan *et al.*, 1997; Hu and Larson, 2002; Popov, 2005; Li, Butt, and Graf, 2006; Schönfeld *et al.*, 2008; Marin *et al.*, 2011) or dissolving (Zhang, Wang *et al.*, 2015) surface or sessile droplets. It is one of the two limiting cases already identified by Picknett and Bexon (1977) for general droplet evaporation, next to the constant contact angle mode, which we discuss in Sec. VI.F.

The pinning assumption is justified by various experimental observations, for both shrinking and growing nanobubbles; see, e.g., Fig. 22 and our discussion in Sec. IV. The origin of contact line pinning is discussed in Sec. VI.E. Pinning implies that in contrast to bulk nanobubbles the Laplace pressure is decreasing once the volume of the bubble (and thus its height H) is decreasing. Vice versa, for increasing bubble volume the Laplace pressure is also increasing, counteracting further increase, i.e., for pinned surface nanobubbles the Laplace pressure provides a negative feedback to a volume change, very different from bulk nanobubbles, for which the feedback is positive to accelerate bubble dissolution.

For dissolution (or growth) or evaporation (or condensation) of pinned droplets, the ordinary differential equation (ODE) for the contact angle θ resulting from Eqs. (24) and (27) reads (again neglecting surface tension effects)

$$\frac{d\theta}{dt} = \frac{4D}{L^2}\frac{c_s}{\rho_d}(1+\cos\theta)^2 f(\theta)\zeta, \tag{28}$$

which can easily be solved and, for the case of an evaporating pinned droplet in still ambient air, gives excellent agreement with experimental data (Gelderblom *et al.*, 2011; Marin *et al.*, 2011). From Eq. (28) one can immediately see that it is only the oversaturation ζ which determines growth ($\zeta > 0$, oversaturation) or shrinkage ($\zeta < 0$, undersaturation).

For pinned surface nanobubbles (or immersed droplets with surface tension at the interface), the corresponding ODE for $\theta(t)$ reads (Lohse and Zhang, 2015)

$$\frac{d\theta}{dt} = \frac{4D}{L^2}\frac{c_s}{\rho_g}(1+\cos\theta)^2 f(\theta)\left[\zeta - \frac{L_c}{L}\sin\theta\right], \tag{29}$$

with the critical lateral extension $L_c = 4\sigma/P_0 \approx 2.84\ \mu$m for air bubbles in water under ambient conditions. For

undersaturation ($\zeta < 0$) the Laplace pressure (resulting in the second term in the brackets) accelerates the shrinkage of the bubble and no equilibrium exists. In contrast, for oversaturation ($\zeta > 0$) the Laplace pressure counteracts the growth, which can lead to a stable equilibrium at (Lohse and Zhang, 2015)

$$\sin\theta_e = \zeta \frac{L}{L_c}. \tag{30}$$

Such an equilibrium occurs for small enough pinning sites

$$L < L_c/\zeta. \tag{31}$$

The equilibrium indeed is stable: From Eq. (29) one can immediately read off that bubble with a smaller contact angle $\theta < \theta_e$ grows toward θ_e, whereas bubbles with a larger contact angle $\theta > \theta_e$ shrink down to θ_e. This situation is sketched in Fig. 32, in which we also give some typical values for the equilibrium angles θ_e for various oversaturations. The equilibrium contact angle θ_e is not the macroscopic contact angle given by Young's equation (1) or its extended version (5) as both equations are irrelevant for pinned contact lines, but it is simply set by the stable equilibrium between gas influx and outflux,[4] resulting in a very small value for θ_e for typical gas oversaturations ζ; see Fig. 32(b).

The equilibrium result (30) can also immediately be obtained from simply balancing the Laplace pressure inside the pinned surface bubble with the oversaturation pressure ζP_0 according to Henry's law. It can also be expressed in terms of the equilibrium curvature

$$R_e = \frac{L_c}{2\zeta}, \tag{32}$$

which is constant for constant oversaturation ζ. The advantage of the above dynamical analysis is that it also gives the time scale on which the equilibrium is achieved, namely, as can be read off from Eq. (29),

$$\tau_{\text{inner}} = \frac{L^2}{4D}\frac{\rho_g}{c_s}. \tag{33}$$

We call this the inner time scale of the diffusive dynamics and it corresponds to the Epstein-Plesset time scale τ_{life} [Eq. (20)] of Sec. VI.A and, in particular, Table II. But note that for flat bubbles the trigonometric correction factor $(1+\cos\theta)^2 f(\theta)$ can be rather large, so that the (inner) diffusive dynamics of surface bubbles is much faster than that of bulk bubbles.

The above analysis reveals what surface nanobubbles are in contrast to surface microbubbles: They are so small that the resulting Laplace pressure is large enough to counteract the gas influx by gas oversaturation, i.e., Eq. (31) must hold.

[4]We note that this had also been the key idea of Brenner and Lohse (2008) dynamic equilibrium theory, although there it was not realized that it is simply the gas oversaturation which provides the gas influx, as then it was unknown that $\zeta > 0$ is necessary to obtain stable surface nanobubbles.

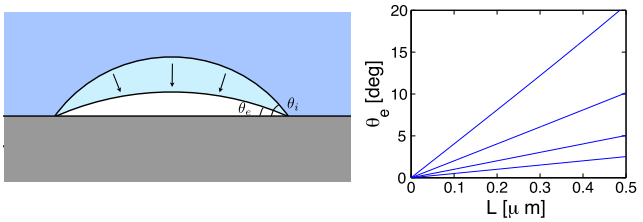

FIG. 32 (color online). (Left) Sketch of the shrinking process of a pinned surface nanobubble with footprint diameter L and initial contact angle $\theta_i > \theta_e$ toward the equilibrium contact angle θ_e. (Right) Equilibrium contact angle θ_e of a nitrogen bubble in water as a function of the lateral footprint size L for four different oversaturations $\zeta = 0.25$, 0.5, 1.0, 2.0, bottom to top. From Lohse and Zhang, 2015.

In contrast, surface microbubbles simply grow in a gas-oversaturated solution and finally detach due to buoyancy.

To illustrate the stability of pinned surface nanobubbles and to contrast it to the unstable bulk bubbles or to the unstable surface bubbles with a constant contact angle (to be discussed in Sec. VI.E) we sketch the respective phase spaces $\dot{\theta}$ vs θ and $\dot{L}$ vs L in Fig. 34.

We finally mention that a completely analogous stabilization mechanism as that of pinned nanobubbles in gas-oversaturated water also works for pinned nanodroplets in vapor-oversaturated air, as demonstrated by Liu and Zhang (2013a) with theoretical arguments and kinetic lattice density functional theory; see Fig. 35. Again, the Laplace pressure is crucial: At the stable equilibrium, it counteracts and thus balances the condensation of vapor molecules out of the oversaturated gas phase on the liquid droplet. The same Eqs. (29) to (33) can be applied to calculate the dynamics and the equilibrium contact angle θ_e of the droplet in air.

3. What determines the gas oversaturation ζ?

We have seen that the oversaturation ζ determines the existence and the value of the equilibrium contact angle θ_e; see Eq. (30). But what determines ζ? It is the diffusion of gas around the surface bubble to the outside world. Assume that the surface and the bubble have a distance $\ell \gg H$ to the outer world. Then the corresponding time scale of this diffusion process is

$$\tau_{\text{outer}} \sim \frac{\ell^2}{D}. \tag{34}$$

This time scale was first introduced into the nanobubble research by Weijs and Lohse (2013). They assumed that the density of the surface nanobubble is statistically homogenous. Then for distances z from the wall which are much larger than the typical interbubble distance, i.e., in the far field, it can be assumed that the gas concentration field depends only on the wall distance z and on time. $c(z,t)$ is then given by the one-dimensional diffusion equation $\partial_t c = D\partial_z^2 c$ with the boundary conditions $c(z=0,t) = c_0(t)$ given by Henry's law and $c(z=\infty,t) = c_\infty$ and an initial concentration field. The one-dimensional diffusion equation can easily be solved through a Laplace transform (Prosperetti, 2011), resulting in the full

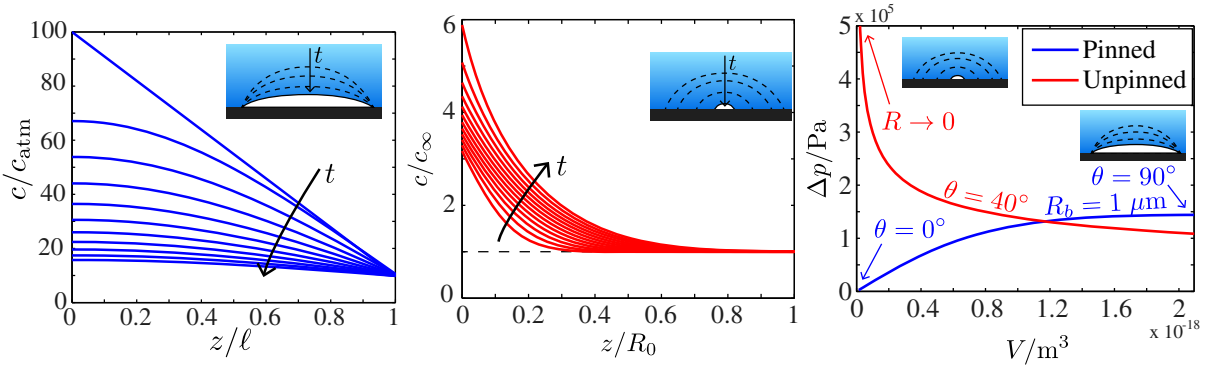

FIG. 33 (color online). Concentration profiles shown at $t = 0$, 10 000, 20 000, 30 000 s, etc. following from Weijs and Lohse (2013) (left panel), which assumes pinning of the contact line. The gradient at the bubble wall $z = 0$ quickly becomes flat. These profiles can in fact be calculated analytically in the zero-gradient limit, giving $c(z,t)/c_s \propto \exp(-\pi^2 Dt/4\ell^2)\cos(\pi z/2\ell)$, apart from transient effects. Middle panel: No pinning is assumed (for $R_0 = 100$ nm), leading to a steep concentration gradient at the bubble wall and thus to much faster shrinkage, as for a spherical bubble in the bulk (Epstein and Plesset, 1950). The profiles are shown at times $t = 10^{-8}$, 1.4×10^{-8}, 1.8×10^{-8}, 2.2×10^{-8} s, etc. Right panel: The Laplace pressures $P_{\text{Laplace}} = 2\sigma/R$ with and without pinning are compared.

concentration field $c(z,t)$. Weijs and Lohse (2013) then calculated the long-time diffusional dynamics for a dissolving pinned surface nanobubble (i.e., $\zeta < 0$). They found that the gas concentration field has nearly zero slope at the bubble-liquid interface $z = 0$; see Fig. 33(a): Once the bubble volume gets smaller, the pressure $p_g(t)$ inside the bubble goes down [see Fig. 33(c)], slowing down further gas transfer from the bubble toward the liquid. This is also reflected in the concentration profiles: While without pinning or for bulk nanobubbles the concentration profiles get steeper and steeper with advancing time [see Fig. 33(b)], with pinning the profiles get less and less steep, slowing down the dissolution.

The distance ℓ between the surface nanobubble and the outside world is thus the central new parameter introduced by Weijs and Lohse (2013). For typical parameters the lifetimes (34) are 1 to 2 days, rather than the submilliseconds (for gases) of the inner time scale (33) and of the Epstein and Plesset (1950) calculation. Note the strong (quadratic) dependence (34) on the length scale parameter ℓ. This dependence is the most pronounced prediction of the model of Weijs and Lohse (2013) and it is open to experimental and numerical (MD) verifications.

These are, however, nontrivial: On the experimental side, long-time observations of surface nanobubbles with well-defined and constant distance ℓ between surface nanobubble and outer atmosphere have not yet been performed for the required duration of many hours to days: For surface nanobubbles generated by droplet deposition the droplet may be evaporated in a shorter time when no special control of the ambient vapor saturation has been taken care of. On the other hand, for surface nanobubbles generated in flow cells, e.g., with the alcohol water exchange procedure, the distance ℓ is not well defined either, and the opening of the flow cell often is small, so that when starting with a gas-oversaturated liquid it is not surprising that the surface nanobubbles dissolve only extremely slowly. Clearly, experiments with controlled and varying ℓ should be performed.

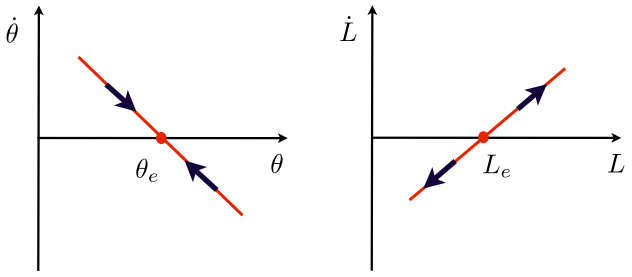

FIG. 34 (color online). (Left) Sketch of the stable equilibrium θ_e for pinned surface nanobubbles in the $\dot\theta$ vs θ phase space. A sketch of the volume phase space $\dot V$ vs V or of the bubble height phase space $\dot H$ vs H looks the same. (Right) Sketch of the unstable equilibrium L_e for unpinned surface nanobubbles with constant contact angle in the $\dot L$ vs L phase space. A sketch of the volume phase space $\dot V$ vs V looks the same. Also for bulk bubbles, the sketch looks the same, with the lateral extension L then meaning the bubble diameter or being replaced by the radius R or the volume V of the bulk bubble. From Lohse and Zhang, 2015.

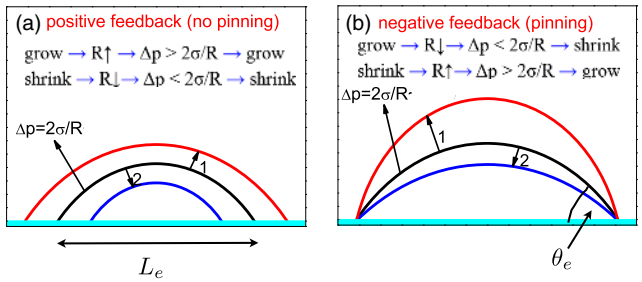

FIG. 35 (color online). Stabilization mechanism of evaporating surface nanodroplets in an oversaturated gas atmosphere through pinning: In (a) the droplet is not pinned, leading to a diverging Laplace pressure and thus evaporation of the droplet for any oversaturation. The equilibrium situation with footprint diameter L_e [Eq. (39), black curve] is unstable. In (b) the droplet is pinned. The equilibrium situation with contact angle θ_e [Eq. (30), black curve] is stable. Adapted from Liu and Zhang, 2013a.

4. Disjoining pressure

For very small bubbles the disjoining pressure

$$\Pi_d(h) = -A/(6\pi h^3) \tag{35}$$

[with some cutoff at small h of the order of a few molecular distances (Pismen and Pomeau, 2000)] will become relevant; see, e.g., the reviews by Bonn *et al.* (2009), Cazabat and Guéna (2010), and Snoeijer and Andreotti (2013), or de Gennes, Brochard-Wyart, and Quere (2004). Here h is the height of the interface and A is the Hamaker constant. The disjoining pressure represents the long-range van der Waals forces including the long-range Casimir forces, which for standard surfaces and water are attractive. Note that it is closely related to the so-called spreading parameter S through the relation $\int_0^\infty \Pi_d(h)dh = S = \sigma_{SL} - (\sigma_{SG} + \sigma_{LG})$ (de Gennes, Brochard-Wyart, and Quere, 2004).

The disjoining pressure must be included as a small additive correction to the Laplace pressure in Eq. (23). Obviously, its effect is largest at the rim of the surface nanobubble where it in principle leads to a small deviation of the spherical-cap shape. As for very small bubbles the disjoining pressure modifies the Laplace pressure inside the (pinned) surface nanobubbles, it also implies a small shift of the equilibrium contact angle θ_e. It may also limit the minimal equilibrium contact angle toward some small threshold value θ^*, below which the gas-liquid interface is attracted toward the surface so that the three-phase contact line is zipped inward, leading to an inward jump of the contact line and an upward jump of the contact angle. All these effects have quantitatively been worked out by Svetovoy *et al.* (2015). They also showed that the effect of the disjoining pressure on the shape of surface nanodroplets is even more negligible.

E. Origin of contact line pinning: Surface heterogeneities

As seen, the assumption of pinning is crucial to account for the long lifetime of surface nanobubbles. But what is the origin of pinning? We already mentioned that chemical and geometrical surface heterogeneities lead to pinning of contact lines; see the reviews by de Gennes (1985), Leger and Joanny (1992), Nadkarni and Garoff (1992), Quere (2008), Bonn *et al.* (2009), and Snoeijer and Andreotti (2013). Such heterogeneities are omnipresent and unavoidable on any solid surface. They also lead to contact line hysteresis, i.e., the difference between an advancing and a receding contact angle (Neumann *et al.*, 1974; Joanny and de Gennes, 1984; de Gennes, Brochard-Wyart, and Quere, 2004; Quere, 2008; Ramiasa *et al.*, 2013). Indeed, Ramos, Charlaix, and Benyagoub (2003) showed that the amount of contact angle hysteresis linearly increases with the density of defects on nanostructured surfaces (provided it is not too high), due to the pinning-depinning process of the contact line at individual defects.

A top-view sketch of the pinning of the surface nanobubbles and nanodroplets at chemical heterogeneities is shown in Fig. 36(a). The surface nanobubbles (nanodroplets) adhere to the hydrophobic patches. Even though the patches will in general not be round, round bubble shapes will be

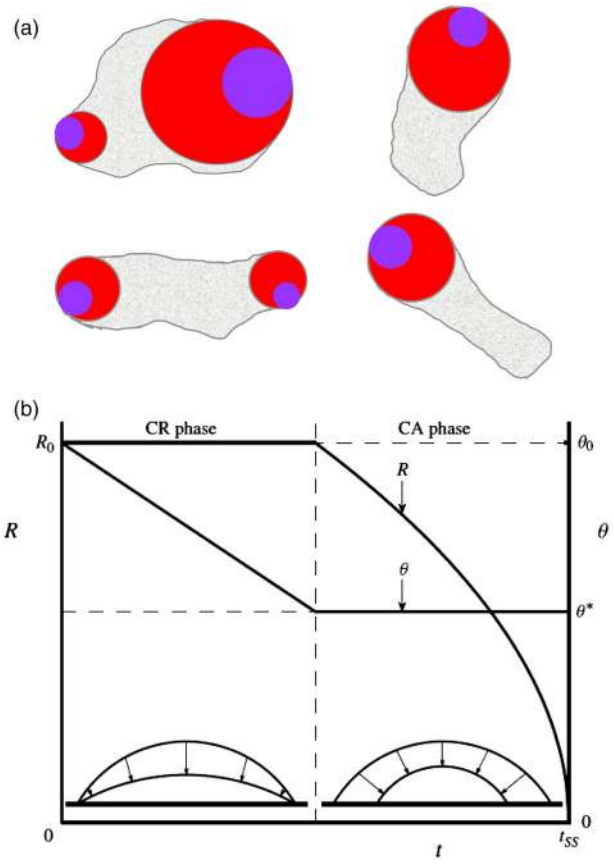

FIG. 36 (color online). (a) Top-view sketch of patches of chemical heterogeneities (light shaded) on the surface. They are more hydrophobic and surface nanobubbles or nanodroplets (larger shaded circles) adhere to them. If exposed to a (partly) degassed or undersaturated water environment ($c_\infty < c_s$ or $\zeta < 0$), the nanobubbles (or nanodroplets) shrink, first in the constant footprint mode (CR mode) due to the pinning, and then jump toward a smaller footprint (CA mode), as drawn by the smaller shaded nanobubbles and nanodroplets. (b) Scheme of a shrinking droplet in the stick-slip mode. The drop transitions from the constant (footprint) radius mode (CR) to the constant contact angle mode (CA). From Stauber *et al.*, 2014. More realistically, the jump in the CA will be only on one side, due to in general different pinning strengths on the two sides, leading to a shift in the center of mass, as shown in (a).

favorable due to the lower overall surface energy. Once the (partially) pinned nanobubbles (nanodroplets) [larger shaded circles in Fig. 36(a)] shrink by dissolution in an undersaturated environment ($c_\infty < c_s$), at some point it will be energetically favorable to jump toward a shape with smaller footprint size (smaller shaded circles), still partially being pinned at one side of the hydrophobic patch; see Figs. 36(b) and 37 for side views. Note again that the jump in generally occurs asymmetrically, as the pinning in one particular region of the three-phase contact line will always be stronger than at some other parts thereof. Such asymmetrical jumps have indeed been observed for dissolving microdroplets (Dietrich *et al.*, 2015; Zhang, Wang *et al.*, 2015).

Further support for the view of pinning caused by chemical heterogeneities on the surface is also coming from

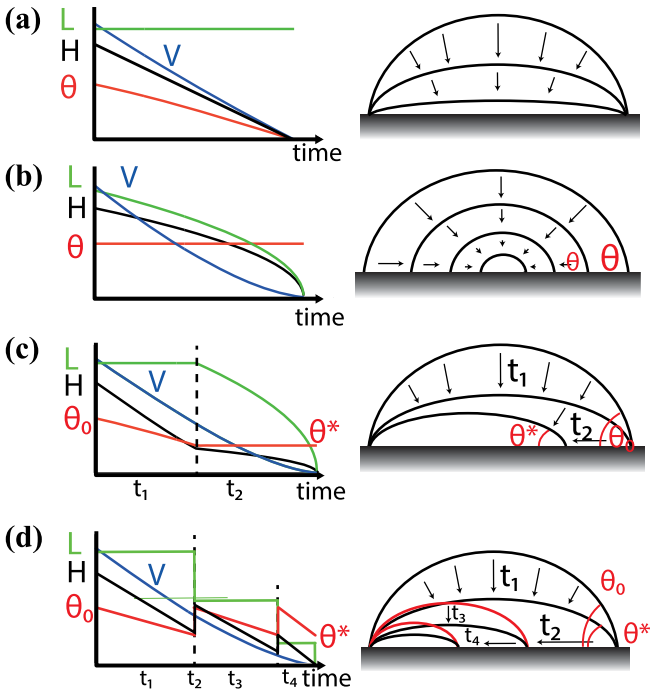

FIG. 37 (color online). Schemes of the four possible dissolution modes of a surface nanodroplet (or a surface nanobubble): (a) CR mode, i.e., constant contact radius due to perfect pinning. (b) CA mode, i.e., constant contact angle. (c) Stick-slide mode, i.e., the nanodroplet dissolves in an iteration of the CR and CA modes. (d) Jumping mode. The droplet first is in a CR mode, but for an angle smaller than θ^* jumps toward a smaller constant radius due to sudden depinning on one side. Because of mass conservation at the jump the droplet height and contact angle jump up. After the jump, the droplet is again in a CR mode, up to the next jump, finally resulting in a cascade of jumps (not drawn). From Zhang, Wang *et al.*, 2015.

reports[5] that the density of surface nanobubbles seems to increase with increasing time a freshly cleaved HOPG surface is exposed to the ambient air, before being immersed in water. We think that it should be possible to visualize such hydrophobic patches by AFM. The role of geometric inhomogeneities for pinning was directly demonstrated by Yang *et al.* (2008) who showed that surface nanobubbles preferably nucleated at the atomic steps of HOPG. Yang *et al.* (2003) showed that the roughness of methylated surfaces had a direct effect on the surface nanobubble size and density.

Another relevant observation in this context is that in the nanobubble nucleation experiments by Hain *et al.* (2015), nanobubbles emerge only after piranha cleaning of the glass surfaces, which presumably causes surface roughness and little crevices on which the nanobubbles can nucleate and pin.[6] In contrast, Hain *et al.* (2015) did not observe nanobubbles on plasma-cleaned or UV and ozone-cleaned glass surfaces by combined AFM-FLIM measurements.

[5]Yaming Dong (private communication).

[6]Note that other groups could not generate nanobubbles on hydrophilic substrates as reported in Sec. II.

The numerical simulation of Liu and Zhang (2013b) (LDFT) and Liu and Zhang (2014) (MD) supported how crucial pinning at heterogeneities is for the surface nanobubble stability, as already reported in Sec. V.D and shown in Fig. 30. Within their LDFT approach, Liu *et al.* (2014) calculated the magnitude of the pinning force which is necessary to stabilize nanobubbles. Before they had already shown with the same method that pinning can stabilize sessile droplets in vapor-supersaturated air (Liu and Zhang, 2013a). They used physical heterogeneities (roughness), but we could show that also chemical heterogeneities (hydrophobic patches) lead to pinning of MD nanobubbles and nanodroplets.

Clearly, more work must be done to further explore contact line pinning on the submicron scale. Dissolving or growing surface nanobubbles and nanodroplets may be seen as a "probe," probing the pinning dynamics on submicron scales, as their lateral scales are comparable to those of the relevant surface heterogeneities. Therefore the effect of the surface heterogeneities no longer averages out as is the case for droplets on larger scales, on which contact angle hysteresis is observed.

F. Further dissolution modes of surface nanobubbles and nanodroplets

In the last two sections we discussed pinned surface nanobubbles and nanodroplets and, in particular, elaborated how pinning (i.e., fixed footprint diameter L and thus fixed footprint radius), together with oversaturation, can stabilize them. We also showed that for undersaturation ($\zeta < 0$), pinning cannot prevent dissolution or evaporation, and bubbles or droplets dissolve or evaporate in that pinning mode, which here we call the "CR mode" (standing for constant footprint radius).

Next to the pinning mode, the second limiting case (Picknett and Bexon, 1977) for droplet evaporation or dissolution is the one with fixed contact angle θ, called the "CA mode," standing for constant angle. Then for droplets, again neglecting surface tension effects, from Eqs. (24) and (27) one obtains an ODE for the footprint diameter L, namely,

$$L\dot{L} = \frac{4Dc_s}{\rho_d}\frac{f(\theta)}{3g(\theta)}\zeta, \tag{36}$$

which can be integrated to obtain the time evolution for the footprint diameter of the dissolving droplet ($\zeta < 0$, undersaturation) with constant contact angle θ,

$$L(t) = \left(L_0^2 + \frac{8c_sD}{\rho_d}\zeta\frac{f(\theta)}{3g(\theta)}t\right)^{1/2}. \tag{37}$$

The same equation holds for oversatuation and the resulting droplet growth ($\zeta > 0$). Apart from the trigonometric correction factor $f(\theta)/3g(\theta)$ (which for small contact angles can be much larger than 1), the time scale of dissolution is still given by L_0^2/α with α as in Eq. (17) (as for a dissolving droplet surface tension does not play a role).

For the bubble case, we obtain

$$L\dot{L} = \frac{4Dc_s}{\rho_d}\frac{f(\theta)}{3g(\theta)}\left(\zeta - \frac{L_c}{L}\sin\theta\right). \tag{38}$$

For undersaturation $\zeta < 0$, this implies enhanced dissolution (as compared to the droplet case) due to the Laplace pressure. Also Eq. (38) can be integrated analytically, giving an implicit equation (with quadratic, linear, and logarithmic terms of L), out of which $L(L_0, t)$ can be obtained.

For oversaturation $\zeta > 0$ also the constant contact angle case allows for an equilibrium point ($\dot{L} = 0$), namely, at

$$L_e = \frac{L_c}{\zeta} \sin\theta, \tag{39}$$

but this equilibrium is unstable, as one can easily show with a linear expansion around the equilibrium L_e: Surface nanobubbles with $L < L_e$ are pressed out by the Laplace pressure, those with $L > L_e$ grow because of the oversaturation, up to detachment from the surface. The phase space of the situation is sketched in Fig. 34(b).

Apart from the two limiting dissolution modes (CR and CA modes), various mixed modes may exist. Shanahan (1995) and Stauber *et al.* (2014) treated such a mixed mode, namely, neither constant contact angle θ nor perfect pinning. They suggested that a droplet in air evaporates in a "stick-slide" mode; see Fig. 36(b). In that schematic figure it is shown that due to pinning the droplet first is in the constant footprint radius mode (CR) during which the contact angle shrinks. Once the contact angle is too small the geometry becomes energetically unfavorable and now the footprint radius shrinks, while the contact angle remains constant (CA mode). Interestingly, the lifetime of a droplet in such a general mode is not constrained by the lifetimes of the limiting cases CA and CR modes. We assume that in general several stick-slide transitions can occur.

In case that the duration of the CA phase is much shorter than that of the CR phase, the contact line "jumps" inward toward smaller footprint radii, determined by the chemical surface heterogeneities. Such a jump may occur at some minimal contact angle θ^*, which may be determined by the disjoining pressure (see Sec. VI.D.4). If the jumping time is so short that it can be neglected as compared to diffusive time scales, then this "stick-jump mode" can be seen as a generalization of the CR mode, with sudden jumps in between periods of constant contact radius. Note that while in this mode the surface bubble or droplet footprint area $\pi L^2/4$ discontinuously decreases at the jumps, the surface bubble or droplet volume decreases continuously and the bubble or droplet height H and its contact angle θ even increase at the jumps, due to volume conservation, which leads to an enhanced surface bubble or droplet lifetime. Debuisson *et al.* (2011) and Debuisson, Senez, and Arscott (2011) observed such stick-jump modes for evaporating sessile droplets on patterned surfaces. Zhang, Wang *et al.* (2015) and Dietrich *et al.* (2015) observed the stick-jump mode for the dissolution of immersed heptane nanodroplets in clean water on a seemingly smooth surface, but the interpretation again is that chemical and geometric surface inhomogeneities provide the pinning sites at which the jumps take place. Zhang, Wang *et al.* (2015) also observed that the jumps can be asymmetric (as shown in Fig. 13), as the pinning of the droplet is not the same on all sides of the droplet. This implies that the center of mass of the droplet slightly moves back and forth during the dissolution process. We would expect similar behavior for dissolving nanobubbles in this stick-jump mode.

Sketches for the various dissolution modes CR, CA, stick-slide, and stick-jump are shown in Fig. 37.

We stress that the theoretical results of this section and Sec. VI.D hold only for an isolated surface bubble or droplet and that collective effects, which delay the dissolution, have not been considered here. We already discussed them in Sec. IV.E. In numerical simulations (either MD, lattice-Boltzmann type, or continuum simulations) such collective effectives can however be included straightforwardly, by changing the geometry and boundary conditions.

G. Theoretical description of solvent exchange process

The theoretical framework as outlined in the last sections can also be used to describe the growth (or shrinkage) of bubbles and droplets in an environment with temporally varying solvent concentration $c_\infty(t)$ and $c_s(t)$, as it, e.g., occurs during the solvent exchange process described in Sec. II.C and sketched in Fig. 7. These temporal variations imply a time dependence of the oversaturation $\zeta(t) = c_\infty(t)/c_s(t) - 1$. One example was worked out in Zhang, Lu *et al.* (2015): When oil-saturated ethanol is replaced by oil-saturated water, the liquid will be oversaturated in the ethanol-water mixing zone and correspondingly at the fixed position of the droplet or bubble, $\zeta(t) > 0$ for some time, as the oil's solubility is larger in ethanol than in water, and thus $\zeta_{\max} = c_{s,\mathrm{eth}}/c_{s,\mathrm{water}} - 1 > 0$. Consequently, droplets will grow during that time.

For drops or bubbles with fixed contact area (CR mode, i.e., constant L), the time-dependent version of Eq. (28) allows for the calculation of the final contact angle θ_f after the solvent exchange, namely, by solving

$$\int_0^{\theta_f} \frac{d\theta}{(1+\cos\theta)^2 f(\theta)} = \frac{4D}{L^2} \frac{c_{s,\mathrm{water}}}{\rho_d} \int_0^\infty \zeta(t) dt. \tag{40}$$

Also for the constant contact angle mode (CA mode) or for a fully immersed droplet a similar calculation is possible, leading to a final droplet radius

$$R_f \propto \left(\frac{D c_{s,\mathrm{water}}}{\rho_d} \int_0^\infty \zeta(t) dt \right)^{1/2}. \tag{41}$$

The flow rate dependence of the solvent exchange process can be embodied by replacing (in the calculations) the concentration boundary layer thickness $\lambda \sim R$ around the droplet by the Prandtl-Blasius-Pohlhausen result $\lambda \sim R/\sqrt{\mathrm{Pe}}$ (Schlichting, 1979; Grossmann and Lohse, 2004), where Pe is the Peclet number of the flow. For more details again see Zhang, Lu *et al.* (2015).

VII. TECHNOLOGICAL RELEVANCE

The presence of surface nanobubbles and nanodroplets has implications on various interfacial properties and phenomena and thus is relevant for all applications where these properties matter. For example, it was proposed that nanobubbles

enhance the attractive interactions between hydrophobic surfaces (Gong *et al.*, 1999; Mahnke *et al.*, 1999; Faghihnejad and Zeng, 2013), that they initiate thin liquid film rupture (Stöckelhuber *et al.*, 2004; Ajaev, 2006; Ajaev, Gatapova, and Kabov, 2011), prevent bimolecular adsorption (Chen *et al.*, 2009), and help in (acoustically enhanced) surface cleaning (Liu, Wu, and Craig, 2008; Wu *et al.*, 2008; Chen *et al.*, 2009; Liu and Craig, 2009). In fabrication of advanced materials, nanobubbles and/or nanodroplets can provide the platform for templateless synthesis, such as hollow nanoparticles, or may help in particle assembly, such as the formation of particle nanorings (Seo, Yoo, and Jeon, 2007; Darwich *et al.*, 2011).

In this section, we cannot go into depth for all examples of potential technological relevance of nanobubbles and nanodroplets, but will focus on five particular promising ones. Namely, we review the role of surface nanobubbles and nanodroplets (A) for flotation, (B) for nanomaterial engineering, (C) for the transport in nanofluidics and the autonomous motions of nanoparticles, (D) for the role of nanobubbles in catalysis and electrolysis, and (E) for plasmonic bubbles in the context of energy conversion. Obviously, all potential applications would be facilitated by a fundamental understanding of nanobubbles and nanodroplets and the ability to form and manipulate them in a controlled way and to tailor their morphology and lifetime.

A. Flotation

A large body of literature on the effects of submicron bubbles on the surface interactions was summarized by Klassen and Mokrousov (1983) and Christenson and Claesson (2001), Attard (2003), and Hampton and Nguyen (2010). The enhancement of particle-particle or particle-microbubble interactions by surface nanobubbles has great implications for dissolved gas flotation, e.g., in mineral particle separation, in waste water treatment, in oil separation, and in other separation processes (Mahnke *et al.*, 1999; Mishchuk, Ralston, and Fornasiero, 2002, 2006; Zhang, Kumar, and Scales, 2011; Calgaroto, Wilberg, and Rubio, 2014).

As proposed by Parker, Claesson, and Attard (1994) and later confirmed by Stevens *et al.* (2005) and Mastropietro and Ducker (2012), surface nanobubbles contribute to the long-range attractive interaction between two hydrophobic surfaces in water. Indeed, the hydrophobic interactions are stronger and over a longer range in the presence of dissolved gases and in fact depend on the gas type. Gong *et al.* (1999) reported that dissolved molecules adsorb on the surface of micron-sized particles, where they form submicron bubbles, facilitating the particle precipitation by buoyancy. The aggregation of hydrophobic and hydrophilic particles was related to the type of the dissolved gas; namely, the rate of aggregation of hydrophobic particles was enhanced in the presence of dissolved CO_2, but was unaffected by dissolved air, argon, or nitrogen, due to the good solubility of CO_2.

An advantage of nanobubbles as compared to macroscopic bubbles is that they may attach to much smaller particles, facilitating the separation of finer particles or finer oil droplets. To produce massive amounts of fine bubbles, Wu *et al.* (2012) designed a baffled cell and created submicron bubbles by hydrodynamic cavitation. Many potential applications of nanobubbles require the capability of initiating the growth of these nanobubbles into macroscopic bubbles. This can be achieved by massive gas oversaturation so that the stable equilibrium of the surface nanobubbles no longer exists and the gas influx due to oversaturation overwhelms the outflux due to the Laplace pressure, so that finally microbubbles developed and buoyancy lets the particles with the attached bubbles rise, or the microbubbles detach from the surface. The growth of nanobubbles may also be helped by rectified diffusion under the application of gentle ultrasound. The achievement of controlled growth of nanobubbles will be crucial for the applications of nanobubbles in flotation.

In this context we also mention the production of low density, nanocelluar polymer nanocomposite foams for isolation purposes (Chen *et al.*, 2013; Liu, Duvigneau, and Vancso, 2015) as a possible application of surface nanobubbles, created on floating hydrophobic particles. The idea is to oversaturate polymeric solutions with CO_2 to stimulate the heterogeneous nucleation of surface nanobubbles on the hydrophobic particles, and then to polymerize the solution, to obtain some foam with cell diameter of < 100 nm.

The potential technological relevance of nanobubbles for flotation of submicron particles (Scheludko, Toshev, and Bojadjiev, 1976) points toward an interesting fundamental question. What are the requirements for the formation and stability of nanobubbles on curved substrates, i.e., on nanoparticles? The curved interface induces two new elements as compared to a planar surface, namely, the curvature and the spatial confinement of the substrate. At a planar solid-water interface, the shape of nanobubbles is spherical caplike. Because of the small equilibrium contact angle θ_e the top surface (i.e., gas/water interface) of these spherical-cap-shaped nanobubbles can be almost as flat as the underneath planar substrate. On a curved surface (provided that the particle is not fully embedded into a gas bubble) the curvature of the surface nanobubble must be larger than that of the underneath substrate. Therefore, for given gas oversaturation ζ, one can expect a critical particle radius, below which it is impossible to produce nanobubbles on the particle surface. If a (small) particle is suspended in a liquid, the lateral size of the nanobubble on the particle is necessarily restricted by the total surface area of the particle. Moreover, from a certain nanobubble size on there is no space for further nanobubbles on the same particle.

B. Nanomaterial engineering

Surface nanodroplets have great potential to be used as soft 3D nanotemplates in engineering nanostructures. The advantages are that their nucleation can be triggered by chemically patterning of surfaces while their chemical composition can be controlled by the bulk solution during the droplet formation. The substrate can be planar or curved (e.g., on microparticles), as demonstrated by Ma *et al.* (2014). They first dispersed microcrystals in a microemulsion of decane nanodroplets produced by the Ouzo effect. The nanodroplets adsorbed onto the microcrystals and acted as a capping agent as the catalytic metal layer of gold or hybrid metal of gold and

platinum was deposited onto the microcrystals by galvanic reactions. The prepared porous gold layers and hybrid gold-platinum layers on copper microcrystals had enhanced efficiency in catalytic reactions, as compared to the catalytic particles without porous architectures.

Similar to nanodroplets, surface nanobubbles can also be used as soft nanotemplates. It is possible to generate a large amount of nanobubbles *in situ* by electrochemical reactions. This approach was applied in the preparation of holes in nanofilms of conductive polymers (Hui *et al.*, 2009) and in the fabrication of a large quantity of hollow gold nanoparticles (Huang *et al.*, 2009). In addition, nanobubbles at the interface between an evaporating droplet and the substrate can create nanopatterns of the materials deposited by drop evaporation. Darwich *et al.* (2011) built nanorings consisting of nanoparticles around nanobubbles by drying a drop of a nanoparticle suspension on a surface that had adsorbed nanobubbles. Berkelaar, Zandvliet, and Lohse (2013) made flower-shaped salt nanostructures by drying a drop of salt aqueous solution on a substrate with nanobubbles and/or nanodroplets in between.

An unconventional application of surface nanobubbles in nanomaterial processing is a high quality thin film transfer in a liquid environment, as shown by Gao *et al.* (2014). The aim of their work was to achieve face-to-face transfer of graphene from copper to SiO_2/Si. The schemes in Fig. 38 show the details of their graphene growth and subsequent nanobubble-faciliated transfer process: The SiO_2/Si substrate was first pretreated by plasma nitration to convert the top layer to a silicon oxynitride phase. The pretreated substrate was then coated with a copper film. By using an established technique, graphene was deposited on top of the copper film by chemical vapor deposition while some bubbles were trapped between the graphene and the copper during the deposition. The graphene/Cu/SiO_2/Si wafer was then coated with PMMA for protection. At the start of the transfer process, the entire layered material was immersed in an aqueous etching solution. The graphene-PMMA film adhered to the underlying wafer throughout the etching and transfer process. After the solution and the PMMA were removed, the transfer of graphene was completed.

In the above etching and rinsing process, it was critical that attractive interactions between the graphene-PMMA film and the substrate were strong enough to keep the film adhered to the substrate all the time. Gao *et al.* (2014) attributed the success of their transfer process to the significant capillary forces created by the trapped nanobubbles. There were two potential causes for nanobubble formation: decomposition of the silicon oxynitride phase leading to bubble nucleation and trapped bubbles from the graphene growth on copper. Without the silicon oxynitride phase from the pretreatment to induce extra nanobubbles and strong capillary forces, the films delaminated from the SiO_2 substrate—so the nanobubbles indeed were crucial.

C. Transport in nanofluidic devices and autonomous motion of nanoparticles

Classical macroscopic hydrodynamics assumes "no-slip" boundary condition at solid walls. On a microscale however this assumption can be incorrect and one has to employ the more general so-called Navier boundary conditions, by introducing a slip length $b = u_{slip}/\dot{\gamma}$, where u_{slip} is the slip velocity at the wall and $\dot{\gamma}$ is the velocity gradient at the wall in the normal direction; see, e.g., Neto *et al.* (2005), Bocquet and Charlaix (2010), and Hyväluoma, Kunert, and Harting (2011), or Rothstein (2010) for recent review articles. Clearly, the occurrence of surface nanobubbles and nanodroplets will affect the slip length. In fact, it was de Gennes (2002) who first spelled out this consequence of nanobubbles and who analyzed how a postulated thin gas film at the interface influences the slip of the liquid. When the thickness of the gas film is smaller than the mean free path of the gas, i.e., in the Knudsen regime, significant slippage can be the consequence, independent of the film thickness. The required weight fraction of the dissolved gas can be very small, on the order of 10^{-5}. We do not discuss the extensive literature on the experimental and numerical verification of this effect and simply again refer to the review articles of Neto *et al.* (2005), Bocquet and Charlaix (2010), Rothstein (2010), or Lee, Charrault, and Neto (2014). In short, gas dissolution indeed can enhance the slip on hydrophobic surfaces (which attract the gas), but the effect is much smaller than had originally been claimed by some.

To enhance the effect, an appealing idea is to nucleate nanobubbles or to create a thin layer of interfacial gas, in order to achieve massive drag reduction on the microscale and thus to allow for larger mass flux [see Feuillebois, Bazant, and

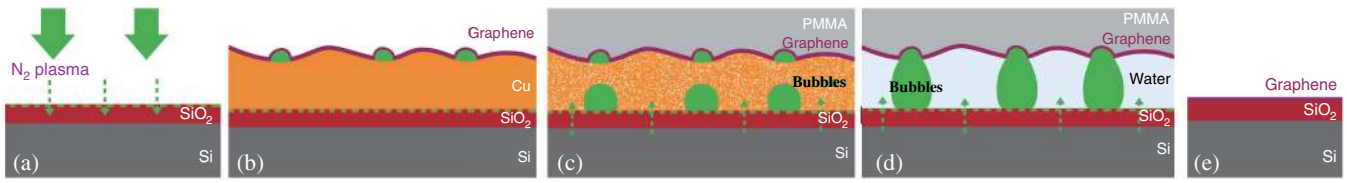

FIG. 38 (color online). Illustration of the transferring process of graphene from copper to SiO_2 facilitated by nanobubbles. (a) The supporting substrate SiO_2/Si was pretreated by nitrogen plasma to convert the top layer of SiO_2/Si to silicon oxynitride phases. (b) The substrate was coated with a copper film and then a graphene film was prepared by chemical vapor deposition onto the copper layer. Some bubbles were trapped during the graphene growth process. (c) After a layer of PMMA was coated on graphene for protection, the copper layer was dissolved in an etching solution. A silicon oxynitride phase readily decomposes, serving an additional source for nanobubbles. (d) Nanobubbles form under the graphene film. The capillary forces created by nanobubbles held the soft PMMA film and the graphene down to the hard supporting substrate. Throughout the etching process the PMMA-graphene film adhered firmly to the underlying substrate. (e) Once the solution and PMMA were washed off, the face-to-face transfer was completed. From Gao *et al.*, 2014.

Vinogradova (2009) for some upper bound estimates] or less pumping power in, e.g., lab-on-a-chip applications (Lee, Charrault, and Neto, 2014), or to further scale them down. In reality however such nanobubble applications are largely limited by the lack of an effective approach to controllably produce surface nanobubles on a large scale.

A variation of this approach is to generate nanobubbles on nanoparticles from chemical reactions and use them *in situ*. For example, in a hydrogen peroxide solution a platinum particle acts as a catalyst to make the H_2O_2 decay to water and O_2 and thus to create oxygen gas bubbles which form on the platinum particle surface. This chemical reaction can be utilized to be used as fuel to power the motion of the nanoparticle (Ismagilov *et al.*, 2002; Paxton *et al.*, 2004).

Ismagilov *et al.* (2002) reported the first self-propelled small hemicylindrical plates that move thanks to the creation of bubbles from platinum-catalyzed decomposition of hydrogen peroxide. The platinum was only at a small area on one surface of the plate, catalyzing a chemical reaction and thus converting chemical energy into autonomous movement. Since then, many groups have focused on the design of faster artificial motors on smaller scales and the study of the origin of the motor movement. Sometimes several competing propulsion mechanisms were proposed for one type of nanomotor (Guix, Mayorga-Martinez, and Merkoci, 2014): In the self-diffusiophoresis mechanism, the motion of the nanostructures is caused by the local concentration gradient of the dissolved oxygen produced during the catalytic reaction. In the bubble release mechanism, the growth, burst, and detachment of oxygen bubbles are responsible for the propulsion of the motors (Guix, Mayorga-Martinez, and Merkoci, 2014).

Another example is the work by Paxton *et al.* (2004) who employed catalytically generated nanobubbles to design a self-propelled nanorod, consisting of a so-called Janus particle, with one side composed of gold and the other side of platinum. When put in a H_2O_2 solution, on the Pt side catalytically generated oxygen nanobubbles emerged, leading to different hydrodynamic boundary conditions on the Pt side (more slip) as compared to the Au side (no slip). The rod then self-propelled thanks to the chemical potential gradient, with a directional motion due to the asymmetry of the boundary conditions. Manjare, Yang, and Zhao (2012) found the motion of such type of micromotor to coincide with the growth and burst of bubbles on the particle surface. Solovev *et al.* (2009) constructed tubular microjet engines that are propelled by gas bubbles ejected from one opening of the end. The velocity of engines can be up to 2 mm/s, subject to the influence of the bubble size and the bubble generation frequency.

Wilson, Nolte, and van Hest (2012) built highly sophisticated smart polymer stomatocytes that were bowl-shaped nanostructures with strictly controlled opening sizes, as shown in Fig. 39. Catalytic platinum nanoparticles were trapped inside the cavity of the stomatocytes, where hydrogen peroxide was decomposed to oxygen and water. The rapid expulsion of the produced oxygen led to the autonomous movement of the stomatocytes. The opening of the stomatocytes controlled the direction of the movement; however, the bubbles were not directly observed due to the small size of the stomatocyte.

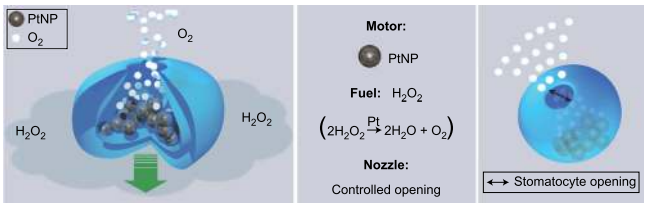

FIG. 39 (color online). Structure of a nanomotor that has the shape of a stomatcyte. Left panel: The polymer stomatocytes entrap catalytical platinum nanoparticles inside the cavity. The autonomous movement of stomatocytes is controlled by adding the appropriate fuel (hydrogen peroxide). The oxygen bubbles from the decomposition of hydrogen peroxide are expelled from the cavity and the direction of the stomatocytes (arrow) is away from its opening. Side view of the system. Middle panel: Analogy with a miniature propellant. Right panel: View of the opening of the stomatocyte. From Wilson, Nolte, and van Hest, 2012.

A rather different type of nanobubble-enhanced transport phenomenon in nanofluidic devices and in porous media was suggested by Lee, Laoui, and Karnik (2014) who used hydrophobic patches to trigger nanobubble formation in nanochannels and revealed the molecular mechanism of the water transport through them; see also the discussion of this work by Bocquet (2014). The liquid and gas interfaces of the nanobubbles act as barriers for nonvolatile substances in the transport and separation processes through the membranes: Water molecules can pass through the nanobubble obstacles by evaporation and subsequent condensation, while nonvolatile substances cannot, as shown in Fig. 40. This mechanism was demonstrated by the separation of ions from water and the separation of dye from water as shown in Fig. 40. The experiments of Lee, Laoui, and Karnik (2014) showed that

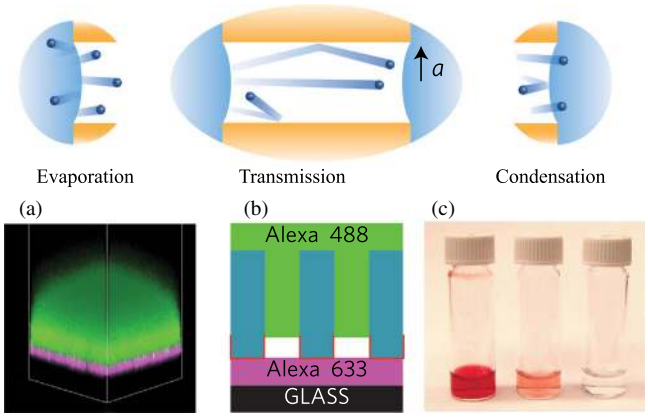

FIG. 40 (color online). Osmosis membranes with nanoscale vapor traps. Top: The schematic illustration shows the vapor transport process in the osmosis membrane. Bottom: (a) The confocal microscopy image shows the clear interface between two different fluorescence dye solutions (Alexa 633 and Alexa 488 in water). (b) The schematic drawing shows the vapor bubbles separating the two dye solutions in the osmosis membrane. (c) Demonstration of the vapor phase transport. Right: Initial dye solution. Middle: Mimicking how the solution would look if water was transported without dye rejection. Left: Actually solution with the vapor phase transport process showing dye rejection. From Lee, Laoui, and Karnik, 2014.

the mass transport in the membrane was limited by the molecular bouncing on the gas and liquid interface of the nanobubbles. The process depended on the transmission probability of water molecules across the nanobubbles and on the condensation probability of water molecules on the liquid surface. In related work Guillemot *et al.* (2012) used highly ordered hydrophobic nanopores with radii of a few nanometers to reveal the dynamics of water evaporation in hydrophobic confinement. Water was forced into the pores at high pressure, and then became metastable and at a reduced pressure finally evaporated, also leading to transport phenomena.

D. Catalysis and electrolysis

In catalytic and electrolytic reactions, gas develops at surfaces which due to the emerging gas oversaturation can lead to gas bubbles attached to the catalyst or the electrode. Various such processes have tremendous relevance for applications, e.g., the chlorine production, electrochemical or photovoltaic photolysis of water in the context of solar energy (Fujishima and Honda, 1972; Luo *et al.*, 2014), photocatalysis, biomass catalysis (Zakzeski *et al.*, 2010), or syngas catalysis for solar fuels production (Steinfeld, 2005). Further cases of bubble formation in electrochemical reactions and their technological relevance is described in Westerheide and Westwater (1961), Ammam (2012), Ahn *et al.* (2013), and Hammadi, Morin, and Olives (2013). The emerging microbubbles and nanobubbles attached to the electrode or catalyst block the direct contact to the liquid phase and thus reduce further electrochemical or electrolytical reactions. In fact, it even had been reported that bubbles collapse close to catalytic surfaces, destroying them by cavitation damage (Suslick and Price, 1999). Nonetheless, remarkably, the bubble dynamics on electrodes and catalysts is not well studied. Some exceptions from an applied point of view are Vogt and Balzer (2005) and Zhang and Zeng (2012) and from a fundamental point of view the papers mentioned in Sec. II.E on nanobubble creation by electrolysis. From an application point of view however this issue is extremely relevant, and we expect major improvements in catalytic or electrochemical process efficiency when the emerging bubbles can be easily removed, e.g., ultrasonically or by surface coating, or when their formation can be suppressed or reduced.

E. Plasmonic bubbles and vapor nanobubbles

Metallic nanostructures can quickly and strongly heat, thanks to plasmonic resonances, which can be excited by a resonant laser (Halas *et al.*, 2011). The plasmonic metal nanoparticles thus convert optical energy into highly localized heat and act as a nanoscopic heat source that overheats the adjacent liquid, leading to a phase transition and the creation of vapor bubbles, termed plasmonic nanobubbles (Lukianova-Hleb *et al.*, 2010). In contrast to the stable surface nanobubbles, the vapor nanobubbles are very transient, growing or shrinking with or without further illumination. The local high temperature that can be reached from the plasmonic heating may have a wide range of applications.

Plasmonic nanobubbles can also be used to enhance catalytic reactions. Adleman *et al.* (2009) developed the so-called plasmon-assisted catalysis technique in which catalytic gold nanoparticles (of 20 nm diameter) were immobilized on a glass substrate inside a microchannel. The microchannel was then filled with water. Under illumination with a low-intensity laser with a wavelength coinciding with the resonant frequency of the nanoparticles steady microbubbles formed. Adleman *et al.* (2009) also suggested that the dissolved gas may facilitate the vapor bubble formation.

Adleman *et al.* (2009) then demonstrated that the plasmonic heating was indeed enough to drive catalytic reactions. In their experiments the reactant solution of ethanol and water with a 1 : 1 ratio flew over the catalyst particles. Continuous bubbles formed under the illumination. The products of the reaction, CO_2, CO, and H_2, were detected in the flow, consistent with catalytic decomposition of ethanol. Unlike a typical reactor in which the entire system is held for a considerable time at the process temperature, which is at least above the boiling point of the reactants, the entire system could be kept at room temperature. Plasmonic heating of the nanoparticles thus provided not only the heat for the reaction, but also the means to generate both water and ethanol vapor locally over the catalysts, which in turn allowed for the chip and the liquid to remain at room temperature.

The nanoscale dynamics of the plasmonic nanobubble formation has not yet been fully understood. A model system is the nanobubble nucleation on a single isolated nanoparticle immobilized on a substrate. Experimental measurements show that the liquid can be overheated significantly until the nucleation of nanobubles. Fang *et al.* (2013) investigated the liquid-vapor phase transition, temperature, and bubble size during the initial formation of the vapor shell around the nanoparticle. Their measurements combined dark-field scattering with surface-enhanced Raman scattering. The dark-field scattering revealed the bubbles, while the Raman spectrum reflected the temperature. It was found that the steam envelop formation leads to a dramatic temperature jump. The quantitative analysis revealed that the temperature for the nanobubble formation was up to 460 K, well above the boiling point of water at ambient conditions. Such high temperatures are not surprising, given the absence of nucleation sites (Apfel, 1970). As the nanoparticles were more densely distributed, nanobubbles from neighboring nanoparticles coalesce and form microbubbles. Carlson, Green, and Richardson (2012) observed that the temperature of water surrounding the nanodot on temperature-dependent photoluminescent thin film can reach about 590 K. In that case nanoparticles themselves did not act as nucleation sites for the bubble formation.

On a regular and uniform array of spherical plasmonic gold nanoparticles on a glass coverslip, Baffou *et al.* (2014) produced microbubbles around the particles under continuous illumination. They also found that the local temperature for the bubble formation was much larger than the water boiling point, and it was evident that water was overheated prior to bubble nucleation. The lifetime of these bubbles was observed to be as long as several minutes. To account for the long lifetime of the bubbles, Baffou *et al.* (2014) proposed that the dissolved gas in the liquid plays an important role in the

growth and stability of the light-induced microbubbles, namely, that the bubbles did not consist of water steam but mainly of air (and of course some water steam). Otherwise one would expect the emerging vapor bubble to collapse and condense immediately once it comes into contact with the cold liquid.

Ongoing research issues in this context are the fabrication of highly effective nanoparticles, the durability of nanoparticles, and the mechanisms of nanoscale nucleation and enhanced (photo)catalytic reactions (Boulais, Lachaine, and Meunier, 2012; Carlson, Green, and Richardson, 2012; Cavicchi *et al.*, 2013; Polman, 2013). In particular, the plasmon enhanced solar to fuel conversion is extremely attractive (Thomann *et al.*, 2011). A full theoretical understanding of the bubble nucleation and dynamics will clearly facilitate the design of more efficient energy conversion processes.

VIII. SUMMARY, PREDICTIONS, AND OPEN ISSUES FOR FUTURE RESEARCH

A. Our view on surface nanobubbles and nanodroplets in a nutshell

If one fills a glass with cold fresh tap water (which is considerably air oversatured) and lets the glass stand for some hours at room temperature, one will find many gas bubbles at the glass wall; see Fig. 41. As the water warms up from the surrounding air (at room temperature) during the experiment, the air oversaturation further locally increases which finally leads to bubble nucleation at the wall. The effect is even stronger in a polyethylene terephthalate (PET) plastic bottle, due to its more hydrophobic surface, on which gas bubbles like to nucleate. In comparison to the heat diffusivity, the mass diffusivity of the dissolved gas is 3 orders of magnitude slower and the oversaturation in the water thus persists. Even after days the air bubbles are still present in the water-filled glass exposed to the atmosphere, and in the closed PET plastic bottle they survive for weeks.

FIG. 41 (color online). Glass filled with cold tap water (which is air oversaturated) after 24 h under room temperature conditions: Many surface bubbles have nucleated and survived.

In another daily life experiment water is poured into a glass filled with clear Ouzo (Anis oil dissolved in an ethanol-water mixture). The addition of water reduces the oil solubility, leading to droplet nucleation in the bulk (emulsification) and even more on immersed hydrophobic surfaces, on which the oil droplets like to nucleate. This method is completely analogous to the most popular way to create surface nanobubbles, namely, by ethanol-water exchange: Here it is the air solubility which is much lower in water than in ethanol (or ethanol-water mixtures with a high ethanol percentage).

Indeed, the formation and long persistence of surface nanobubbles or nanodroplets is not so different from above daily life processes, apart from the smaller length scales, which are in the above sketched experiments normally not detected. How the gas or oil oversaturation is created is not so relevant and there are various ways from warming up saturated water to ethanol-water exchange to electrolysis to catalytic reactions: Once some local oversaturation is achieved close to some hydrophobic surface, it will inevitably lead to nucleation of the species in abundance, be it gas or a dissolved liquid such as oil.

Not only are the methods to create immersed surface nanobubbles and nanodroplets the same, namely, by ethanol-water exchange, but also the dynamical equations describing them, namely, the diffusion equation with the corresponding boundary conditions, which are the imposed concentration c_∞ far away from the bubble or droplet and the gas concentration following from Henry's law (with the Laplace pressure considered) at the bubble-water interface and the liquid saturation concentration at the droplet-water interface. In fact, these equations even describe the evaporation of a droplet in air, as long as the process is diffusion limited.

What also is the same for both surface nanobubbles and nanodroplets is that the pinning of the three-phase contact line at geometric and chemical surface heterogeneities is essential, leading to stabilization. Thanks to the pinning, the pressure inside the surface bubble does not diverge once the bubble is shrinking (as it does for a bubble in the bulk, pressing out the gas into the water), but decreases.

For gas oversaturation and small enough surface bubbles, thanks to the pinning a stable equilibrium can emerge, at which the influx into the bubble due to the oversaturation is balanced by the outflux due to the Laplace pressure. There thus indeed is a (gas concentration dependent) difference between surface nanobubbles as compared to surface microbubbles: For the latter the Laplace pressure is not large enough to be able to counteract the gas influx due to oversatuation. It is this equilibrium between gas influx due to oversaturation and gas outflux due to the Laplace pressure which sets the equilibrium contact angle θ_e of the nanobubble, which has nothing to do with the macroscopic contact angle, given by Young's equation with the involved surface tensions. So the two most prominent "paradoxes" of surface nanobubbles, namely, their long lifetime and their low contact angle, are both naturally accounted for by contact line pinning, resulting from surface heterogeneities, just as the omnipresent contact angle hysteresis.

In (gas or liquid) undersaturated water, the type of mode in which the bubble or drop is shrinking can be mixed, with the CA mode (constant angle) and the CR mode (constant contact radius, i.e., constant footprint) as extreme cases, but in general with a stick-slide or stick-jump mode, in which the contact radius can slide or jump to smaller values, depending on the local geometric and chemical surface heterogeneities. As these features differ for the various surface nanobubbles and nanodroplets, they obtain a kind of "individuality": Each one can behave differently. This individuality is also helped by collective effects between the surface nanobubbles and nanodroplets, as in general each one is surrounded by others which affect the concentration field.

The surface heterogeneities are crucial for the surface nanobubble and nanodroplet stabilization. They are omnipresent and nearly unavoidable. Therefore, they are not a bug of the system, but a feature. Chemical surface heterogeneities can be either air bound prior to immersion or water bound and will in general be hydrophobic so that both dissolved gases and dissolved oils will nucleated at them, leading to surface nanobubbles and nanodroplets. Another consequence of the surface inhomogeneities is the omnipresent contact angle hysteresis, which is well known and was well studied by de Gennes and co-workers in the 1980s and 1990s. So contact angle hysteresis and the formation of long-living surface nanobubbles and nanodroplets go hand in hand. The new element here is that the surface nanobubbles and nanodroplets have submicron lateral scale and are thus better suited to probe the microscopic surface heterogeneities.

Two time scales govern the surface nanobubble and nanodroplet dynamics: First, the local time scale for the diffusion around an individual bubble or droplet, $\tau_{\text{inner}} = L^2\rho_{g,l}/(4Dc_s)$, which is given by the material parameters, in particular, the solubility; see Table II. For gases or liquids with low solubility (e.g., air or decane), this local time scale can be rather slow. In order to perform experiments which probe and study the local diffusive dynamics of the surface nanobubbles and nanodroplets (shrinkage, dissolution, Ostwald ripening, etc.), gases and liquids with appropriate local time scale must be chosen. The second relevant time scale for surface nanobubbles and nanodroplets is the one which controls the oversaturation ζ. For closed systems $\tau_{\text{outer}} = \infty$. For open systems with a distance ℓ to the outer world it is the diffusive time scale $\tau_{\text{outer}} = \ell^2/D$, which in general is orders of magnitude larger than τ_{inner}.

B. Predictions and open issues for future research

Of course, the above sketched view on surface nanobubbles and nanodroplets should quantitatively be tested against further experiments. In this last section we suggest various such experiments and will make predictions on their outcome, in order to verify our view and to supplement it—or to falsify it.

First, if one wants to experimentally probe the diffusive dynamics in open systems, it would be helpful to perform experiments with individual (i.e., noninteracting and isolated) bubbles or drops (e.g., obtained by surface patterning, see below), which will not have an enhanced lifetime by collective effects. If the density of surface nanobubbles or nanodroplets is larger or smaller, their lifetime is longer or smaller, and in open systems they are a transient phenomenon. Trying to understand them from individual AFM "snapshots" is comparable to the attempt to understand Newtonian dynamics from a snapshot of a stone thrown into the air. In fact, in any surface nanobubble experiment, the nanobubble dissolution in degassed water should be a standard test, to avoid confusion surface nanobubbles with long-living surface nanodroplets of some poorly soluble liquid contamination. Note that gas condensates (with a thickness of one molecular layer) on the surface can survive the degassing procedure as they are chemically bound.

These experiments must be performed under controlled conditions. The field must aim at getting a fully reproducible protocol of surface nanobubble generation and characterize and quantify the fluid dynamical and thermodynamical conditions of the surface nanobubble generating an ethanol-water exchange process in detail. Presently, most flow cells in which this process takes place are neither fully closed, nor fully open, nor are there free boundary conditions with a well-defined pool depth ℓ. This makes it nearly impossible to have controlled boundary conditions on the gas concentration field and thus a well-controlled oversaturation ζ. In addition, open cells facilitate all kinds of contaminations and imply evaporation of the water, changing the conditions over time.

The lack of controlled conditions will thus complicate long-term dynamical experiments, which are however essential to probe our view: The surface nanobubble (and nanodroplet) formation and dissolution should be quantitatively analyzed. For nanobubbles, a possible way out may be closed and pressure controlled devices as that of Enriquez *et al.* (2013), with which controlled gas oversaturations ζ can be achieved. With such devices in principle the equilibrium contact angle $\theta_e(\zeta)$ and the equilibrium radius of curvature $R_e(\zeta)$ and their dependences on ζ can be measured and compared to theory, although presently such devices are not accessible for AFM measurements.

As compared to gases, for liquids, there is a larger variability of solubility, leading to adjustable inner time scales with many orders of magnitude differences. The advantage of surface nanodroplets as compared to surface nanobubbles in addition is that it is much easier to control the liquid concentration in water, rather than the gas concentration, and that (at least for nonvolatile liquids) the interaction with the surrounding world is easier to control.

As stated previously, pinning caused by chemical and geometric surface heterogeneities is an essential feature for the stability of surface nanobubbles and nanodroplets. Therefore, efforts should be undertaken to control them, both their—preferably very high—hydrophobicity, their shape, their lateral extension, and their spacing. This is meanwhile possible through chemically prepatterning surfaces on a microscale and nanoscale, thus offering the system weak spots on which the surface nanobubbles and nanodroplets will nucleate, similar to introducing controlled air-filled microcrevices and nanocrevices as weak spots in the study of cavitation bubbles (Bremond *et al.*, 2006; Borkent, Gekle *et al.*, 2009) or in boiling studies (Phan *et al.*, 2009; Patankar, 2010). The surface nanobubbles and nanodroplets which nucleate on the prepatterned hydrophobic patches offer the

opportunity to directly study the pinning and depinning behavior of the surface nanobubbles and nanodroplets and their long-term diffusive dynamics. This holds for individual surface nanobubbles and nanodroplets nucleated on individual patches of various geometric shapes and sizes, but also for their collective behavior, in order to study their cross talk, Ostwald ripening, and other collective effects for a controlled spatial distribution imposed by the micropatterning and nanopatterning.

For these controlled nucleation and dissolution experiments on chemically prepatterned surfaces, direct optical observations (including confocal microscopy) is easiest, but is restricted to features larger than a few hundred nanometers. Nonetheless, we think that such experiments are extremely worthwhile. However, chemically micropatterning and nanopatterning surfaces with strongly hydrophobic patches will also ease AFM measurements on surface nanobubbles and nanodroplets, as (i) the bubble and droplet nucleation and dissolution will be more reproducible and as (ii) their positions are *a priori* known. Studying the nucleation, growth, and dissolution dynamics of surface nanobubbles and nanodroplets will shed new light on the problems of contact line pinning and contact angle hysteresis on the submicron scale. The exact chemical and geometric properties of the surface but also the flow conditions and the concentrations will all be relevant here.

Although on solid surfaces heterogeneities are nearly unavoidable, the situation may be more controlled on liquid surfaces, at least with respect to the geometric heterogeneities as for a liquid the surface is perfectly smooth, but for hydrophobic liquids inmiscible with water (and ethanol) presumably also with respect to the chemical heterogeneities. We suggest to perform the ethanol-water exchange process on (or under, in case that it is lighter than water) such a liquid, rather than on a solid surface. Because of the surface homogeneity and thus absence of pinning we expect a strongly reduced lifetime of the surface bubbles and droplets on such liquid surfaces as compared to those on solid surfaces—it may be difficult to observe them at all. If they form, it will again be interesting to observe their diffusive dynamics, but also to see how the capillary forces at the three-phase contact line deform the interface. Such interface deformation is expected and has been observed in the context of wetting of soft substrates (Weijs, Andreotti, and Snoeijer, 2013) and it may lead to self-pinning of the bubble or droplet.

Surfaces with properties similar to liquid surfaces (i.e., perfectly smooth), but on which it may be easier to perform AFM imaging, are self-repairing slippery surfaces with pressure-stable omniphobicity, as developed and employed by Wong *et al.* (2011), Kim *et al.* (2012), and Daniel *et al.* (2013). Here some organic lubricants sit on rough structures, giving perfect smoothness. Correspondingly, also on such surfaces we do not expect long-living surface nanobubbles.

The prime experimental technique for surface nanobubbles has hitherto been AFM, due to the good spatial resolution. But AFM is blind, slow, and intrusive. To make further progress it will have to be augmented by further techniques, many of which we discussed in Sec. III. Here we want to stress again the potential of combining AFM with local optical techniques for single surface nanobubbles, such as time-resolved tip-enhanced Raman spectroscopy, integrated AFM-Raman instruments, or correlated single photon counting combined with FLIM, all of which overcome the blindness of AFM.

At the end of this review we come back to one of the original motivations to postulate the existence of nanobubbles, namely, to account for the experimentally observed so-called hydrophobic attraction (Parker, Claesson, and Attard, 1994; Considine and Drummond, 2000; Stevens *et al.*, 2005). While for the case of Fig. 3 the nanobubbles are indeed likely the origin of the enhanced attraction, they do not offer a general solution to the question of the so-called hydrophobic attraction (Stevens *et al.*, 2005). However, for each individual case the role of the nanobubbles can simply be tested, namely, by (partially) degassing the liquid for a sufficiently long time (so that the local oversaturation ζ at the wall is smaller than zero) and then study the situation again: Any possible effects by the nanobubbles will be gone. Indeed, Stevens *et al.* (2005) and Mastropietro and Ducker (2012) found strongly reduced hydrophobic attraction by degassing.

Finally, next to the analytical calculations for the diffusive processes around single surface bubbles and droplets (Sec. VI.D), also numerical simulations for controlled populations of nanobubbles and nanodroplets are necessary, by numerically solving the diffusion equations with the respective boundary conditions. Next to direct finite difference simulations of the continuum equations and MD simulations, also lattice-Boltzmann simulations may be useful. Theoretical and numerical effort should, in particular, explore the role of the disjoining pressure and its detailed effect on the bubble shape, its inside pressure, and thus its equilibrium contact angle. In any case, we are optimistic that at least for surface microdroplets and nanodroplets and for the controlled conditions of chemically prepatterned surfaces soon the field will achieve a favorable one-to-one comparison between experiment, theory, and numerical simulations.

ACKNOWLEDGMENTS

We thank all of our co-workers and colleagues for their contributions to our understanding of this great problem, for the many stimulating discussions we had the privilege to enjoy with them over the years, and for their many valuable comments on this manuscript. D. L. acknowledges continuous support from FOM and STW, both of which are part of The Netherlands Organisation for Scientific Research (NWO), from ERC via an Advanced Grant, and from the NWO Zwartekracht MCEC program. X. H. Z. acknowledges continuous support from the Australian Research Council through ARC Fellowships (No. DP0880152 and No. FFT120100473) and Discovery Project (No. DP140100805) and support from the NWO Zwartekracht MCEC program.

REFERENCES

Adleman, J. R., D. A. Boyd, D. G. Goodwin, and D. Psaltis, 2009, "Heterogenous Catalysis Mediated by Plasmon Heating," Nano Lett. **9**, 4417.

Afkhami, S., and L. Kondic, 2013, "Numerical Simulation of Ejected Molten Metal Nanoparticles Liquified by Laser Irradiation: Interplay of Geometry and Dewetting," Phys. Rev. Lett. **111**, 034501.

Agrawal, A., J. Park, D. Y. Ryu, P. T. Hammond, T. P. Russell, and G. H. McKinley, 2005, "Controlling the location and spatial extent of nanobubbles using hydrophobically nanopatterned surfaces," Nano Lett. **5**, 1751.

Ahn, S. H., *et al.*, 2013, "Effect of morphology of electrodeposited Ni catalysts on the behavior of bubbles generated during the oxygen evolution reaction in alkaline water electrolysis," Chem. Commun. (Cambridge) **49**, 9323.

Ajaev, V. S., 2006, "Effect of nanoscale bubbles on viscous flow and rupture in thin liquid films," Phys. Fluids **18**, 068101.

Ajaev, V. S., E. Y. Gatapova, and O. A. Kabov, 2011, "Rupture of thin liquid films on structured surfaces," Phys. Rev. E **84**, 041606.

Ammam, M., 2012, "Electrophoretic deposition under modulated electric fields: a review," R. Soc. Chem. Adv. **2**, 7633.

An, H., G. Liu, and V. S. Craig, 2015, "Wetting of nanophases: Nanobubbles, nanodroplets and micropancakes on hydrophobic surfaces," Adv. Colloid Interface Sci. **222**, 9.

Apfel, R. E., 1970, "The Role of Impurities in Cavitation Threshold Determination,"
J. Acoust. Soc. Am. **48**, 1179.

Aschenbrenner, E., K. Bley, K. Koynov, M. Makowski, M. Kappl, K. Landfester, and C. K. Weiss, 2013, "Using the Polymeric Ouzo Effect for the Preparation of Polysaccharide-Based Nanoparticles," Langmuir **29**, 8845.

Atchley, A. A., and A. Prosperetti, 1989, "The crevice model of bubble nucleation," J. Acoust. Soc. Am. **86**, 1065.

Attard, P., M. P. Moody, and J. W. G. Tyrrell, 2002, "Nanobubbles: the big picture," Physica A (Amsterdam) **314**, 696.

Attard, P., 2003, "Nanobubbles and the hydrophobic attraction," Adv. Colloid Interface Sci. **104**, 75.

Aubry, J., F. Ganachaud, J.-P. C. Addad, and B. Cabane, 2009, "Nanoprecipitation of Polymethylmethacrylate by Solvent Shifting: 1. Boundaries," Langmuir **25**, 1970.

Baffou, G., J. Polleux, H. Rigneault, and S. Monneret, 2014, "Super-Heating and Micro-Bubble Generation around Plasmonic Nanoparticles under cw Illumination," J. Phys. Chem. C **118**, 4890.

Bain, C. D., and G. M. Whitesides, 1988, "Formation of two-component surfaces by the spontaneous assembly of monolayers on gold from solutions containing mixtures of organic thiols," J. Am. Chem. Soc. **110**, 6560.

Ball, P., 2003, "How to keep dry in water," Nature (London) **423**, 25.

Banwell, C. N., 1983, *Fundamentals of molecular spectroscopy* (McGraw-Hill, London).

Barnes, G., 1986, "The effects of monolayers on the evaporation of liquids," Adv. Colloid Interface Sci. **25**, 89.

Battino, R., P. G. Seybold, and F. C. Campanell, 2011, "Correlations Involving the Solubility of Gases in Water at 298.15 K and 101325 Pa," J. Chem. Eng. Data **56**, 727.

Bauer, C., and S. Dietrich, 1999, "Quantitative study of laterally inhomogeneous wetting films," Eur. Phys. J. B **10**, 767.

Belova, V., D. A. Gorin, D. G. Shchukin, and H. Moehwald, 2010, "Selective Ultrasonic Cavitation on Patterned Hydrophobic Surfaces," Angew. Chem., Int. Ed. Engl. **49**, 7129.

Belova, V., M. Krasowska, D. Wang, J. Ralston, D. G. Shchukin, and H. Moehwald, 2013, "Influence of adsorbed gas at liquid/solid interfaces on heterogeneous cavitation," Chem. Sci. **4**, 248.

Belova, V., D. G. Shchukin, D. A. Gorin, A. Kopyshev, and H. Moehwald, 2011, "A new approach to nucleation of cavitation bubbles at chemically modified surfaces," Phys. Chem. Chem. Phys. **13**, 8015.

Berendsen, H., J. Postma, W. van Gunsteren, A. Dinola, and J. Haak, 1984, "Molecular-Dynamics with coupling to an external bath," J. Chem. Phys. **81**, 3684.

Berkelaar, R. P., P. Bampoulis, E. Dietrich, H. P. Jansen, X. Zhang, E. S. Kooij, D. Lohse, and H. J. W. Zandvliet, 2015, "Water-induced blister formation in a thin film polymer," Langmuir **31**, 1017.

Berkelaar, R. P., E. Dietrich, G. A. M. Kip, E. S. Kooij, H. J. W. Zandvliet, and D. Lohse, 2014, "Exposing nanobubble-like objects to a degassed environment," Soft Matter **10**, 4947.

Berkelaar, R. P., J. R. T. Seddon, H. J. W. Zandvliet, and D. Lohse, 2012, "Temperature Dependence of Surface Nanobubbles," ChemPhysChem **13**, 2213.

Berkelaar, R. P., H. J. W. Zandvliet, and D. Lohse, 2013, "Covering surface nanobubbles with a NaCl nanoblanket," Langmuir **29**, 11 337.

Bhushan, B., Y. Wang, and A. Maali, 2008, "Coalescence and movement of nanobubbles studied with tapping mode AFM and tip-bubble interaction analysis," J. Phys. Condens. Matter **20**, 485004.

Biggs, S., and F. Grieser, 1994, "Atomic-force microscopy imaging of thin-films formed by hydrophobing reagents," J. Colloid Interface Sci. **165**, 425.

Binnig, G., C. F. Quate, and C. Gerber, 1986, "Atomic Force Spectroscopy," Phys. Rev. Lett. **56**, 930.

Bocquet, L., 2014, "Bubbles as osmotic membranes," Nat. Nanotechnol. **9**, 249.

Bocquet, L., and E. Charlaix, 2010, "Nanofluidics, from bulk to interfaces," Chem. Soc. Rev. **39**, 1073.

Bonn, D., J. Eggers, J. Indekeu, J. Meunier, and E. Rolley, 2009, "Wetting and spreading," Rev. Mod. Phys. **81**, 739.

Borkent, B. M., S. M. Dammer, H. Schönherr, G. J. Vancso, and D. Lohse, 2007, "Superstability of Surface Nanobubbles," Phys. Rev. Lett. **98**, 204502.

Borkent, B. M., S. de Beer, F. Mugele, and D. Lohse, 2010, "On the shape of surface nanobubbles," Langmuir **26**, 260.

Borkent, B. M., S. Gekle, A. Prosperetti, and D. Lohse, 2009, "Nucleation threshold and deactivation mechanisms of nanoscopic cavitation nuclei," Phys. Fluids **21**, 102003.

Borkent, B. M., H. Schönherr, G. L. Caër, B. Dollet, and D. Lohse, 2009, "Preferred sizes and ordering in surface nanobubble populations," Phys. Rev. E **80**, 036315.

Boruvka, L., and A. Neumann, 1977, "Generalization of the classical theory of capillarity," J. Chem. Phys. **66**, 5464.

Boulais, E., R. Lachaine, and M. Meunier, 2012, "Plasma Mediated off-Resonance Plasmonic Enhanced Ultrafast Laser-Induced Nanocavitation," Nano Lett. **12**, 4763.

Bouwhuis, W., R. C. A. van der Veen, T. Tran, D. L. Keij, K. G. Winkels, I. R. Peters, D. van der Meer, C. Sun, J. H. Snoeijer, and D. Lohse, 2012, "Maximal Air Bubble Entrainment at Liquid-Drop Impact," Phys. Rev. Lett. **109**, 264501.

Bratko, D., and A. Luzar, 2008, "Attractive surface force in the presence of dissolved gas: A molecular approach," Langmuir **24**, 1247.

Bremond, N., M. Arora, C.-D. Ohl, and D. Lohse, 2006, "Controlled Multibubble Surface Cavitation," Phys. Rev. Lett. **96**, 224501.

Brennen, C. E., 1995, *Cavitation and Bubble Dynamics* (Oxford University Press, Oxford).

Brenner, M. P., S. Hilgenfeldt, and D. Lohse, 2002, "Single bubble sonoluminescence," Rev. Mod. Phys. **74**, 425.

Brenner, M. P., and D. Lohse, 2008, "Dynamic Equilibrium Mechanism for Surface Nanobubble Stabilization," Phys. Rev. Lett. **101**, 214505.

Brotchie, A., and X. H. Zhang, 2011, "Response of interfacial nanobubbles to ultrasound irradiation," Soft Matter **7**, 265.

Brunauer, S., P. H. Emmet, and E. Teller, 1938, "Adsorption of gases in multimolecular layers," J. Am. Chem. Soc. **60**, 309.

Burg, T. P., M. Godin, S. M. Knudsen, W. Shen, G. Carlson, J. S. Foster, K. Babcock, and S. R. Manalis, 2007, "Weighing of biomolecules, single cells and single nanoparticles in fluid," Nature (London) **446**, 1066.

Burns, P., 1996, "Harmonic imaging with ultrasound contrast agents," Clin. Radiol. **51**, 50.

Bussi, G., D. Donadio, and M. Parrinello, 2007, "Canonical sampling through velocity rescaling," J. Chem. Phys. **126**, 014101.

Butler, J. A. V., 1932, "The thermodynamics of the surfaces of solutions," Proc. R. Soc. A **135**, 348.

Butt, H., B. Cappella, and M. Kappl, 2005, "Force measurements with the atomic force microscope: Technique, interpretation and applications," Surf. Sci. Rep. **59**, 1.

Calgaroto, S., K. Q. Wilberg, and J. Rubio, 2014, "On the nanobubbles interfacial properties and future applications in flotation," Miner. Eng. **60**, 33.

Cappella, B., and G. Dietler, 1999, "Force-distance curves by atomic force microscopy," Surf. Sci. Rep. **34**, 1.

Carambassis, A., L. C. Jonker, P. Attard, and M. W. Rutland, 1998, "Forces Measured between Hydrophobic Surfaces due to a Submicroscopic Bridging Bubble," Phys. Rev. Lett. **80**, 5357.

Carlson, M. T., A. J. Green, and H. H. Richardson, 2012, "Superheating Water by CW Excitation of Gold Nanodots," Nano Lett. **12**, 1534.

Carr, M. W., A. R. Hillman, S. D. Lubetkin, and M. J. Swann, 1989, "Detection of electrolytically generated bubbles using an electrochemical quartz crystal microbalance," J. Electroanal. Chem. **267**, 313.

Cavicchi, R. E., D. C. Meier, C. Presser, V. M. Prabhu, and S. Guha, 2013, "Single Laser Pulse Effects on Suspended-Au-Nanoparticle Size Distributions and Morphology," J. Phys. Chem. C **117**, 10 866.

Cazabat, A. M., and G. Guéna, 2010, "Evaporation of macroscopic sessile droplets," Soft Matter **6**, 2591.

Chan, C. C., and C.-D. Ohl, 2012, "Total-Internal-Reflection-Fluorescence Microscopy for the Study of Nanobubble Dynamics," Phys. Rev. Lett. **109**, 174501.

Chan, C. U., L. Chen, M. Arora, and C.-D. Ohl, 2015, "Collapse of Surface Nanobubbles," Phys. Rev. Lett. **114**, 114505.

Chen, H., H. Mao, L. Wu, J. Zhang, Y. Dong, Z. Wu, and J. Hu, 2009, "Defouling and cleaning using nanobubbles on stainless steel," Biofouling **25**, 353.

Chen, L., D. Rende, L. S. Schadler, and R. Ozisik, 2013, "Polymer nanocomposite foams," J. Mater. Chem. A **1**, 3837.

Chen, Q., L. Luo, H. Faraji, S. W. Feldberg, and H. S. White, 2014, "Electrochemical Measurements of Single H2 Nanobubble Nucleation and Stability at Pt Nanoelectrodes," J. Phys. Chem. Lett. **5**, 3539.

Chen, Q., L. Luo, and H. S. White, 2015, "Electrochemical Generation of a Hydrogen Bubble at a Recessed Platinum Nanopore Electrode," Langmuir **31**, 4573.

Chen, S., and G. D. Doolen, 1998, "Lattice Boltzmann methods for fluid flows," Annu. Rev. Fluid Mech. **30**, 329.

Christenson, H. K., and P. M. Claesson, 2001, "Direct measurements of the force between hydrophobic surfaces in water," Adv. Colloid Interface Sci. **91**, 391.

Connell, S., S. Allen, C. Roberts, J. Davies, M. Davies, S. Tendler, and P. Williams, 2002, "Investigating the interfacial properties of single-liquid nanodroplets by atomic force microscopy," Langmuir **18**, 1719.

Considine, R. F., and C. J. Drummond, 2000, "Long-Range Force of Attraction between Solvophobic Surfaces in Water and Organic Liquids Containing Dissolved Air," Langmuir **16**, 631.

Craig, V. S. J., 2011, "Very small bubbles at surfaces—the nanobubble puzzle," Soft Matter **7**, 40.

Dammer, S. M., and D. Lohse, 2006, "Gas enrichment at Liquid-Wall Interfaces," Phys. Rev. Lett. **96**, 206101.

Daniel, D., M. N. Mankin, R. A. Belisle, T.-S. Wong, and J. Aizenberg, 2013, "Lubricant-infused micro/nano-structured surfaces with tunable dynamic omniphobicity at high temperatures," Appl. Phys. Lett. **102**, 231603.

Darwich, S., K. Mougin, L. Vidal, E. Gnecco, and H. Haidara, 2011, "Nanobubble and nanodroplet template growth of particle nanorings versus nanoholes in drying nanofluids and polymer films," Nanoscale **3**, 1211.

Das, S., 2011, "Effect of impurities in the description of surface nanobubbles: Role of nonidealities in the surface layer," Phys. Rev. E **83**, 066315.

Das, S., J. H. Snoeijer, and D. Lohse, 2010, "Effect of impurities in description of surface nanobubbles," Phys. Rev. E **82**, 056310.

Daub, C. D., J. Wang, S. Kudesia, D. Bratko, and A. Luzar, 2010, "The influence of molecular-scale roughness on the surface spreading of an aqueous nanodrop," Faraday Discuss. **146**, 67.

Debuisson, D., R. Dufur, V. Senez, and S. Arscott, 2011, "Wetting on smooth micropatterned defects," Appl. Phys. Lett. **99**, 184101.

Debuisson, D., V. Senez, and S. Arscott, 2011, "Tunable contact angle hysteresis by micropatterning surfaces," Appl. Phys. Lett. **98**, 184101.

Deegan, R. D., O. Bakajin, T. F. Dupont, G. Huber, S. R. Nagel, and T. A. Witten, 1997, "Capillary flow as the cause of ring stains from dried liquid drops," Nature (London) **389**, 827.

de Gennes, P. G., 1985, "Wetting: statics and dynamics," Rev. Mod. Phys. **57**, 827.

de Gennes, P. G., 2002, "On fluid/wall slippage," Langmuir **18**, 3413.

de Gennes, P. G., F. Brochard-Wyart, and D. Quere, 2004, *Capillarity and wetting phenomena: drops, bubbles, pearls, waves* (Springer, New York).

Dietrich, E., E. S. Kooij, H. J. W. Z. Xuehua Zhang, and D. Lohse, 2015, "Stick-Jump Mode in Surface Droplet Dissolution," Langmuir **31**, 4696.

Dietrich, E., H. J. W. Zandvliet, D. Lohse, and J. R. T. Seddon, 2013, "Particle tracking around surface nanobubbles," J. Phys. Condens. Matter **25**, 184009.

Doshi, D. A., E. B. Watkins, J. N. Israelachvili, and J. Majewski, 2005, "Reduced water density at hydrophobic surfaces: Effect of dissolved gases," Proc. Natl. Acad. Sci. U.S.A. **102**, 9458.

Dressaire, E., R. Bee, D. C. Bell, A. Lips, and H. A. Stone, 2008, "Interfacial polygonal nanopatterning of stable microbubbles," Science **320**, 1198.

Du, Q., R. Superfine, E. Freysz, and Y. Shen, 1993, "Vibrational Spectroscopy of Water at the Vapor Water Interface," Phys. Rev. Lett. **70**, 2313.

Ducker, W. A., 2009, "Contact angle and stability of interfacial nanobubbles," Langmuir **25**, 8907.

Duncan, P. B., and D. Needham, 2006, "Microdroplet dissolution into a second-phase solvent using a micropipet technique: test of the Epstein-Plesset model for an aniline-water system," Langmuir **22**, 4190.

Duval, E., S. Adichtchev, S. Sirotkin, and A. Mermet, 2012, "Long-lived submicrometric bubbles in very diluted alkali halide water solutions," Phys. Chem. Chem. Phys. **14**, 4125.

Eckhardt, W., *et al.*, 2013, "591 TFLOPS Multi-trillion Particles Simulation on SuperMUC," in *Supercomputing Lecture Notes in Computer Science*, edited by J. M. Kunkel, T. Ludwig, and H. W. Meuer (Springer, New York), Vol. 7905, pp. 1–12.

Eggers, J., and L. M. Pismen, 2010, "Nonlocal description of evaporating drops," Phys. Fluids **22**, 112101.
Eller, A., and H. G. Flynn, 1965, "Rectified Diffusion During Nonlinear Pulsations of Cavitation Bubbles," J. Acoust. Soc. Am. **37**, 493.
Enriquez, O. R., C. Hummelink, G.-W. Bruggert, D. Lohse, A. Prosperetti, D. van der Meer, and C. Sun, 2013, "Growing bubbles in a slightly oversaturated liquid solution," Rev. Sci. Instrum. **84**, 065111.
Enriquez, O. R., C. Sun, D. Lohse, A. Prosperetti, and D. van der Meer, 2014, "The quasi-static growth of CO_2 bubbles," J. Fluid Mech. **741**, R1.
Epstein, P. S., and M. S. Plesset, 1950, "On the stability of gas bubbles in liquid-gas solutions," J. Chem. Phys. **18**, 1505.
Evans, D. R., V. S. J. Craig, and T. J. Senden, 2004, "The hydrophobic force: nanobubbles or polymeric contaminant?," Physica (Amsterdam) **339A**, 101.
Faghihnejad, A., and H. Zeng, 2013, "Interaction Mechanism between Hydrophobic and Hydrophilic Surfaces: Using Polystyrene and Mica as a Model System," Langmuir **29**, 12 443.
Fang, Z., Y. R. Zhen, O. Neumann, A. Polman, G. de Abajo, F. Javier, P. Nordlander, and N. J. Halas, 2013, "Evolution of Light-Induced Vapor Generation at a Liquid-Immersed Metallic Nanoparticle," Nano Lett. **13**, 1736.
Feuillebois, F., M. Z. Bazant, and O. I. Vinogradova, 2009, "Effective Slip over Superhydrophobic Surfaces in Thin Channels," Phys. Rev. Lett. **102**, 026001.
Finger, A., and D. Johannsmann, 2011, "Hemispherical nanobubbles reduce interfacial slippage in simple liquids," Phys. Chem. Chem. Phys. **13**, 18015.
Frenkel, D., and B. Smit, 1996, *Understanding molecular simulations: From algorithm to applications* (Academic Press, San Diego).
Fujishima, A., and K. Honda, 1972, "Electrochemical photolysis of water at semiconductor electrode," Nature (London) **238**, 37.
Gao, L., G.-X. Ni, Y. Liu, B. Liu, A. H. Castro Neto, and K. P. Loh, 2014, "Face-to-face transfer of wafer-scale graphene films," Nature (London) **505**, 190.
Garcia, R., and R. Perez, 2002, "Dynamic atomic force microscopy methods," Surf. Sci. Rep. **47**, 197.
Geissler, A., M. Biesalski, T. Heinze, and K. Zhang, 2014, "Formation of nanostructured cellulose stearoyl esters via nanoprecipitation," J. Mater. Chem. A **2**, 1107.
Gelderblom, H., A. G. Marin, H. Nair, A. van Houselt, L. Lefferts, J. H. Snoeijer, and D. Lohse, 2011, "How water droplets evaporate on a superhydrophobic substrate," Phys. Rev. E **83**, 026306.
German, S. R., X. Wu, H. An, V. S. J. Craig, T. L. Mega, and X. Zhang, 2014, "Interfacial Nanobubbles Are Leaky: Permeability of the Gas/Water Interface," ACS Nano **8**, 6193.
Getta, T., and S. Dietrich, 1998, "Line tension between fluid phases and a substrate," Phys. Rev. E **57**, 655.
Gibbs, J. W., 1957, *The collected works of J. W. Gibbs* (Yale University Press, New Haven, CT).
Giessibl, F., 2003, "Advances in atomic force microscopy," Rev. Mod. Phys. **75**, 949.
Gong, W., J. Stearnes, D. Fornasiero, R. A. Hayes, and J. Ralston, 1999, "The influence of dissolved gas on the interactions between surfaces of different hydrophobicity in aqueous media," Phys. Chem. Chem. Phys. **1**, 2799.
Grogan, J. M., N. M. Schneider, F. M. Ross, and H. H. Bau, 2014, "Bubble and Pattern Formation in Liquid Induced by an Electron Beam," Nano Lett. **14**, 359.
Grossmann, S., and D. Lohse, 2004, "Fluctuations in turbulent Rayleigh-Bénard convection: The role of plumes," Phys. Fluids **16**, 4462.
Guan, M., W. Guo, L. Gao, Y. Tang, J. Hu, and Y. Dong, 2012, "Investigation on the temperature difference method for producing nanobubbles and their physical properties," ChemPhysChem **13**, 2115.
Guggenheim, E. A., 1967, *Thermodynamics* (North-Holland, Amsterdam).
Guillemot, L., T. Biben, A. Galarneau, G. Vigier, and E. Charlaix, 2012, "Activated drying in hydrophobic nanopores and the line tension of water," Proc. Natl. Acad. Sci. U.S.A. **109**, 19 557.
Guix, M., C. C. Mayorga-Martinez, and A. Merkoci, 2014, "Nano/Micromotors in (Bio)chemical Science Applications," Chem. Rev. **114**, 6285.
Guo, W., H. Shan, M. Guan, L. Gao, M. Liu, and Y. Dong, 2012, "Investigation on nanobubbles on graphite substrate produced by the water-NaCl solution replacement," Surf. Sci. **606**, 1462.
Hain, N., S. Zheng, S. Druzhinin, and H. Schönherr, 2015, "FLIM techniques for nanobubbles," unpublished.
Halas, N. J., S. Lal, W.-S. Chang, S. Link, and P. Nordlander, 2011, "Plasmons in Strongly Coupled Metallic Nanostructures," Chem. Rev. **111**, 3913.
Hammadi, Z., R. Morin, and J. Olives, 2013, "Field nano-localization of gas bubble production from water electrolysis," Appl. Phys. Lett. **103**, 223106.
Hampton, M. A., B. C. Donose, and A. V. Nguyen, 2008, "Effect of alcohol-water exchange and surface scanning on nanobubbles and the attraction between hydrophobic surfaces," J. Colloid Interface Sci. **325**, 267.
Hampton, M. A., and A. V. Nguyen, 2010, "Nanobubbles and the nanobubble bridging capillary force," Adv. Colloid Interface Sci. **154**, 30.
Hansen, W. N., 1973, *Advances in Electrochemistry and Electrochemical Engineering* (Wiley, New York).
Harper, J. F., 1973, "Bubble with small immobile adsorbed films rising in liquids at low Reynolds numbers," J. Fluid Mech. **58**, 539.
Harvey, C. E., E. M. van Schrojenstein Lantman, A. J. G. Mank, and B. M. Weckhuysen, 2012, "An integrated AFM-Raman instrument for studying heterogeneous catalytic systems: a first showcase," Chem. Commun. (Cambridge) **48**, 1742.
Harvey, E. N., D. K. Barnes, W. D. McElroy, A. H. Whiteley, D. C. Pease, and K. W. Cooper, 1944, "Bubble formation in animals. I. Physical factors," J. Cell. Comp. Physiol. **24**, 1.
Heim, L.-O., and E. Bonaccurso, 2013, "Measurement of Line Tension on Droplets in the Submicrometer Range," Langmuir **29**, 14 147.
Hofer, W., A. Foster, and A. Shluger, 2003, "Theories of scanning probe microscopes at the atomic scale," Rev. Mod. Phys. **75**, 1287.
Holmberg, M., A. Kühle, J. Garnaes, K. A. Morch, and A. Boisen, 2003, "Nanobubble trouble on gold surfaces," Langmuir **19**, 10 510.
Howarter, J. A., and J. P. Youngblood, 2006, "Optimization of silica silanization by 3-aminopropyltriethoxysilane," Langmuir **22**, 11 142.
Hu, H., and R. G. Larson, 2002, "Evaporation of a Sessile Droplet on a Substrate," J. Phys. Chem. B **106**, 1334.
Huang, C., J. Jiang, M. Lu, L. Sun, E. I. Meletis, and Y. Hao, 2009, "Capturing Electrochemically Evolved Nanobubbles by Electroless Deposition. A Facile Route to the Synthesis of Hollow Nanoparticles," Nano Lett. **9**, 4297.

Huang, T.-W., *et al.*, 2013, "Dynamics of hydrogen nanobubbles in KLH protein solution studied with *in situ* wet-TEM," Soft Matter **9**, 8856.

Hui, F., B. Li, P. He, J. Hu, and Y. Fang, 2009, "Electrochemical fabrication of nanoporous polypyrrole film on HOPG using nanobubbles as templates," Electrochem. Comm. **11**, 639.

Hyväluoma, J., C. Kunert, and J. Harting, 2011, "Simulations of slip flow on nanobubble-laden surfaces," J. Phys. Condens. Matter **23**, 184106.

Ishida, N., T. Inoue, M. Miyahara, and K. Higashitani, 2000, "Nano bubbles on a hydrophobic surface in water observed by tapping-mode atomic force microscopy," Langmuir **16**, 6377.

Ishida, N., Y. Kusaka, and H. Ushijima, 2012, "Hydrophobic Attraction between Silanated Silica Surfaces in the Absence of Bridging Bubbles," Langmuir **28**, 13 952.

Ismagilov, R. F., A. Schwartz, N. Bowden, and G. M. Whitesides, 2002, "Autonomous Movement and Self-Assembly," Angew. Chem., Int. Ed. Engl. **41**, 652.

Israelachvili, J., 1991, *Intermolecular and surface forces* (Academic Press, New York).

Jin, F., J. Li, X. Ye, and C. Wu, 2007, "Effects of pH and ionic strength on the stability of nanobubbles in aqueous solutions of alpha-cyclodextrin," J. Phys. Chem. B **111**, 11 745.

Joanny, J., and P. de Gennes, 1984, "A model for contact angle hysteresis," J. Chem. Phys. **81**, 552.

Jones, S. F., G. M. Evans, and K. P. Galvin, 1999, "Bubble nucleation from gas cavities: a review," Adv. Colloid Interface Sci. **80**, 27.

Kameda, N., and S. Nakabayashi, 2008, "Size-induced sign inversion of line tension in nanobubbles at a solid/liquid interface," Chem. Phys. Lett. **461**, 122.

Kameda, N., N. Sogoshi, and S. Nakabayashi, 2008, "Nitrogen nanobubbles and butane nanodroplets at Si(100)," Surf. Sci. **602**, 1579.

Kaptay, G., 2012, "On the size and shape dependence of the solubility of nano-particles in solutions," Int. J. Pharm. **430**, 253.

Karpitschka, S., E. Dietrich, J. R. T. Seddon, H. J. W. Zandvliet, D. Lohse, and H. Riegler, 2012, "Nonintrusive Optical Visualization of Surface Nanobubbles," Phys. Rev. Lett. **109**, 066102.

Karraker, K., and C. Radke, 2002, "Disjoining pressures zeta potentials and surface tensions of aqueous non-ionic surfactant/electrolyte solutions: theory and comparison to experiment," Adv. Colloid Interface Sci. **96**, 231.

Kim, P., T.-S. Wong, J. Alvarenga, M. J. Kreder, W. E. Adorno-Martinez, and J. Aizenberg, 2012, "Liquid-Infused Nanostructured Surfaces with Extreme Anti-Ice and Anti-Frost Performance," ACS Nano **6**, 6569.

Klassen, V. I., and V. A. Mokrousov, 1983, *An introduction to the theory of flotation* (Butterworths, Oxford).

Köhler, R., P. Lazar, and H. Riegler, 2006, "Optical imaging of thin films with molecular depth resolution," Appl. Phys. Lett. **89**, 241906.

Koplik, J., and J. R. Banavar, 1995, "Continuum Deductions from Molecular Hydrodynamics," Annu. Rev. Fluid Mech. **27**, 257.

Koplik, J., and R. Zhang, 2013, "Nanodrop impact on solid surfaces," Phys. Fluids **25**, 022003.

Lauga, E., M. P. Brenner, and H. A. Stone, 2007, "Microfluidics: The no-slip boundary condition," in *Handbook of Experimental Fluid Dynamics*, edited by C. Tropea, A. Yarin, and J. F. Foss (Springer, New York), pp. 1219–1240.

Ledesma-Aguilar, R., D. Vella, and J. M. Yeomans, 2014, "Lattice-Boltzmann simulations of droplet evaporation," Soft Matter **10**, 8267.

Lee, J., T. Laoui, and R. Karnik, 2014, "Nanofluidic transport governed by the liquid/vapour interface," Nat. Nanotechnol. **9**, 317.

Lee, T., E. Charrault, and C. Neto, 2014, "Interfacial slip on rough, patterned and soft surfaces: A review of experiments and simulations," Adv. Colloid Interface Sci. **210**, 21.

Leger, L., and J. F. Joanny, 1992, "Liquid spreading," Rep. Prog. Phys. **55**, 431.

Leighton, T. G., 1994, *The acoustic bubble* (Academic Press, London).

Leung, K., A. Luzar, and D. Bratko, 2003, "Dynamics of Capillary Drying in Water," Phys. Rev. Lett. **90**, 065502.

Lhuissier, H., D. Lohse, and X. Zhang, 2014, "Spatial organization of surface nanobubbles and implications on their formation process," Soft Matter **10**, 942.

Li, D., D. Jing, Y. Pan, W. Wang, and X. Zhao, 2014, "Coalescence and Stability Analysis of Surface Nanobubbles on the Polystyrene/Water Interface," Langmuir **30**, 6079.

Li, G., H.-J. Butt, and K. H. Graf, 2006, "Microstructures by solvent drop evaporation on polymer surfaces: dependence on molar mass," Langmuir **22**, 11 395.

Lide, D. R., 1995, Ed., *CRC Handbook of Chemistry and Physics* (CRC Press, Boca Raton).

Lindner, J. R., 2004, "Microbubbles in medical imaging: current applications and future directions," Nat. Rev. Drug Discovery **3**, 527.

Liu, G., and V. S. J. Craig, 2009, "Improved Cleaning of Hydrophilic Protein-Coated Surfaces using the Combination of Nanobubbles and SDS," ACS Appl. Mater. Interfaces **1**, 481.

Liu, G., Z. Wu, and V. S. J. Craig, 2008, "Cleaning of protein-coated surfaces using nanobubbles: An investigation using a quartz crystal microbalance," J. Phys. Chem. C **112**, 16 748.

Liu, M., W. Zhao, S. Wang, W. Guo, Y. Tang, and Y. Dong, 2013, "Study on Nanobubble Generation: Saline Solution/Water Exchange Method," ChemPhysChem **14**, 2589.

Liu, S., J. Duvigneau, and G. J. Vancso, 2015, "Nanocellular polymer foams as promising high performance thermal insulation materials," Eur. Polym. J. **65**, 33.

Liu, Y., and S. J. Dillon, 2014, "In situ observation of electrolytic H_2 evolution adjacent to gold cathodes," Chem. Commun. (Cambridge) **50**, 1761.

Liu, Y., J. Wang, X. Zhang, and W. Wang, 2014, "Contact line pinning and the relationship between nanobubbles and substrates," J. Chem. Phys. **140**, 054705.

Liu, Y., and X. Zhang, 2013a, "Evaporation dynamics of nanodroplets and their anomalous stability on rough substrates," Phys. Rev. E **88**, 012404.

Liu, Y., and X. Zhang, 2013b, "Nanobubble stability induced by contact line pinning," J. Chem. Phys. **138**, 014706.

Liu, Y., and X. Zhang, 2014, "A unified mechanism for the stability of surface nanobubbles: Contact line pinning and supersaturation," J. Chem. Phys. **141**, 134702.

Ljunggren, S., and J. C. Eriksson, 1997, "The lifetime of a colloid-sized gas bubble in water and the cause of the hydrophobic attraction," Colloids Surf., A **129–130**, 151.

Lohse, D., and X. Zhang, 2015, "Pinning and gas oversaturation imply stable single surface nanobubble," Phys. Rev. E **91**, 031003(R).

Lou, S., J. Gao, X. Xiao, X. Li, G. Li, Y. Zhang, M. Li, J. Sun, X. Li, and J. Hu, 2002, "Studies of nanobubbles produced at liquid/solid interfaces," Mater. Charact. **48**, 211.

Lou, S.-T., Z.-Q. Ouyang, Y. Zhang, X.-J. Li, J. Hu, M.-Q. Li, and F.-J. Yang, 2000, "Nanobubbles on solid surface imaged by atomic force microscopy," J. Vac. Sci. Technol. B **18**, 2573.

Lu, Y.-H., C.-W. Yang, C.-K. Fang, H.-C. Ko, and I.-S. Hwang, 2014, "Interface-Induced Ordering of Gas Molecules Confined in a Small Space," Science Rep. **4**, 7189.

Lu, Y.-H., C.-W. Yang, and I.-S. Hwang, 2012, "Molecular Layer of Gaslike Domains at a Hydrophobic-Water Interface Observed by Frequency-Modulation Atomic Force Microscopy," Langmuir **28**, 12 691.

Lu, Y.-H., C.-W. Yang, and I.-S. Hwang, 2014, "Atomic Force Microscopy Study of Nitrogen Molecule Self-Assembly at the HOPG-Water Interface," Appl. Surf. Sci. **304**, 56.

Luederitz, L. A. C., and R. von Klitzing, 2012, "Scanning of Silicon Wafers in Contact with Aqueous CTAB Solutions below the CMC," Langmuir **28**, 3360.

Luederitz, L. A. C., and R. von Klitzing, 2013, "Interaction forces between silica surfaces in cationic surfactant solutions: An atomic force microscopy study," J. Colloid Interface Sci. **402**, 19.

Lukianova-Hleb, E., Y. Hu, L. Latterini, L. Tarpani, S. Lee, R. A. Drezek, J. H. Hafner, and D. O. Lapotko, 2010, "Plasmonic Nanobubbles as Transient Vapor Nanobubbles Generated around Plasmonic Nanoparticles," ACS Nano **4**, 2109.

Lum, K., D. Chandler, and J. D. Weeks, 1999, "Hydrophobicity at Small and Large Length Scales," J. Phys. Chem. B **103**, 4570.

Luo, J., J.-H. Im, M. T. Mayer, M. Schreier, M. K. Nazeeruddin, N.-G. Park, S. D. Tilley, H. J. Fan, and M. Grätzel, 2014, "Water photolysis at 12.3% efficiency via perovskite photovoltaics and Earth-abundant catalysts," Science **345**, 1593.

Luo, L., and H. S. White, 2013, "Electrogeneration of Single Nanobubbles at Sub-50-nm-Radius Platinum Nanodisk Electrodes," Langmuir **29**, 11 169.

Luzar, A., and D. Bratko, 2005, "Gas solubility in hydrophobic confinement," J. Phys. Chem. B **109**, 22 545.

Ma, A., J. Xu, X. Zhang, B. Zhang, D. Wang, and H. Xu, 2014, "Interfacial nanodroplets guided construction of hierarchical Au, Au-Pt, and Au-Pd particles as excellent catalysts," Sci. Rep. **4**, 4849.

Mahnke, J., J. Stearnes, R. A. Hayes, D. Fornasiero, and J. Ralston, 1999, "The influence of dissolved gas on the interactions between surfaces of different hydrophobicity in aqueous media Part I. Measurement of interaction forces," Phys. Chem. Chem. Phys. **1**, 2793.

Manjare, M., B. Yang, and Y.-P. Zhao, 2012, "Bubble Driven Quasioscillatory Translational Motion of Catalytic Micromotors," Phys. Rev. Lett. **109**, 128305.

Mao, M., J. Zhang, R.-H. Yoon, and W. A. Ducker, 2004, "Is there a thin film of air at the inteface between water and smooth hydrophobic solids?," Langmuir **20**, 1843.

Marin, A. G., H. Gelderblom, D. Lohse, and J. H. Snoeijer, 2011, "Order-to-Disorder Transition in Ring-Shaped Colloidal Stains," Phys. Rev. Lett. **107**, 085502.

Martinez, J., and P. Stroeve, 2007, "Transient behavior of the hydrophobic surface/water interface: From nanobubbles to organic layer," J. Phys. Chem. B **111**, 14 069.

Mastropietro, D. J., and W. A. Ducker, 2012, "Forces between Hydrophobic Solids in Concentrated Aqueous Salt Solution," Phys. Rev. Lett. **108**, 106101.

Mazumder, M., and B. Bhushan, 2011, "Propensity and geometrical distribution of surface nanobubbles: effect of electrolyte, roughness, pH, and substrate bias," Soft Matter **7**, 9184.

Mcgovern, M., K. Kallury, and M. Thompson, 1994, "Role of solvent on the silanization of glass with octadecyltrichlorosilane," Langmuir **10**, 3607.

Mendez-Vilas, A., A. B. Jodar-Reyes, and M. L. Gonzalez-Martin, 2009, "Ultrasmall Liquid Droplets on Solid Surfaces: Production, Imaging, and Relevance for Current Wetting Research," Small **5**, 1366.

Mezger, M., H. Reichert, S. Schoeder, J. Okasinski, H. Schroeder, H. Dosch, D. Palms, J. Ralston, and V. Honkimaki, 2006, "High-resolution *in situ* x-ray study of the hydrophobic gap at the water-octadecyl-trichlorosilane interface," Proc. Natl. Acad. Sci. U.S.A. **103**, 18 401.

Mishchuk, N., J. Ralston, and D. Fornasiero, 2002, "Influence of dissolved gas on van der Waals forces between bubbles and particles," J. Phys. Chem. A **106**, 689.

Mishchuk, N., J. Ralston, and D. Fornasiero, 2006, "Influence of very small bubbles on particle/bubble heterocoagulation," J. Colloid Interface Sci. **301**, 168.

Munz, M., and T. Mills, 2014, "Size Dependence of Shape and Stiffness of Single Sessile Oil Nanodroplets As Measured by Atomic Force Microscopy," Langmuir **30**, 4243.

Nadkarni, G. D., and S. Garoff, 1992, "An Investigation of Microscopic Aspects of Contact Angle Hysteresis: Pinning of the Contact Line on a Single Defect," Europhys. Lett. **20**, 523.

Nanda, N. C., and R. Schlief, 1993, Eds., *Advances in echo imaging using contrast enhancement* (Kluwer Academic Publishers, Dordrecht).

Neto, C., D. Evans, E. Bonaccurso, H. Butt, and V. Craig, 2005, "Boundary slip in Newtonian liquids: a review of experimental studies," Rep. Prog. Phys. **68**, 2859.

Neumann, A. W., R. J. Good, C. J. Hope, and M. Sejpal, 1974, "An equation-of-state approach to determine surface tensions of low-energy solids from contact angles," J. Colloid Interface Sci. **49**, 291.

Palmer, L. A., D. Cookson, and R. N. Lamb, 2011, "The Relationship Between Nanobubbles and the Hydrophobic Force," Langmuir **27**, 144.

Parker, J. L., P. M. Claesson, and P. Attard, 1994, "Bubbles, cavities and the long-ranged attraction between hydrophobic surfaces," J. Phys. Chem. **98**, 8468.

Patankar, N. A., 2010, "Supernucleating surfaces for nucleate boiling and dropwise condensation heat transfer," Soft Matter **6**, 1613.

Paxton, W., K. Kistler, C. Olmeda, A. Sen, S. St Angelo, Y. Cao, T. Mallouk, P. Lammert, and V. Crespi, 2004, "Catalytic nanomotors: Autonomous movement of striped nanorods," J. Am. Chem. Soc. **126**, 13 424.

Peng, H., G. R. Birkett, and A. V. Nguyen, 2013, "Origin of Interfacial Nanoscopic Gaseous Domains and Formation of Dense Gas Layer at Hydrophobic Solid-Water Interface," Langmuir **29**, 15 266.

Peng, H., M. A. Hampton, and A. V. Nguyen, 2013, "Nanobubbles do not sit alone at the solid-liquid interface," Langmuir **29**, 6123.

Petsev, N. D., M. S. Shell, and L. G. Leal, 2013, "Dynamic equilibrium explanation for nanobubbles' unusual temperature and saturation dependence," Phys. Rev. E **88**, 010402(R).

Phan, H. T., N. Caney, P. Marty, S. Colasson, and J. Gavillet, 2009, "Surface wettability control by nanocoating: The effects on pool boiling heat transfer and nucleation mechanism," Int. J. Heat Mass Transfer **52**, 5459.

Picknett, R. G., and R. Bexon, 1977, "The evaporation of sessile or pendant drops in still air," J. Colloid Interface Sci. **61**, 336.

Pismen, L. M., and Y. Pomeau, 2000, "Disjoining potential and spreading of thin layers in the diffuse interface model coupled to hydrodynamics," Phys. Rev. E **62**, 2480.

Pollack, G. L., 1991, "Why gases dissolve in liquids," Science **251**, 1323.

Polman, A., 2013, "Solar Steam Nanobubbles," ACS Nano **7**, 15.
Popov, Y. O., 2005, "Evaporative deposition patterns: Spatial dimensions of the deposit," Phys. Rev. E **71**, 036313.
Prosperetti, A., 2011, *Advanced Mathematics for Applications* (Cambridge University Press, Cambridge, England).
Quere, D., 2008, "Wetting and roughness," Annu. Rev. Mater. Sci. **38**, 71.
Ramiasa, M., J. Ralston, R. Fetzer, R. Sedev, D. M. Fopp-Spori, C. Morhard, C. Pacholski, and J. P. Spatz, 2013, "Contact Line Motion on Nanorough Surfaces: A Thermally Activated Process," J. Am. Chem. Soc. **135**, 7159.
Ramos, S. M. M., E. Charlaix, and A. Benyagoub, 2003, "Contact angle hysteresis on nano-structured surfaces," Surf. Sci. **540**, 355.
Ritchie, J. A., J. S. Yazdi, D. Bratko, and A. Luzar, 2012, "Metastable Sessile Nanodroplets on Nanopatterned Surfaces," J. Phys. Chem. C **116**, 8634.
Rodahl, M., F. Hook, A. Krozer, P. Brzezinski, and B. Kasemo, 1995, "Quartz-crystal microbalance setup for frequency and Q-factor measurements in gaseous and liquid environments," Rev. Sci. Instrum. **66**, 3924.
Roger, K., R. Botet, and B. Cabane, 2013, "Coalescence of Repelling Colloidal Droplets: A Route to Monodisperse Populations," Langmuir **29**, 5689.
Rothstein, J. P., 2010, "Slip on superhydrophobic surfaces," Annu. Rev. Fluid Mech. **42**, 89.
Scheludko, A., B. V. Toshev, and D. T. Bojadjiev, 1976, "Attachment of particles to a liquid surface (Capillary theory of flotation)," J. Chem. Soc., Faraday Trans. 1 **72**, 2815.
Schlichting, H., 1979, *Boundary layer theory* (McGraw-Hill, New York), 7th ed.
Schlief, R., 1991, "Ultrasound contrast agents," Curr. Opin. Radiol. **3**, 198.
Schönfeld, F., K. H. Graf, S. Hardt, and H.-J. Butt, 2008, "Evaporation dynamics of sessile liquid drops in still air with constant contact radius," Int. J. Heat Mass Transfer **51**, 3696.
Schubert, S., J. T. Delaney, Jr., and U. S. Schubert, 2011, "Nanoprecipitation and nanoformulation of polymers: from history to powerful possibilities beyond poly(lactic acid)," Soft Matter **7**, 1581.
Schwendel, D., T. Hayashi, R. Dahint, A. Pertsin, M. Grunze, R. Steitz, and F. Schreiber, 2003, "Interaction of water with self-assembled monolayers: Neutron relectivity measurements of the water density in the interface region," Langmuir **19**, 2284.
Seddon, J. R. T., O. Bliznyuk, E. S. Kooij, B. Poelsema, H. J. W. Zandvliet, and D. Lohse, 2010, "Dynamic dewetting through micropancake growth," Langmuir **26**, 9640.
Seddon, J. R. T., E. S. Kooij, B. Poelsema, H. J. W. Zandvliet, and D. Lohse, 2011, "Surface Bubble Nucleation Stability," Phys. Rev. Lett. **106**, 056101.
Seddon, J. R. T., and D. Lohse, 2011, "Nanobubbles and micropancakes: Gaseous domains on immersed substrates," J. Phys. Condens. Matter **23**, 133001.
Seddon, J. R. T., D. Lohse, W. A. Ducker, and V. S. J. Craig, 2012, "A deliberation on nanobubbles at surfaces and in bulk," ChemPhysChem **13**, 2179.
Seddon, J. R. T., H. J. W. Zandvliet, and D. Lohse, 2011, "Knudsen Gas Provides Nanobubble Stability," Phys. Rev. Lett. **107**, 116101.
Seemann, R., M. Brinkmann, E. J. Kramer, F. F. Lange, and R. Lipowsky, 2005, "Wetting morphologies at microstructured surfaces," Proc. Natl. Acad. Sci. U.S.A. **102**, 1848.
Sendner, C., D. Horinek, L. Bocquet, and R. R. Netz, 2009, "Interfacial water at hydrophobic and hydrophilic surfaces: Slip, viscosity, and diffusion," Langmuir **25**, 10 768.
Seo, H., M. Yoo, and S. Jeon, 2007, "Influence of nanobubbles on the adsorption of nanoparticles," Langmuir **23**, 1623.
Shanahan, M. E. R., 1995, "Simple theory of stick-slip wetting hysteresis," Langmuir **11**, 1041.
Shen, G., X. H. Zhang, Y. Ming, L. Zhang, Y. Zhang, and J. Hu, 2008, "Photocatalytic Induction of Nanobubbles on TiO_2 surfaces," J. Phys. Chem. C **112**, 4029.
Shin, D., J. B. Park, Y.-J. Kim, S. J. Kim, J. H. Kang, B. Lee, S.-P. Cho, B. H. Hong, and K. S. Novoselov, 2015, "Growth dynamics and gas transport mechanism of nanobubbles in graphene liquid cells," Nat. Commun. **6**, 6068.
Shumaker-Parry, J., and C. Campbell, 2004, "Quantitative methods for spatially resolved adsorption/desorption measurements in real time by surface plasmon resonance microscopy," Anal. Chem. **76**, 907.
Simonsen, A. C., P. L. Hansen, and B. Klösgen, 2004, "Nanobubbles give evidence of incomplete wetting at a hydrophobic interface," J. Colloid Interface Sci. **273**, 291.
Snoeijer, J. H., and B. Andreotti, 2008, "A microscopic view on contact angle selection," Phys. Fluids **20**, 057101.
Snoeijer, J. H., and B. Andreotti, 2013, "Moving Contact Lines: Scales, Regimes, and Dynamical Transitions," Annu. Rev. Fluid Mech. **45**, 269.
Solovev, A. A., Y. Mei, E. Bermudez Urena, G. Huang, and O. G. Schmidt, 2009, "Catalytic Microtubular Jet Engines Self-Propelled by Accumulated Gas Bubbles," Small **5**, 1688.
Song, B., W. Walczyk, and H. Schönherr, 2011, "Contact Angles of Surface Nanobubbles on Mixed Self-Assembled Monolayers with Systematically Varied Macroscopic Wettability by Atomic Force Microscopy," Langmuir **27**, 8223.
Stauber, J. M., S. K. Wilson, B. R. Duffy, and K. Sefiane, 2014, "On the lifetimes of evaporating droplets," J. Fluid Mech. **744**, R2.
Steinfeld, A., 2005, "Solar thermochemical production of hydrogen—a review," Solar Energy **78**, 603.
Steitz, R., T. Gutberlet, T. Hauss, B. Klösgen, R. Krastev, S. Schemmel, A. C. Simonsen, and G. H. Findenegg, 2003, "Nanobubbles and their precursor layer at the interface of water against a hydrophobic substrate," Langmuir **19**, 2409.
Stevens, H., R. F. Considine, C. J. Drummond, R. A. Hayes, and P. Attard, 2005, "Effects of degassing on the long-range attractive force between hydrophobic surfaces in water," Langmuir **21**, 6399.
Stöckelhuber, K. W., B. Radoev, A. Wenger, and H. J. Schulze, 2004, "Rupture of wetting films caused by nanobubbles," Langmuir **20**, 164.
Su, J. T., and D. Needham, 2013, "Mass Transfer in the Dissolution of a Multicomponent Liquid Droplet in an Immiscible Liquid Environment," Langmuir **29**, 13 339.
Suslick, K. S., and G. J. Price, 1999, "Application of ultrasound to materials chemistry," Annu. Rev. Mater. Sci. **29**, 295.
Svetovoy, V., I. Devic, J. H. Snoeijer, and D. Lohse, 2015, "The effect of disjoining pressure and surface nanobubbles," unpublished.
Svetovoy, V. B., R. G. P. Sanders, and M. C. Elwenspoek, 2013, "Transient nanobubbles in short-time electrolysis," J. Phys. Condens. Matter **25**, 184002.
Svetovoy, V. B., R. G. P. Sanders, T. S. J. Lammerink, and M. C. Elwenspoek, 2011, "ICombustion of hydrogen-oxygen mixture in electrochemically generated nanobubbles," Phys. Rev. E **84**, 035302.
Svetovoy, V. B., R. G. P. Sanders, K. Ma, and M. C. Elwenspoek, 2014, "New type of microengine using internal combustion of hydrogen and oxygen," Sci. Rep. **4**, 4296.

Switkes, M., and J. W. Ruberti, 2004, "Rapid cryofixation/freeze fracture for the study of nanobubbles at solid-liquid interfaces," Appl. Phys. Lett. **84**, 4759.

Takata, Y., J. Cho, B. Law, and M. Aratono, 2006, "Ellipsometric search for vapor layers at liquid-hydrophobic solid surfaces," Langmuir **22**, 1715.

Thomann, I., B. A. Pinaud, Z. Chen, B. M. Clemens, T. F. Jaramillo, and M. L. Brongersma, 2011, "Plasmon Enhanced Solar-to-Fuel Energy Conversion," Nano Lett. **11**, 3440.

Thormann, E., A. C. Simonsen, P. L. Hansen, and O. G. Mouritsen, 2008, "Force trace hysteresis and temperature dependence of bridging nanobubble induced forces between hydrophobic surfaces," ACS Nano **2**, 1817.

Tsai, W., P. Hsu, Y. Hwu, C. Chen, L. Chang, J. Je, H. Lin, A. Groso, and G. Margaritondo, 2002, "Electrochemistry—Building on bubbles in metal electrodeposition," Nature Rev. Urol. **417**, 139.

Tyrode, E., M. W. Rutland, and C. D. Bain, 2008, "Adsorption of CTAB on Hydrophilic Silica Studied by Linear and Nonlinear Optical Spectroscopy," J. Am. Chem. Soc. **130**, 17 434.

Tyrrell, J. W. G., and P. Attard, 2001, "Images of Nanobubbles on Hydrophobic Surfaces and their Interactions," Phys. Rev. Lett. **87**, 176104.

Tyrrell, J. W. G., and P. Attard, 2002, "Atomic force microscope images of nanbubbles on a hydrophobic surface and corresponding force-separation data," Langmuir **18**, 160.

van Limbeek, M. A. J., and J. R. T. Seddon, 2011, "Surface nanobubbles as a function of gas type," Langmuir **27**, 8694.

van Schrojenstein Lantman, E. M., T. Deckert-Gaudig, A. J. G. Mank, V. Deckert, and B. M. Weckhuysen, 2012, "Catalytic processes monitored at the nanoscale with tip-enhanced Raman spectroscopy," Nat. Nanotechnol. **7**, 583.

Velasco-Velez, J.-J., C. H. Wu, T. A. Pascal, L. F. Wan, J. Guo, D. Prendergast, and M. Salmeron, 2014, "The structure of interfacial water on gold electrodes studied by x-ray absorption spectroscopy," Science **346**, 831.

Vitale, S., and J. Katz, 2003, "Liquid droplet dispersions formed by homogeneous liquid-liquid nucleation: "The ouzo effect"," Langmuir **19**, 4105.

Vogt, H., and R. Balzer, 2005, "The bubble coverage of gas-evolving electrodes in stagnant electrolytes," Electrochim. Acta **50**, 2073.

Walczyk, W., N. Hain, and H. Schönherr, 2014, "Hydrodynamic effects of the tip movement on surface nanobubbles: a combined tapping mode, lift mode and force volume mode AFM study," Soft Matter **10**, 5945.

Walczyk, W., P. M. Schön, and H. Schönherr, 2013, "The effect of peakforce tapping mode AFM imaging on the apparent shape of surface nanobubbles," J. Phys. Condens. Matter **25**, 184005.

Walczyk, W., and H. Schönherr, 2014, "Dimensions and the Profile of Surface Nanobubbles: Tip-Nanobubble Interactions and Nanobubble Deformation in Atomic Force Microscopy," Langmuir **30**, 11 955.

Wang, M., K. Liechti, Q. Wang, and J. White, 2005, "Self-assembled silane monolayers: Fabrication with nanoscale uniformity," Langmuir **21**, 1848.

Wang, X., B. Zhao, W. Ma, Y. Wang, X. Gao, R. Tai, X. Zhou, and L. Zhang, 2015, "Interfacial Nanobubbles on Atomically Flat Substrates with Different Hydrophobicities," ChemPhysChem **16**, 1003.

Wang, Y., and B. Bhushan, 2010, "Boundary slip and nanobubble study in micro/nanofluidics using atomic force microscopy," Soft Matter **6**, 29.

Wang, Y., B. Bhushan, and X. Zhao, 2009a, "Improved nanobubble immobility induced by surface structures on hydrophobic surfaces," Langmuir **25**, 9328.

Wang, Y., B. Bhushan, and X. Zhao, 2009b, "Nanoindents produced by nanobubbles on ultrathin polystyrene films in water," Nanotechnology **20**, 045301.

Wang, Y., and M. Lieberman, 2003, "Growth of ultrasmooth octadecyltrichlorosilane self-assembled monolayers on SiO2," Langmuir **19**, 1159.

Weijs, J. H., B. Andreotti, and J. H. Snoeijer, 2013, "Elasto-capillarity at the nanoscale: on the coupling between elasticity and surface energy in soft solids," Soft Matter **9**, 8494.

Weijs, J. H., and D. Lohse, 2013, "Why Surface Nanobubbles Live for Hours," Phys. Rev. Lett. **110**, 054501.

Weijs, J. H., A. Marchand, B. Andreotti, D. Lohse, and J. H. Snoeijer, 2011, "Origin of line tension for a Lennard-Jones nanodroplet," Phys. Fluids **23**, 022001.

Weijs, J. H., J. R. T. Seddon, and D. Lohse, 2012, "Diffusive Shielding Stabilizes Bulk Nanobubble Clusters," ChemPhysChem **13**, 2197.

Weijs, J. H., J. H. Snoeijer, and D. Lohse, 2012, "Surface Nanobubbles: Formation and Universality of the Contact Angle," Phys. Rev. Lett. **108**, 104501.

Westerheide, D., and J. Westwater, 1961, "Isothermal growth of hydrogen bubbles during electrolysis," AIChE J. **7**, 357.

Wilson, D. A., R. J. M. Nolte, and J. C. M. van Hest, 2012, "Autonomous movement of platinum-loaded stomatocytes," Nat. Chem. **4**, 268.

Wong, T.-S., S. H. Kang, S. K. Y. Tang, E. J. Smythe, B. D. Hatton, A. Grinthal, and J. Aizenberg, 2011, "Bioinspired self-repairing slippery surfaces with pressure-stable omniphobicity," Nature (London) **477**, 443.

Woods, D. A., and C. D. Bain, 2012, "Total internal reflection Raman spectroscopy," Analyst. **137**, 35.

Wu, C., K. Nesset, J. Masliyah, and Z. Xu, 2012, "Generation and characterization of submicron size bubbles," Adv. Colloid Interface Sci. **179–182**, 123.

Wu, Z., H. Chen, Y. Dong, H. Mao, J. Sun, S. Chen, V. S. J. Craig, and J. Hu, 2008, "Cleaning using nanobubbles: Defouling by electrochemical generation of bubbles," J. Colloid Interface Sci. **328**, 10.

Xu, C., S. Peng, G. O. Qiao, V. Gutowski, D. Lohse, and X. Zhang, 2014, "Nanobubbles on a warmer substrate," Soft Matter **10**, 7857.

Yakubov, G. E., H.-J. Butt, and O. I. Vinogradova, 2000, "Interaction forces between hydrophobic surfaces. Attractive jump as an indication of formation of "stable" submicrocavities," J. Phys. Chem. B **104**, 3407.

Yan, X., M. Delgado, A. Fu, P. Alcouffe, S. G. Gouin, E. Fleury, J. L. Katz, F. Ganachaud, and J. Bernard, 2014, "Simple but Precise Engineering of Functional Nanocapsules through Nanoprecipitation," Angew. Chem., Int. Ed. **53**, 6910.

Yang, C. W., Y. H. Lu, and I. S. Hwang, 2013, "Imaging surface nanobubbles at graphite-water interfaces with different atomic force microscopy modes," J. Phys. Condens. Matter **25**, 184010.

Yang, H., S. Peng, X. Hao, T. A. Smith, G. G. Qiao, and X. Zhang, 2014, "Surfactant-mediated formation of polymeric microlenses from interfacial microdroplets," Soft Matter **10**, 957.

Yang, J., J. Duan, D. Fornasiero, and J. Ralston, 2003, "Very small bubble formation at the solid-water interface," J. Phys. Chem. B **107**, 6139.

Yang, J., J. Duan, D. Fornasiero, and J. Ralston, 2007, "Kinetics of CO_2 nanobubble formation at the solid/water interface," Phys. Chem. Chem. Phys. **9**, 6327.

Yang, S., S. M. Dammer, N. Bremond, H. J. W. Zandvliet, E. S. Kooij, and D. Lohse, 2007, "Characterization of nanobubbles on hydrophobic surfaces in water," Langmuir **23**, 7072.

Yang, S., E. S. Kooij, B. Poelsema, D. Lohse, and H. J. W. Zandvliet, 2008, "Correlation between geometry and nanobubble distribution on HOPG surface," Europhys. Lett. **81**, 64006.

Yang, S., P. Tsai, E. S. Kooij, A. Prosperetti, H. J. W. Zandvliet, and D. Lohse, 2009, "Electrolytically generated nanobubbles on highly orientated pyrolytic graphite surfaces," Langmuir **25**, 1466; **29**, 5937(E) (2013).

Yasui, K., T. Tuziuti, W. Kanematsu, and K. Kato, 2015, "Advanced dynamic-equilibrium model for a nanobubble and a micropancake on a hydrophobic or hydrophilic surface," Phys. Rev. E **91**, 033008.

Zakzeski, J., P. C. A. Bruijnincx, A. L. Jongerius, and B. M. Weckhuysen, 2010, "The Catalytic Valorization of Lignin for the Production of Renewable Chemicals," Chem. Rev. **110**, 3552.

Zhang, D., and K. Zeng, 2012, "Evaluating the Behavior of Electrolytic Gas Bubbles and Their Effect on the Cell Voltage in Alkaline Water Electrolysis," Ind. Eng. Chem. Res. **51**, 13 825.

Zhang, L., X. Zhang, C. Fan, Y. Zhang, and J. Hu, 2009, "Nanoscale multiple gaseous layers on a hydrophobic surface," Langmuir **25**, 8860.

Zhang, L., X. Zhang, Y. Zhang, J. Hu, and H. Fang, 2010, "The length scales for stable gas nanobubbles at liquid/solid surfaces," Soft Matter **6**, 4515.

Zhang, L., Y. Zhang, X. Zhang, Z. Li, G. Shen, M. Ye, C. Fan, H. Fang, and J. Hu, 2006, "Electrochemically controlled formation and growth of hydrogen nanobubbles," Langmuir **22**, 8109.

Zhang, L., B. Zhao, L. Xue, Z. Guo, Y. Dong, H. Fang, R. Tai, and J. Hu, 2013, "Imaging interfacial micro- and nano-bubbles by scanning transmission soft X-ray microscopy," J. Synchrotron Radiat. **20**, 413.

Zhang, X., D. Y. C. Chan, D. Wang, and N. Maeda, 2013, "Stability of Interfacial Nanobubbles," Langmuir **29**, 1017.

Zhang, X., and W. Ducker, 2007, "Formation of interfacial nanodroplets through changes in solvent quality," Langmuir **23**, 12 478.

Zhang, X., A. Kumar, and P. J. Scales, 2011, "Effects of solvency and interfacial nanobubbles on surface forces and bubble attachment at solid surfaces," Langmuir **27**, 2484.

Zhang, X., H. Lhuissier, O. R. Enriquez, C. Sun, and D. Lohse, 2013, "Deactivation of Microbubble Nucleation Sites by Alcohol-Water Exchange," Langmuir **29**, 9979.

Zhang, X., H. Lhuissier, C. Sun, and D. Lohse, 2014, "Surface Nanobubbles Nucleate Microplets," Phys. Rev. Lett. **112**, 144503.

Zhang, X., and D. Lohse, 2014, "Perspectives on surface nanobubbles," Biomicrofluidics **8**, 041301.

Zhang, X., and N. Maeda, 2011, "Interfacial Gaseous States on Crystalline Surfaces," J. Phys. Chem. C **115**, 736.

Zhang, X., M. H. Uddin, H. Yang, G. Toikka, W. Ducker, and N. Maeda, 2012, "Effects of surfactants on the formation and the stability of interfacial nanobubbles," Langmuir **28**, 10471.

Zhang, X., J. Wang, L. Bao, E. Dietrich, R. C. A. van der Veen, S. Peng, J. Friend, H. J. W. Zandvliet, L. Yeo, and D. Lohse, 2015, "Mixed mode of dissolving immersed microdroplets at a solid-water interface," Soft Matter **11**, 1889.

Zhang, X., X. Wei, and W. Ducker, 2010, "Formation of Nanodents by Deposition of Nanodroplets at the Polymer-Liquid Interface," Langmuir **26**, 4776.

Zhang, X., Z. Wu, X. Zhang, G. Li, and J. Hu, 2005, "Nanobubbles at the interface of HOPG and ethanol solution," Int. J. Nanosci. **04**, 399.

Zhang, X. H., 2008, "Quartz crystal microbalance study of the interfacial nanobubbles," Phys. Chem. Chem. Phys. **10**, 6842.

Zhang, X. H., A. Khan, and W. A. Ducker, 2007, "A Nanoscale Gas State," Phys. Rev. Lett. **98**, 136101.

Zhang, X. H., G. Li, N. Maeda, and J. Hu, 2006, "Removal of induced nanobubbles from water/graphite interfaces by partial degassing," Langmuir **22**, 9238.

Zhang, X. H., G. Li, Z. H. Wu, X. D. Zhang, and J. Hu, 2005, "Effect of temperature on the morphology of nanobubbles at mica/water interface," Chin. Phys. **14**, 1774.

Zhang, X., Z. Lu, H. Tan, L. Bao, Y. He, C. Sun, and D. Lohse, 2015, "Formation of surface nanodroplets under controlled flow conditions," Proc. Natl. Acad. Sci. U.S.A. **112**, 9253.

Zhang, X. H., N. Maeda, and V. S. J. Craig, 2006, "Physical properties of nanobubbles on hydrophobic surface in water and aqueous solutions," Langmuir **22**, 5025.

Zhang, X. H., N. Maeda, and J. Hu, 2008, "Thermodynamic stability of interfacial gaseous states," J. Phys. Chem. B **112**, 13 671.

Zhang, X. H., A. Quinn, and W. A. Ducker, 2008, "Nanobubbles at the interface between water and a hydrophobic solid," Langmuir **24**, 4756.

Zhang, X. H., J. M. Ren, H. J. Yang, Y. H. He, J. F. Tan, and G. G. Qiao, 2012, "From Transient Nanodroplets to Permanent Nanolenses," Soft Matter **8**, 4314.

Zhang, X. H., X. Zhang, J. Sun, Z. Zhang, G. Li, H. Fang, X. Xiao, X. Zeng, and J. Hu, 2007, "Detection of novel gaseous states at the highly oriented pyrolytic graphite-water interface," Langmuir **23**, 1778.

Zhang, X. H., X. D. Zhang, S. T. Lou, Z. X. Zhang, J. L. Sun, and J. Hu, 2004, "Degassing and temperature effects on the formation of nanobubbles at the mica/water interface," Langmuir **20**, 3813.

Zhao, B., Y. Song, S. Wang, B. Dai, L. Zhang, Y. Dong, J. Lü, and J. Hu, 2013, "Mechanical mapping of nanobubbles by PeakForce atomic force microscopy," Soft Matter **9**, 8837.